2011

Next generation multi-scale quantum simulations for strongly correlated materials

Shuxiang Yang
Louisiana State University and Agricultural and Mechanical College, yangphysics@gmail.com

NEXT GENERATION MULTI-SCALE QUANTUM SIMULATIONS FOR
STRONGLY CORRELATED MATERIALS

A Dissertation

Submitted to the Graduate Faculty of the
Louisiana State University and
Agricultural and Mechanical College
in partial fulfillment of the
requirements for the degree of
Doctor of Philosophy

in

The Department of Physics and Astronomy

by
Shuxiang Yang
B.S., Zhejiang University, 2004
M.S., Zhejiang University, 2006
M.S., University of Cincinnati, 2008
December 2011

Acknowledgements

Tables of Contents

Abstract

This thesis represents our effort to develop the next generation multi-scale quantum simulation methods suitable for strongly-correlated materials, where complicated phase-diagrams prevail, suggesting complicated underlying physics.

We first give a detailed description of the parquet formalism. With its help, different approximate methods can be unified and a hierarchy of approximate methods with different accuracies and computational complexity can thus be designed.

Next, we present a numerical solution of the parquet approximation. Results on the Hubbard model are compared to those obtained from Determinant Quantum Monte Carlo (DQMC), FLuctuation EXchange (FLEX), and self-consistent second-order approximation methods. The comparison shows a satisfactory agreement with DQMC and a significant improvement over the FLEX or the self-consistent second-order approximation.

The parquet formalism can also be used to analyze the superconducting mechanism of the high-temperature superconductors. The dynamical cluster approximation (DCA) method is used to understand the proximity of the superconducting dome to the quantum critical point in the 2-D Hubbard model. At optimal doping, where V_d is revealed to be featureless, we find a power-law behavior of $\chi_{0d}(\omega = 0)$, replacing the BCS logarithm behavior, and strongly enhanced T_c.

After that we propose another multi-scale approach by combining the DCA and the recently introduced dual-fermion formalism. Within this approach, short and long length scale physics is addressed by the DCA cluster calculation, while intermediate length scale physics is addressed diagrammatically using dual fermions. The bare and dressed dual fermionic Green functions scale as $\mathcal{O}(1/L_c)$, so perturbation theory on the dual lattice converges very quickly.

Lastly, we study the responses to dynamical modulation of the optical lattice potential by analyzing properties of the repulsive fermionic Hubbard model in an optical lattice. We provide numerical evidence showing the modulations by on-site local interaction cannot be ignored, and instead can even strongly contribute to the dynamical behaviors of the system in highly-doped cases.

Chapter 1

Introduction

The discovery of high-temperature superconductors in the 1980s ignited an intense interest and study of strongly correlated fermion systems. The high transition temperature, higher than the boiling point of liquid nitrogen, has already resulted in vast application in industry. However, a room-temperature superconductors could potentially have a much greater impact on industry, and even in our everyday life. To realize that dream, one might need to understand the underlying superconducting mechanism. On the other hand, the expected high-T_c is far above the theoretical upper limit set by the BCS theory, and thus demands a totally different theoretical explanation.

A generic feature in these systems is that the potential energy due to the Coulomb interaction between electrons is comparable to or larger than the kinetic energy due to the movement of the electrons. This is different from the situation in the simple metal or semi-conductor, where interaction energy is much smaller than the kinetic energy and thus conventional perturbation theory works remarkably well. No small parameters exist, making the problem non-perturbative in nature, so the conventional perturbative approaches fail. Numerically, this problem is exemplified, as an example, by the minus-sign problem in quantum Monte Carlo (QMC) simulations, which makes the simulation exponentially hard with increasing system size. The complicated phase diagrams associated with these strongly correlated materials suggest physics with different length scales are competing with each other, rendering a multi-scale two-particle approach essential to analyzing these systems.

To make the discussion more concrete and analysis more practical, we need to start from some model Hamiltonians. For the cuprates, as the representative example of the strongly correlated fermion systems, the Hubbard model is believed to be able to capture its essential low energy physics. Though as simple as the single-band 2-D Hubbard model, no analytical solution exists, and all the conventional perturbation approaches fail. We thus have to turn to the numerical methods.

There are different numerical methods in our disposal for the 2-D Hubbard model. The two most powerful are exact diagonalization and quantum Monte Carlo (QMC). For the former, the computational complexity increases exponentially with the system size, making the calculation restricted to around 20 sites, which is far from enough to extract

the correct thermodynamical limit information. As for QMC, the difficulty is exemplified as the minus sign problem [1], which in the effect makes the simulation of large systems exponentially difficult as well.

People have been trying very hard to seek a possible solution for the minus sign problem for years, but all in vain. And recently, it is proved to be non-deterministic polynomial (NP) hard [1]. In spite of this, new approaches are proposed from time to time trying to solve this problem. An example is the recently introduced bosonization approach. Though it looks like a very clever idea, we prove in our comment [2] [2] that it is equivalent to the conventional BSS algorithm and has the same minus-sign problem.

It may be impossible to solve this problem. Nevertheless, making it less severe is possible. And many people have been working in this direction and great advances are thus achieved. One example is the dynamical mean field theory (DFMT). As a quantum analogy of the conventional Weiss mean field theory, DMFT maps a lattice system into a single-site system embedded into a self-determined dynamical mean field. The spacial fluctuation for the irreducible quantities is frozen while the most important quantum fluctuation is preserved.

The Dynamical Cluster Approach (DCA) is a natural generalization of the DMFA. And the short-ranged spacial correlation is incorporated, and thus DCA can provide a better description of the real system.

The DCA is essentially a two-scale method: short and long. To incorporate the correlation in the intermediate length scale, we thus propose the multi-scale approach: the multi-scale many-body approach and the dual fermion dynamical approach. They mainly differ in the different problem solvers used to take into account the intermediate length-scale physics. For the former, the parquet approach is used, and for the latter, the dual fermion approach is used.

1.1 Structure and Scope

As manifested in the title, this thesis is mainly intended for developing new multi-scale numerical methods for strongly correlated materials. The thesis is structured as follows:

The parquet formalism, which is a combination of both single-particle formalism and two-particle formalism, is described in detail in Chapter 2. Within the parquet formalism, different approximate methods can be unified and a hierarchy of approximate methods are thus formed.

Next, in Chapter 3, we apply the parquet approximation, which is the first two-particle level approximate method, on the 2-D Hubbard model on a half-filled 4×4 cluster. Results are compared to those obtained from Determinant Quantum Monte Carlo (DQMC), FLuctuation EXchange (FLEX), and self-consistent second-order approximation methods. This comparison shows a satisfactory agreement with DQMC

---

[1]See Appendix B.1 for more details
[2]See Appendix B.2 for more details

and a significant improvement over the FLEX or the self-consistent second-order approximation.

In Chapter 4, the dynamical cluster approximation (DCA) method is used to understand the proximity of the superconducting dome to the quantum critical point in the 2-D Hubbard model. In a BCS formalism, T_c may be enhanced through an increase in the d-wave pairing interaction (V_d) or the bare pairing susceptibility (χ_{0d}). At optimal doping, where V_d is revealed to be featureless, we find a power-law behavior of $\chi_{0d}(\omega = 0)$, replacing the BCS log, and strongly enhanced T_c. Experiments are suggested in the end to verify these predictions.

In Chapter 5, another multi-scale approach for strongly correlated systems is proposed by combining the DCA and the recently introduced dual-fermion formalism. This approach employs an exact mapping from a real lattice to a DCA cluster of linear size L_c embedded in a dual fermion lattice. Short-length-scale physics is addressed by the DCA cluster calculation, while longer-length-scale physics is addressed diagrammatically using dual fermions. The bare and dressed dual fermionic Green functions scale as $\mathcal{O}(1/L_c)$, so perturbation theory on the dual lattice converges very quickly. E.g., the dual Fermion self-energy calculated with simple second order perturbation theory is of order $\mathcal{O}(1/L_c^3)$, with third order and three body corrections down by an additional factor of $\mathcal{O}(1/L_c)$.

Chapter 6 is devoted to the study of responses to dynamical modulation of the optical lattice potential by studying properties of the repulsive fermionic Hubbard model in an optical lattice. With the help of quantum Monte Carlo simulations and Maximum Entropy Method as well as Hubbard-I approximation, the numerical evidence shows that the modulations by on-site local interaction cannot be ignored, and can even strongly contribute to the dynamical behaviors of the system in highly-doped cases. The filling of the system plays a very important role to the responses and it also determines the non-equilibrium dynamics of the system under perturbation.

In Chapter 7, a general discussion of future development and application concludes the main body of this thesis.

In the appendix, a variety of subjects about the technical details are presented.

Chapter 2

Parquet Formalism

In this chapter, we will give a detailed description of the parquet formalism, which is a combination of both single-particle formalism and two-particle formalism. Within the parquet formalism, different approximate methods can be unified and a hierarchy of approximate methods can thus been formed.

2.1 Single-Particle Formalism

2.1.1 Single-Particle Green Function and Self-Energy

The single-particle Green function (in the following we will call it Green function) can be defined as

$$
\begin{aligned}
G(\mathbf{r}, \tau) &\equiv \ - < T_\tau c_r(\tau) c_0^\dagger(0) > && (2.1) \\
&\equiv \ -\theta(\tau) < c_r(\tau) c_0^\dagger(0) > +\theta(-\tau) < c_0^\dagger(0) c_r(\tau) > && (2.2)
\end{aligned}
$$

where $\theta(\tau)$ is the step function, and we are using the Heisenberg representation

$$
\hat{O}(\tau) \equiv e^{\tau H} \hat{O} e^{-\tau H} \tag{2.3}
$$

and

$$
< ... >= \frac{Tr\left(e^{-\beta H}...\right)}{Tr\left(e^{-\beta H}\right)} \tag{2.4}
$$

The Green function can be interpreted as the phase a particle accumulates when it moves through the spatial-time space. It is periodic in real space for the usual lattice model and anti-periodic in the imaginary time space, thus can be transformed into the momentum-frequency space:

$$
G(\mathbf{k}, i\omega_n) = \frac{1}{N\beta} \sum_i \int_0^\beta d\tau \, e^{i\omega_n \tau - i\mathbf{k}\mathbf{r}_i} G(r, \tau) \tag{2.5}
$$

The inverse Fourier transform is

$$G(r, \tau) = \sum_{k,n} e^{-i\omega_n \tau + i\mathbf{k}\mathbf{r}_i} G(\mathbf{k}, i\omega_n) \tag{2.6}$$

The Green function $G(r, \tau)$ is long-ranged and is reducible in the sense that the contributing Feynman diagrams can be separated into two pieces by cutting one internal fermion line. Careful analysis of the all contributing Feynman diagrams shows there is some self-similarity in them, and the Green function can be decomposed into a more irreducible and short-ranged quantity named as the self-energy. They are related by the Dyson equation as

$$G(\mathbf{k}, i\omega_n) = G_0(\mathbf{k}, i\omega_n) + G_0(\mathbf{k}, i\omega_n)\Sigma(\mathbf{k}, i\omega_n)G(\mathbf{k}, i\omega_n) \tag{2.7}$$

where $G_0(\mathbf{k}, i\omega_n)$ is the Green function for systems without interaction, and is thus called bare Green function, and $\Sigma(\mathbf{k}, i\omega_n)$ is the self-energy . There is an obvious benefit by making approximation on the self-energy level instead of the Green function. Even if we approximate the self-energy by a small number of Feynman diagrams, we would end up with summing an infinite number of diagrams by solving the above Dyson equation. The fact that the self-energy is short-ranged renders it possible to calculate using small lattice size.

2.1.2 Self-Consistent Diagrammatic Approximate Method

The diagrammatic approach is a powerful method to analyze quantum systems. The central issue within this kind of calculation is how to sum up as many physically relevant Feynman diagrams as possible. And it turns out the self-consistent diagrammatic method is an efficient way to achieve this purpose.

Before a detailed explanation of the self-consistent approximate method, we start by recalling the conventional perturbation calculation. One can start from the Green function (G-based) and calculate each Taylor expansion term directly. Take the first order contribution as an example. We have the Hartree-Fock term diagrammatically shown in Fig. 2.1.

Obviously, the Green function based perturbation calculation is inefficient, and we can improve it by doing the perturbation calculation on the irreducible quantity, namely the self-energy. We calculate the Hartree-Fock contribution to the self-energy, instead of the Green function, and then we calculate the Green function using the Dyson's equation. In this way, we end up with summing an infinite number of diagrams constructed from the Hartree-Fock contribution (see (b) in Fig. 2.1).

We can do an even better job by doing this self-consistently. The algorithm is shown in Fig. 2.2. We need to use the dressed Green function to calculate the self-energy, and after we calculate the Green function from Dyson equation, we need to calculate the self-energy again using the updated Green function, and iterate it until some criterion

a),

b),

c),

1st iter

2nd iter
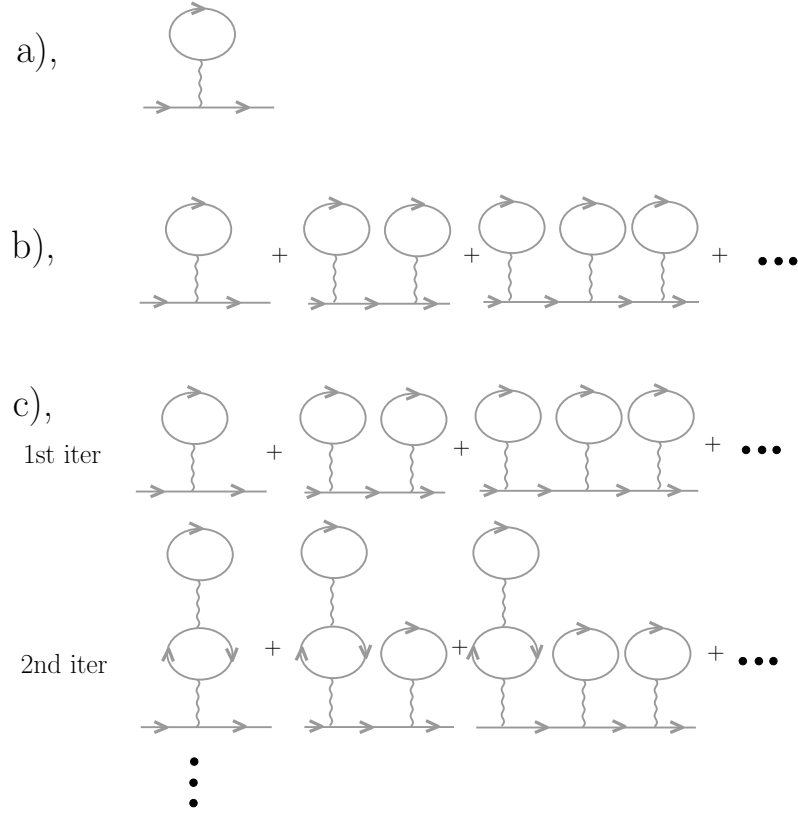
Figure 2.1: Feynman diagrams generated from the conventional G-based HF perturbation (a), conventional Σ-based HF perturbation and the self-consistent HF calculation. Note that the Σ-based HF perturbation incorporates infinite number of diagrams and shows the advantage of making approximation on the irreducible quantity. And self-consistent calculation can include many more diagrams by simply doing the calculation iteratively and enjoys the best efficiency of generating many Feynman diagrams.
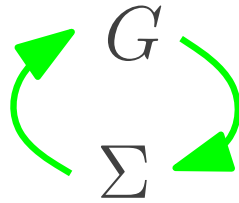
Figure 2.2: Algorithm for the self-consistent HF approximation.

of self-consistency is satisfied. In this way, many more diagrams can be included (see (c) in Fig. 2.1).

2.2 Two-Particle Formalism

2.2.1 Two-Particle Quantities

While single-particle quantities only give an averaged effect from other particles on one specific particle in a motion, two-particle quantities can provide more detailed information about how two particles interact with each other.

Two-Particle Green Function The two-particle Green function for the p-h channel is defined as:

$$\chi^{ph}(\tau_1, \tau_2; \tau_3, \tau_4) \equiv < T_\tau c(\tau_1) c^\dagger(\tau_2) c(\tau_4) c^\dagger(\tau_3) > - < T_\tau c(\tau_1) c^\dagger(\tau_2) > < T_\tau c(\tau_4) c^\dagger(\tau_3) > \tag{2.8}$$

and for p-p channel

$$\chi^{pp}(\tau_1, \tau_2; \tau_3, \tau_4) \equiv < T_\tau c(\tau_1) c(\tau_2) c^\dagger(\tau_4) c^\dagger(\tau_3) > \tag{2.9}$$

in which other degrees of freedom can be added accordingly as the imaginary time index. Its Fourier transform:

$$\chi(i\nu_m)_{i\omega_n, i\omega_{n'}} = \int_0^\beta e^{(i\omega_n + i\nu_m)\tau_1} d\tau_1 \int_0^\beta e^{-i\omega_n \tau_2} d\tau_2 \int_0^\beta e^{-(i\omega_{n'} + i\nu_m)\tau_3} d\tau_3 \chi(\tau_1, \tau_2; \tau_3, 0) \tag{2.10}$$

which is of the dimensionality:

$$\chi(i\nu_m)_{i\omega_n, i\omega_{n'}} \sim \frac{1}{E^3} \tag{2.11}$$

Vertex Function Similar to the self-energy in the single-particle formalism, we have vertex functions. For example, the reducible two-particle vertex $F_h^{ph}(12; 34)$ describes the amplitude of a particle-hole pair scattered from its initial state $|3, 4\rangle$ into the final state $|1, 2\rangle$. Here, $i = 1, 2, 3, 4$ represents a set of indices which combine the momentum $\mathbf{k}_i$, the Matsubara frequency $i\omega_{n_i}$ and, if needed, the spin σ_i and band index m_i.

In general, depending on how particles or holes are involved in the scattering processes, one can define three different two-particle scattering channels. These are the particle-hole (p-h) horizontal channel, the p-h vertical channel and the particle-particle (p-p) channel. For the Hubbard model, the spin degree of freedom further divides the particle-particle channel into triplet and singlet channels while the particle-hole is divided into density and magnetic channels.

One can further discriminate the vertices according to their topology. Starting from the reducible vertex F introduced above, we may define the irreducible vertex Γ corresponding to the subclass of diagrams in F that can not be separated into two parts by cutting two horizontal Green's function lines. Similarly, the fully irreducible vertex Λ corresponds to the subclass of diagrams in Γ that cannot be split into two parts by

7
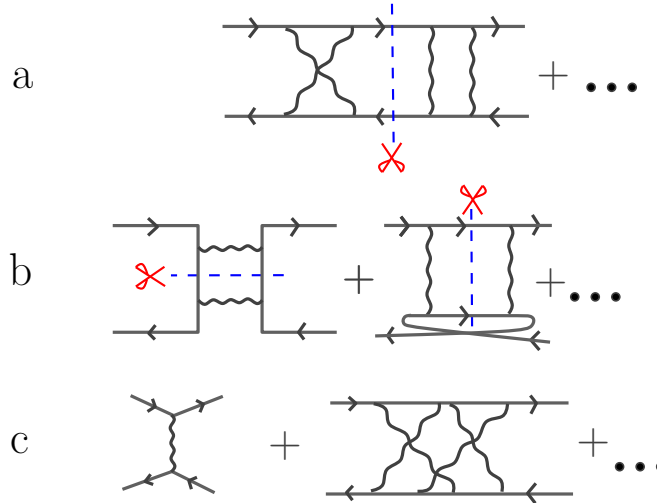
Figure 2.3: Different classes of diagrams; the solid line represents the single-particle Green's function and the wavy line represents the Coulomb interaction: here we use the p-h horizontal channel for illustration. (a) Reducible diagrams: can be separated into two parts by cutting two horizontal Green's function lines. (b) Irreducible diagrams: can only be separated into two parts by cutting two Green's function lines in the other two channels. (c) Fully irreducible diagrams : cannot be split in two parts by breaking two Green's function lines in any channel.

cutting two Green's function lines in any channel. An illustration of these different types of vertices is provided in Fig. 2.3.

The Pauli exclusion principle produces the so-called crossing symmetries which in turn yield relationships between these vertices in the different channels. This enables us to reduce the independent channels defined for the theory to the particle-particle and the particle-hole horizontal channels.

2.2.2 Equations

Schwinger-Dyson Equation The parquet formalism assumes the complete knowledge of the fully irreducible vertices and provides a set of equations which are self-consistent at both the single- and two-particle levels. The connection between the single- and two-particle quantities is through the Schwinger-Dyson equation which connects the reducible vertex F to the self-energy Σ and serves as a bridge between single-particle quantities and two-particle quantities.. It is an exact equation derived from the equation

of motion and has the following form:

$$\Sigma(P) = -\frac{UT^2}{4N} \sum_{P',Q} \{G(P')G(P'+Q)G(P-Q)(F_d(Q)_{P-Q,P'} - F_m(Q)_{P-Q,P'})$$
$$+G(-P')G(P'+Q)G(-P+Q)(F_s(Q)_{P-Q,P'} + F_t(Q)_{P-Q,P'})\}$$

$$(2.12)$$

where the indices P, P' and Q combine momentum $\mathbf{k}$ and Matsubara frequency $i\omega_n$, i.e. $P = (\mathbf{k}, i\omega_n)$.

Bethe-Salpeter Equations Similar to Dyson equation in the single-particle formalism, we have two-particle Dyson equation which relates the two-particle Green function with the vertex functions. For p-p channel, we have

$$\chi^p(Q)_{P,P'} = \beta * G(-P)G(P+Q)\delta_{P,P'}$$
$$- G(P+Q)G(-P)F^p(Q)_{P,P'}G(P'+Q)G(-P') \qquad (2.13)$$

and

$$\chi^p(Q)_{P,P'} = \beta * G(-P)G(P+Q)\delta_{P,P'}$$
$$- \frac{1}{\beta}\sum_{P''}\chi^p(Q)_{P,P''}\Gamma^p(Q)_{P'',P}G(P'+Q)G(-P') \qquad (2.14)$$

As for the p-h channel, we have

$$\chi^{ph}_{d/m}(Q)_{P,P'} = -\beta * G(P)G(P+Q)\delta_{P,P'}$$
$$- G(P+Q)G(P)F_{d/m}(Q)_{P,P'}G(P'+Q)G(P') \qquad (2.15)$$

9

$$\chi^p_{d/m}(Q)_{P,P'} = -\beta * G(P)G(P+Q)\delta_{P,P'}$$

$$-\frac{1}{\beta}\sum_{P''} G(P+Q)G(P)\Gamma^p_{d/m}(Q)_{P,P''}\chi^{ph}(Q)_{P'',P'} \qquad (2.16)$$

For more details about the definitions of these quantities and how to measure them during the QMC simulation, please see the Appendix C.

The reducible and the irreducible vertices in a given channel are related by another form of Bethe-Salpeter equation. It has the following form:

$$F_r(Q)_{P,P'} = \Gamma_r(Q)_{P,P'} + \Phi_r(Q)_{P,P'} \qquad (2.17)$$
$$F_{r'}(Q)_{P,P'} = \Gamma_{r'}(Q)_{P,P'} + \Psi_{r'}(Q)_{P,P'} \qquad (2.18)$$

where $r = d$ or m for the density and magnetic channels respectively and $r' = s$ or t for the singlet and triplet channels, and we are using the vertex ladders which are defined as:

$$\Phi_r(Q)_{P,P'} \equiv \sum_{P''} F_r(Q)_{P,P''}\chi^{ph}_0(Q)_{P''}\Gamma_r(Q)_{P'',P'} \qquad (2.19)$$

$$\Psi_{r'}(Q)_{P,P'} \equiv \sum_{P''} F_{r'}(Q)_{P,P''}\chi^{pp}_0(Q)_{P''}\Gamma_{r'}(Q)_{P'',P'} \qquad (2.20)$$

χ_0 is the direct product of two single-particle Green's functions and is defined according to the particle-particle or the particle-hole channel as

$$\chi^{ph}_0(Q)_P = G(P+Q)G(P) \qquad (2.21)$$

$$\chi^{pp}_0(Q)_P = -\frac{1}{2}G(P+Q)G(-P) \qquad (2.22)$$

Note that in the above, the prefactor $\frac{1}{2}$ is introduced to avoid the double-counting in the p-p channel. This equation shows how a reducible vertex is reducible in its own scattering channel.

Parquet Equation In a similar manner, the irreducible vertex and the fully irreducible vertex are related by the parquet equation. This set of equations expresses the fact that the irreducible vertex in a given channel is still reducible in the other two channels. The parquet equation has the following form in the different channels:

10
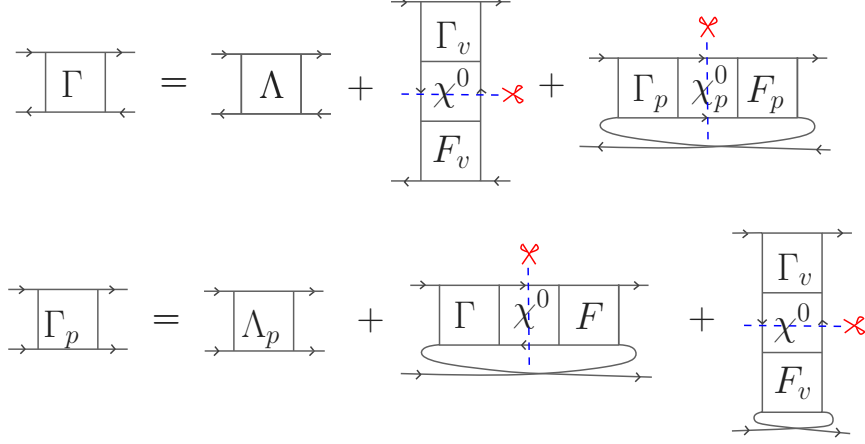
Figure 2.4: Feynman diagram representation of the parquet equation for both p-h and p-p channel. The irreducible vertex Γ is still decomposable in the other channels. Note that the spin indices are ignored for simplicity.

$$\Gamma_d(Q)_{PP'} = \Lambda_d(Q)_{PP'} - \frac{1}{2}\Phi_d(P'-P)_{P,P+Q} - \frac{3}{2}\Phi_m(P'-P)_{P,P+Q} \quad (2.23)$$
$$+ \frac{1}{2}\Psi_s(P+P'+Q)_{-P-Q,-P} + \frac{3}{2}\Psi_t(P+P'+Q)_{-P-Q,-P}$$

$$\Gamma_m(Q)_{PP'} = \Lambda_m(Q)_{PP'} - \frac{1}{2}\Phi_d(P'-P)_{P,P+Q} + \frac{1}{2}\Phi_m(P'-P)_{P,P+Q} \quad (2.24)$$
$$- \frac{1}{2}\Psi_s(P+P'+Q)_{-P-Q,-P} + \frac{1}{2}\Psi_t(P+P'+Q)_{-P-Q,-P}$$

$$\Gamma_s(Q)_{PP'} = \Lambda_s(Q)_{PP'} + \frac{1}{2}\Phi_d(P'-P)_{-P',P+Q} - \frac{3}{2}\Phi_m(P'-P)_{-P',P+Q} \quad (2.25)$$
$$+ \frac{1}{2}\Phi_d(P+P'+Q)_{-P',-P} - \frac{3}{2}\Phi_m(P+P'+Q)_{-P',-P}$$

$$\Gamma_t(Q)_{PP'} = \Lambda_t(Q)_{PP'} + \frac{1}{2}\Phi_d(P'-P)_{-P',P+Q} + \frac{1}{2}\Phi_m(P'-P)_{-P',P+Q} \quad (2.26)$$
$$- \frac{1}{2}\Phi_d(P+P'+Q)_{-P',-P} - \frac{1}{2}\Phi_m(P+P'+Q)_{-P',-P}$$

2.3   Hierarchy of Different Approximate Methods

As summarized in Fig. 2.5, the parquet formalism is a combination of single-particle formalism and two-particle formalism. It provides a self-contained description of a quantum system up to the two-particle quantity level. Based on the parquet formalism, one

can design approximate methods at different levels, forming a hierarchy of approximate methods.
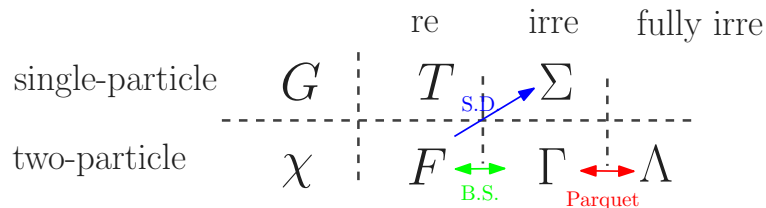
Figure 2.5: Parquet formalism.

2.3.1 Self-Consistent Hartree-Fock Approximation

At the highest level, we might make the approximation on the two-particle Green function (analogous to the conventional G-based Hartree-Fock (HF) perturbation) such that four-point correlation function can be expressed as a product of two two-point correlation functions

$$\langle n_{i\sigma} n_{j\sigma'} \rangle = \langle n_{i\sigma} \rangle \langle n_{j\sigma'} \rangle \tag{2.27}$$

It is equivalent to ignoring the contribution from the vertex functions. So we have

$$F = 0 \tag{2.28}$$

From the Schwinger-Dyson equation, we then end up with including only the HF diagram in the calculation of the self-energy (See (a) in Fig. 2.6).
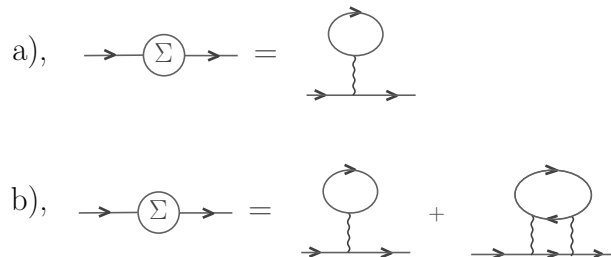
Figure 2.6: Contributions to the self-energy for the HF (a) and SOPT (b) methods.

For this HF method, the lowest-order correction comes from the second-order diagram, and thus is of order of $\mathcal{O}(U^2)$.

2.3.2 Self-Consistent Second-Order Perturbation Theory

As the next level of approximation, we approximate the full vertex F by the bare interaction

12

$$F = v \tag{2.29}$$

Putting this result into the Schwinger-Dyson equation, we then need to sum up first-order and second-order diagrams in the calculation of self-energy (See (b) in Fig. 2.6), which is exactly the Self-consistent Second-Order Perturbation Theory (SOPT). For this method, the lowest-order correction is of order of $\mathcal{O}(U^3)$.

2.3.3   Random-Phase Approximation, T-Matrix Approximation and Fluctuation Exchange Approximation

By approximating the irreducible vertex, instead of the full vertex, we can sum more diagrams, such as the ring-type (See (a) in Fig. 2.7) and the ladder-type (See (b) and (c) in Fig. 2.7). For the former, it is referred to as the random phase approximation (RPA), while the latter is referred to as the T-matrix approximation (TMA). And if we sum up both types of diagrams, then we will end up with the so-called fluctuation exchange approximation (FLEX). As compared to RPA or TMA, FLEX has the advantage of considering fluctuations from different channels equally. For both RPA and TMA, the lowest-order correction is of order of $\mathcal{O}(U^3)$, the same as SOPT, while it is of order of $\mathcal{O}(U^4)$ for FLEX since it includes all the contributions up to the third order in U.
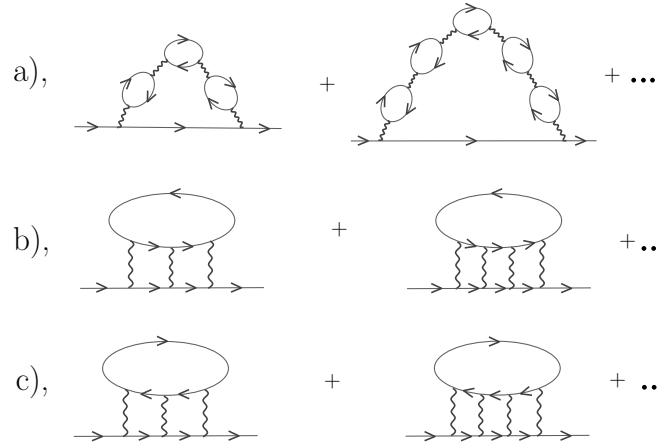
Figure 2.7: Contributions to the self-energy for the RPA (a), TMA (b or c) and FLEX (a, b and c) methods.

Random-Phase Approximation (RPA)   The irreducible vertex in the longitudinal charge channel is approximated by the bare Coulomb interaction. And then the Bethe-Salpeter equation is used to sum over all the ring-type diagrams.

T-Matrix Approximation (TMA) Similar to RPA, the irreducible vertex in the transverse p-h channel or p-p channel, instead of longitudinal p-h channel, is approximated by the bare Coulomb interaction. And then the Bethe-Salpeter equation is used to sum all the ladder-type (instead of ring-type in RPA) diagrams.

Fluctuation Exchange Approximation (FLEX) A combination of RPA and T-matrix approximation, such that the fluctuations in different channels are treated equally.

2.3.4   Parquet Approximation (PA)

To include even more diagrams in our calculation, we need to make the approximation on the irreducible vertex level

$$\Lambda = v \tag{2.30}$$

and then end up with the parquet approximation (PA). Within this approach, more diagrams, like the ring+ladder-type and the simply-crossed diagrams, are included (see Fig. 2.8). As compared to FLEX, PA preserves the crossing-symmetries, which are consequences of the Pauli exclusive principle, and the lowest-order correction is of order of $\mathcal{O}(U^5)$.
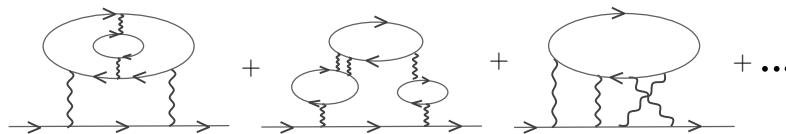
Figure 2.8: More diagrams are included in the PA calculation.

Although many more complicated diagrams are included in the PA approach, we are still missing diagrams as shown in Fig. 2.9. To account for them, we can use the quantum Monte Carlo method to sum up different diagrams and go to the next level of approximate method, so-called Multi-Scale Many-Body approach (MSMB).
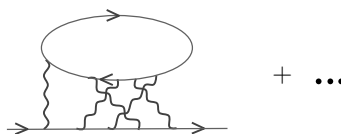
Figure 2.9: Diagrams which are missing in the PA calculation.

2.3.5   Multi-Scale Many-Body Approach

Within this approach, physics at the short length scales is treated explicitly with QMC method, physics at the intermediate length scales treated diagrammatically using fully
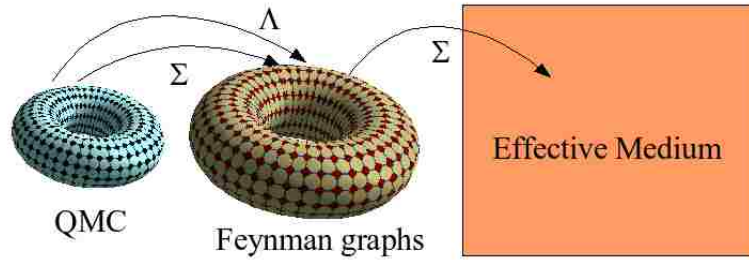
Figure 2.10: Schematic representation of MSMB approach.
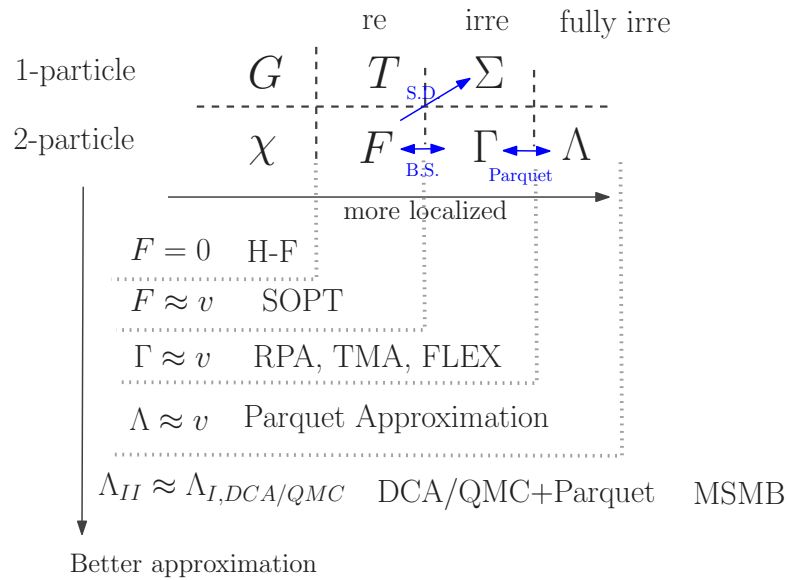
Figure 2.11: From the parquet formalism, one can design a hierarchy of approximate methods with different accuracies and different complexity.

irreducible vertices obtained from QMC, and physics at the long length scales treated at the mean field level.

Chapter 3

Parquet Approximation

In the previous chapter, we unified different approximate methods within the parquet formalism, forming a hierarchy of methods with different precisions and computational complexity. Among them, as the first full two-particle level method, the parquet approximation has been out of our reach due to the massive computational requirement since the introduction of parquet formalism. And only recently can we for the first time carry out parquet calculations.

In this chapter, we will show how the parquet approximation is implemented, what the computational challenges are, and how we solve them. With the almost perfectly parallel parquet code, we apply it on the 2-D Hubbard model on a half-filled 4×4 cluster. Results are compared to those obtained from Determinant Quantum Monte Carlo (DQMC), FLuctuation EXchange (FLEX), and self-consistent second-order approximation methods. This comparison shows a satisfactory agreement with DQMC and a significant improvement over the FLEX or the self-consistent second-order approximation.

During this project, I worked out the whole parquet formalism, designed the parquet approximation algorithm, and implemented the serial version of the parquet code. To make the code more stable, I went to University of Goettingen to work with Thomas Pruschke, and finally we designed the damping scheme for our code, making the code a practical tool for the strongly correlated electron systems. And I wrote a Matlab version of the code, which is very helpful for the analysis the stability behavior of the parquet approximation and turns out to be an ideal platform to try new techniques on the parquet calculation efficiently. To make it parallel using MPI, I proposed the three-step procedure to implement the vertex rotation, which is the communication bottle-neck of the whole calculation. And then I worked with our collaborators to implement the MPI version of parquet code. Later we added the OpenMP directives to increase the parallel efficiency. This code is available in the public domain [1], and has seen several hundred accesses up to now.

This work has been published in Phys. Rev. E, 80, 046706, (2009). The following sections in this chapter are from that paper.

---

[1]http://www.phys.lsu.edu/~syang/parquet/index.html

3.1   Introduction

Over the past 50 years, many different techniques have been devised and employed to study strongly correlated electron systems. Unfortunately, advantages of the successful attempts were usually outweighed by their limitations. Recently, because of the progress in computer technology, complex diagramatic approaches have received increased attention. Although Baym and Kadanoff's Φ derivability [3, 4] does not guarantee the physical validity of a theory, their framework enables the generation of conserving approximations which are guaranteed to satisfy a variety of Ward identities. For these reasons, the FLuctuation EXchange (FLEX) approximation [5, 6] has been intensively studied over the years. Its major disadvantage, however, is that it represents a conserving approximation at the single-particle level only. Thus, the physical validity of the approximation appears to be questionable as the vertices are either overestimated or underestimated and the Pauli exclusion principle is not respected properly [7]. In contrast, the parquet formalism [8] introduced by de Dominicis et al. in 1964 is a conserving approximation which is self-consistent also at the two-particle level and one may hope that it resolves at least some of the limitations FLEX has. Unfortunately, it has an extremely complicated structure and was, apart from applications to the Anderson impurity model and the 1-D Hubbard model with small system size [9, 10], hitherto also computationally out of reach. To circumvent this limitation, Bickers et al. introduced the so-called pseudo-parquet approximation [5] which attempts to improve on the FLEX without introducing the complexity of the full Parquet equations. But this approach fails to properly address the full frequency and momentum dependence of the scattering processes. Only very recently, due to the great advance of parallel computing and the tremendous increase in computer memory, has it become possible to fully solve this approximation for the first time.

The chapter is organised as follows. In section 3.2, we discuss the algorithm and the numerical difficulties that arise. In section 3.3, we present first results obtained from the parquet approximation (PA) for the 2-dimensional Hubbard model and their comparison to other conserving approximation methods such as FLEX and self-consistent second-order approximation (SC2nd). As a benchmark, we compare these results against the Determinant Quantum Monte Carlo (DQMC) which provides a numerically exact result.

3.2   Algorithm and Computational Challenge

The set of equations dicussed above are solved self-consistently as illustrated in the self-consistency loop in Fig. 3.1. One starts with a guess of the single-particle Green's function or self-energy. This can, for example, be taken from the second-order approximation. The reducible and the irreducible vertices are also initialized with the bare interaction. The self-consistency loop can then be described as follows:
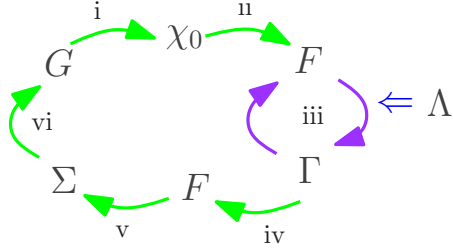
Figure 3.1: (color online) Schematic illustration for the different steps in solving the parquet approximation equations self-consistently.

(i) first we calculte the bare susceptibility χ_0 which is given by the product of two Green's functions

(ii) next this bare susceptibility is used to calculate F through the Bethe-Salpeter equation

(iii) we then proceed with updating the irreducible vertices Γ by solving the parquet equation.
This step requires the input of the fully irreducible vertex Λ. In the context of the parquet approximation which we study here it is taken to be the bare interaction. It however can also be extracted from some more sophisticated methods.

(iv) it is followed by a calculation of the new F through the Bethe-Salpeter equation

(v) this value of F is then used to update the self-energy through the Schwinger-Dyson equation

(vi) the Dyson's equation is solved for the Green's function G.

This loop is repeated until convergence of the self-energy Σ is achieved within a reasonable criterion.

Unfortunately, this loop becomes unstable when the strength of the Coulomb interaction is increased or the temperature is lowered. As we believe that this instability is purely numerical in origin and related to the iterative nature of the algorithm, we have to extend the above scheme to account for this problem. For example, one possibility is to start with an overestimated self-energy and to damp it along with the irreducible vertex between two iterations according to:

$$\Sigma = \alpha_1 \Sigma_{new} + (1 - \alpha_1)\Sigma_{old} \tag{3.1}$$

$$\Gamma = \alpha_2 \Gamma_{new} + (1 - \alpha_2)\Gamma_{old} \tag{3.2}$$

where α_1 and α_2 are some damping parameters.

Another possibility is to rewrite the coupled Bethe-Salpeter and parquet equations in the form $f(\mathbf{x}) = 0$ and apply a variant of a Newton's root searching method. Then

18

we can take advantage of the existing linear solvers such as BiCGS [11], GMRES [12] or the Broyden algorithm [13].

One major advantage that the parquet formalism has over Exact Diagonalization (ED) or Quantum Monte Carlo (QMC) is that it scales algebraically with the volume of the system in space-time for any choice of parameters including those that lead to a sign problem in QMC. The most time-consuming part of the formalism is the solution of the Bethe-Salpeter and the parquet equations, where the computational time scales as $O(n_t^4)$ where $n_t = n_c \times n_f$, n_c being the number of sites on the cluster and n_f the number of Matsubara frequencies. Although the scaling is better than that of ED or QMC when the sign problem is severe, one can see that the complexity quickly grows beyond the capacity of usual desktop computers with incrasing system size, and large-scale supercomputer systems have to be employed.

Our parallel scheme and our data distribution are based on the realization that the Bethe Salpeter equation is the most time-consuming part of our calculation. One can easily see that it decouples nicely with respect to the bosonic momentum-frequency index Q. This enables us to distribute the vertices across processors with respect to this third index and to solve the Bethe-Salpeter equation with a local matrix inversion. However, this storage scheme puts a limit on the size of the problem that we can address. For a node with 2 GBytes of memory, the maximum value of n_t that we can use if our variables are complex double precision is about 2500.

Unlike the Bethe-Salpeter equation, one can readily observe that the parquet equation does not decouple in terms of the third index. Solving this equation requires a rearrangement of the matrix elements across processors and this is the communication bottleneck in the algorithm. The rearrangement is necessary to obtain the form of the vertex ladder Φ or Ψ that is required in the parquet equation. For instance, in the d channel, we need $\Phi\left(P - P'\right)_{P,P+Q}$. This form of the vertex ladder is obtained by employing the three-step process described in the following equations:

$$\Phi\left(Q\right)_{P,P'} \implies \Phi\left(Q\right)_{P,P-P'} \tag{3.3}$$

$$\Phi\left(Q\right)_{P,P-P'} \implies \Phi\left(P - P'\right)_{P,Q} \tag{3.4}$$

$$\Phi\left(P - P'\right)_{P,Q} \implies \Phi\left(P - P'\right)_{P,P+Q} \tag{3.5}$$

The first step in this transformation only moves data locally in memory. This does not require much time. The second step is actually just a 2D matrix transpose but with matrix elements spreading on many nodes. This is where communication across nodes is required. It is achieved by using the standard Message Passing Interface (MPI) collective directives[2]. The final step is also local and can equally be done very fast.
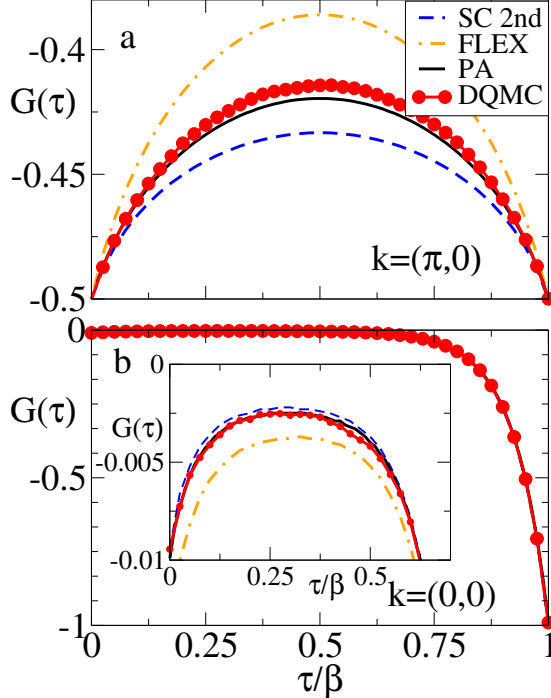
Figure 3.2: (color online) Single-particle Green function $G(\tau)$ for two different momenta a), $\mathbf{k} = (\pi, 0)$, b), $\mathbf{k} = (0,0)$, extracted the three diagrammatic approaches and the DQMC. For this temperature ($T = 0.3t$), the PA result (solid line) looks very close to the DQMC one (symbol solid line) as compared to SC second-order (dashed line) or FLEX (dash-dotted line). In the insert of b) is an enlarged view of the figure.

3.3 Results

In the following section, we will show the PA results for a 4×4 Hubbard cluster at half-filling. The calculations are done for $U = 2t$ and different temperatures. The calculations are performed for a finite number of Matsubara frequencies[3]. However, for the observables we calculated, such as the local moment and magnetic susceptibility in Fig. 3.3 and Fig. 3.4, we performed an extrapolation to an infinite number of frequencies so that the cutoff error in frequency is minimized. To see how good PA works for the lattice model, we use the DQMC result as the benchmark. In the DQMC calculation, $\Delta\tau = 1/12$ is used and the combined statistical and systematic errors are smaller than the symbols used. To further compare PA to other approximations, FLEX and self-consistent second-order results are also included.

---

[2]For a detailed description of MPI, we refer to: http://www.mcs.anl.gov/research/projects/mpi/

[3]We use the periodic boundary condtions in the frequency space for the ease of implementation. And we have checked that different boundary conditions converge to the same result as n_f increases.

3.3.1   Single-Particle Green Function $G(\tau)$

First, one can get a rough idea of how PA improves the accuracy of physical observables by comparing the single-particle Green's function from different levels of approximation. Shown in Fig. 3.2 are $G_{\mathbf{k}}(\tau)$ with $\mathbf{k} = (\pi, 0)$ and $\mathbf{k} = (0, 0)$ calculated from the self-consistent second-order approximation, FLEX, PA and DQMC. The parquet result is significantly closer to the DQMC result than the second-order approximation and FLEX results as can readily seen from the figure. This confirms the intuition that one would get better results if the approximation is made on the vertex which is most irreducible.

3.3.2   Unscreened Local Moment
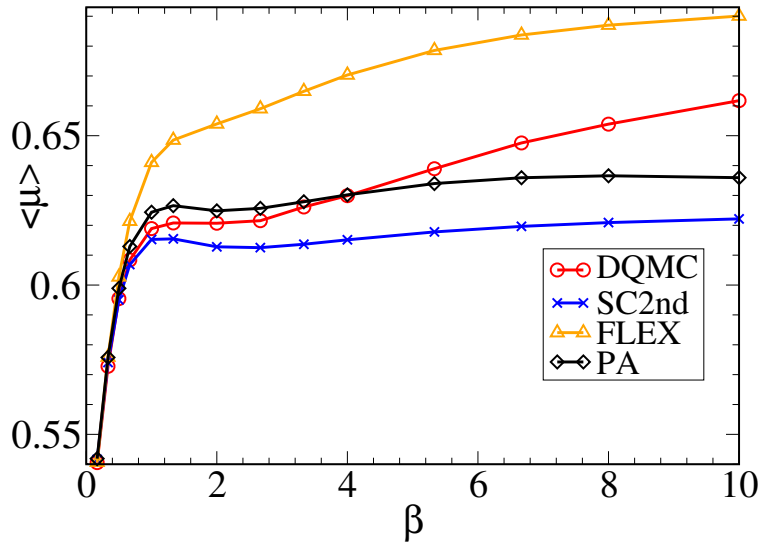
Figure 3.3: (color online) The inverse temperature dependence of local moment. Among the three diagrammatic approaches, the PA result comes closest to the DQMC one.

Next we present results for the local magnetic moment defined as

$$
\begin{aligned}
\langle \mu \rangle &\equiv \langle (n_\uparrow - n_\downarrow)^2 \rangle && (3.6) \\
&= \langle n \rangle - 2 \langle n_\uparrow n_\downarrow \rangle && (3.7)
\end{aligned}
$$

where $\hat{n}_\sigma$ denotes the number operator for electrons of spin σ. In the context of a conserving approximation, it can be re-expressed in terms of the self-energy and the single-particle Green's function as

$$
\langle \mu \rangle = \langle n \rangle - \frac{2T}{U} Tr(\Sigma G) \tag{3.8}
$$

where the trace sums over both the momentum and the frequency degrees of freedom.

The results are shown in Fig. 3.3. Among the three diagrammatic approaches, the PA result comes closest to the DQMC one. If we look more carefully at the DQMC curve, we can find the existence of two humps. The hump at $T_1 \simeq U/2$, which is well reproduced by the PA, designates the energy scale for the charge fluctuation, and is directly related to the suppression of charge double occupancy. The other hump beginning at $T_2 \ll t$ is related to the virtual exchange interaction, J, between nearby spins. It is believed to be related to the synergism between the development of the long-range antiferromagnetic correlation and enhancement of the local moment. As a result, a pseudogap is opened which increases the entropy of the system [14, 15]. The magnitude of T_2 can be estimated by noticing $J = 4t^2/U$ for the strong coupling limit and $t \exp(-2\pi t/U)$ in the weak coupling limit [14, 16]. Therefore it basically interpolates between these two limits for that $U = 2t$ is in the intermediate coupling regime. This hump is not well captured by PA. The increasing importance of envelop-shape diagram contribution [5, 7] not included in PA is responsible for this deviation in the low temperature region.

3.3.3 Uniform Susceptibility
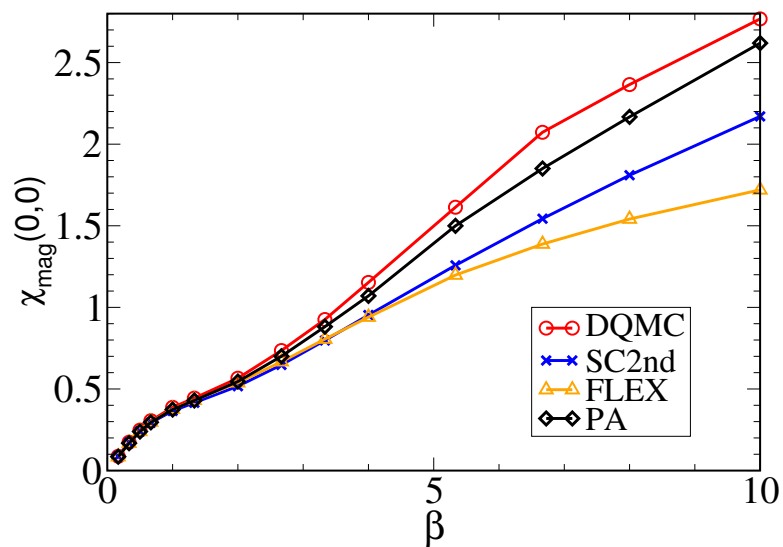
Figure 3.4: (color online) Uniform susceptibility calculated for different methods as a function of inverse temperature. While at the high temperature region, all the diagrammatic method results come close to the DQMC result, the PA shows its advantage clearly in the low temperature region.

Finally, we look at the uniform magnetic susceptibility which is defined as

$$\chi_{mag}(0,0) = \int_0^\beta d\tau \left\langle \hat{T}_\tau S_z(\tau) S_z(0) \right\rangle \tag{3.9}$$

$$= \frac{1}{T} \left\langle S_z^2 \right\rangle \tag{3.10}$$

with magnetic moment defined as

$$\hat{S}_z\left(\tau\right) \;\; = \;\; \frac{1}{N}\sum_r \left(n_{r,\uparrow}\left(\tau\right) - n_{r,\downarrow}\left(\tau\right)\right) \tag{3.11}$$

The χ_{mag} from different approaches are presented in Fig. 3.4. The uniform magnetic susceptibility calculated from DQMC follows a nearly linear dependence on β. This mimics closely the Curie-Weiss law of weakly interacting moments and implies that the dominant effect in the system is the short range magnetic fluctuation. This is consistent with the β dependence of the local moment presented in Fig. 3.3. As the temperature still dominates over the spin energy scale of the system, it suppresses the long range fluctuation.

From this figure, the improvement of PA over the other two approximations is also easy to see. Similar to the local moment, the difference between results from PA and DQMC at the low temperature region can be explained by the omission of envelop-shape diagrams in PA.

3.4 Summary and Outlook

We have presented the parquet formalism, PA method and in particular the implementation we use to solve large-sized problem. The preliminary application of PA on the 4×4 Hubbard cluster shows that it can yield better results than the self-consistent second-order or FLEX calculations. This is the first step in our work, next we are going to use the parquet formalism in the so-called Multi-Scale Many-Body (MSMB) approach [17]. Within MSMB, correlations at different length scales are treated with different methods. The short length scales are treated explicitly with QMC methods, intermediate length scales treated diagrammatically using fully irreducible vertices obtained from QMC and long length scales treated at the mean field level. Note that in this approach the fully irreducible vertex is approximated by a QMC calculation on a small cluster, while in PA it is approximated by the bare interaction. Therefor this approach should provide superior results to the PA. Another advantage is that it can also avoid the exponential increase of the computational cost as the system size increases, and thus can take full advantage of the most up-to-date computer resources available. We will combine it with the Local Density Approximation (LDA) to gain some predictive power from the first principle electronic structure calculation.

Chapter 4

Proximity of Superconducting Dome to the QCP

The parquet formalism can also used to analyze the underlying mechanism of second-order phase transition. Especially, we are most interested in the superconducting mechanism of the high-temperature superconductors. In the chapter, we use the dynamical cluster approximation (DCA) method to understand the proximity of the superconducting dome to the quantum critical point in the 2-D Hubbard model. In a BCS formalism, T_c may be enhanced through an increase in the d-wave pairing interaction (V_d) or the bare pairing susceptibility (χ_{0d}). At optimal doping, where V_d is revealed to be featureless, we find a power-law behavior of $\chi_{0d}(\omega = 0)$, replacing the BCS log, and strongly enhanced T_c. And we suggest experiments in the end to verify these predictions.

In this project, I carried out the DCA calculation, determined the phase digram by extracting the simulated data, and implemented the analysis code to do the vertex decomposition using the parquet formalism. And I also worked with other collaborators to analyze the bare d-wave susceptibility.

This work has been published in Phys. Rev. Lett. 106, 047004 (2011). The following sections in this chapter are from that paper.

Reprinted by permission of "Phys. Rev. Lett.".

4.1 Introduction

The unusually high superconducting transition temperature of the cuprates remains an unsolved puzzle, despite more than two decades of intense theoretical and experimental research. Central to the efforts to unravel this mystery is the idea that the high critical temperature is due to the presence of a quantum critical point (QCP) which is hidden under the superconducting dome [18, 19]. Numerical calculations in the Hubbard model, which is accepted as the de-facto model for the cuprates, strongly support the case of a finite-doping QCP separating the low-doping region, found to be a non-Fermi liquid (NFL), from a higher doping Fermi-liquid (FL) region [20, 21]. Calculations also

show that in the vicinity of the QCP, and for a wide range of temperatures, the doping and temperature dependence of the single-particle properties, such as the quasi-particle weight [20], as well as thermodynamic properties such as the chemical potential and the entropy, are consistent with marginal Fermi liquid (MFL) behavior [22]. This QCP emerges by tuning the temperature of a second-order critical point of charge separation transitions to zero and is therefore intimately connected to $q = 0$ charge fluctuations [23]. Finally, the critical doping seems to be in close proximity to the optimal doping for superconductivity as found both in the context of the Hubbard [23] and the t-J model [24]. Even though this proximity may serve as an indication that the QCP enhances pairing, the detailed mechanism is largely unknown.

In this project, we attempt to differentiate between two incompatible scenarios for the role of the QCP in superconductivity. The *first* scenario is the quantum critical BCS (QCBCS) formalism introduced by She and Zaanen (She-Zaanen) [25]. According to this, the presence of the QCP results in replacing the logarithmic divergence of the BCS pairing bubble by an algebraic divergence. This leads to a stronger pairing instability and higher critical temperature compared to the BCS for the same pairing interactions. The *second* scenario suggests that remnant fluctuations around the QCP mediate the pairing interaction [26, 27]. In this case the strength of the pairing interaction would be strongly enhanced in the vicinity of the QCP, leading to the superconducting instability. Here, we find that near the QCP, the pairing interaction depends monotonically on the doping, but the bare pairing susceptibility acquires an algebraic dependence on the temperature, consistent with the first scenario.

4.2   Formalism

In a conventional BCS superconductor, the superconducting transition temperature, T_c, is determined by the condition $V\chi_0'(\omega = 0) = 1$, where χ_0' is the real part of the $q = 0$ bare pairing susceptibility, and V is the strength of the pairing interaction. The transition is driven by the divergence of $\chi_0'(\omega = 0)$ which may be related to the imaginary part of the susceptibility via $\chi_0'(\omega = 0) = \frac{1}{\pi} \int d\omega \chi_0''(\omega)/\omega$. And $\chi_0''(\omega)$ itself can be related to the spectral function, $A_{\boldsymbol{k}}(\omega)$, through

$$\chi_0''(x) = \frac{\pi}{N} \sum_{\zeta, \boldsymbol{k}} \int d\omega A_{\boldsymbol{k}}(\omega) A_{\boldsymbol{k}}(\zeta x - \omega) \left(f(\omega - \zeta x) - f(\omega) \right) \qquad (4.1)$$

where the summation of $\zeta \in \{-1, +1\}$ is used to anti-symmetrize $\chi_0''(\omega)$. In a FL, $\chi_0''(\omega) \propto N(\omega/2) \tanh(\omega/4T)$, and $\chi_0'(T) \propto N(0) \ln(\omega_D/T)$ with $N(0)$ the single-particle density of states at the Fermi surface and ω_D the phonon Debye cutoff frequency. This yields the well known BCS equation $T_c = \omega_D \exp\left(-1/(N(0)V)\right)$. In the QCBCS formulation, the BCS equation is $V\chi'(\omega = 0) = 1$, where χ' is fully dressed by both the self energy and vertices associated with the interaction responsible for the QCP, but not by the pairing interaction V. In the Hubbard model the Coulomb interaction is responsible for both the QCP and the pairing, so this deconstruction is not possible. Thus, we will

use the more common BCS T_c condition to analyze our results with $V\chi'_0(\omega = 0) = 1$ where χ'_0 is dressed by the self energy but without vertex corrections. Since the QCP is associated with MFL behavior, we do not expect the bare bubble to display a FL logarithm divergence. Here, we explore the possibility that $\chi'_0(\omega = 0) \sim 1/T^\alpha$.

The two-dimensional Hubbard model is expressed as:

$$H = H_k + H_p = \sum_{\boldsymbol{k}\sigma} \epsilon^0_{\boldsymbol{k}} c^\dagger_{\boldsymbol{k}\sigma} c_{\boldsymbol{k}\sigma} + U \sum_i n_{i\uparrow} n_{i\downarrow}, \qquad (4.2)$$

where $c^\dagger_{\boldsymbol{k}\sigma}(c_{\boldsymbol{k}\sigma})$ is the creation (annihilation) operator for electrons of wavevector $\boldsymbol{k}$ and spin σ, $n_{i\sigma} = c^\dagger_{i\sigma} c_{i\sigma}$ is the number operator, $\epsilon^0_{\boldsymbol{k}} = -2t\left(\cos(k_x) + \cos(k_y)\right)$ with t being the hopping amplitude between nearest-neighbor sites, and U is the on-site Coulomb repulsion.

We employ the dynamical cluster approximation (DCA) [28, 29] to study this model with a Quantum Monte Carlo (QMC) algorithm as the cluster solver. The DCA is a cluster mean-field theory which maps the original lattice onto a periodic cluster of size $N_c = L_c^2$ embedded in a self-consistent host. Spatial correlations up to a range L_c are treated explicitly, while those at longer length scales are described at the mean-field level. However the correlations in time, essential for quantum criticality, are treated explicitly for all cluster sizes. To solve the cluster problem we use the Hirsch-Fye QMC method [30, 31] and employ the maximum entropy method [32] to calculate the real-frequency spectra.

We evaluate the results starting from the Bethe-Salpeter equation in the pairing channel:

$$\chi(Q)_{P,P'} = \chi_0(Q)_P \delta_{P,P'} + \sum_{P''} \chi(Q)_{P,P''} \Gamma(Q)_{P'',P'} \chi_0(Q)_{P'} \qquad (4.3)$$

where χ is the dynamical susceptibility, $\chi_0(Q)_P [= -G(P+Q)G(-P)]$ is the bare susceptibility, which is constructed from G, the dressed one-particle Green's function, Γ is the vertex function, and indices $P^{[\dots]}$ and external index Q denote both momentum and frequency. The instability of the Bethe-Salpeter equation is detected by solving the eigenvalue equation $\Gamma\chi_0\phi = \lambda\phi$ [33] for fixed Q. By decreasing the temperature, the leading λ increases to one at a temperature T_c where the system undergoes a phase transition. To identify which part, χ_0 or Γ, dominates at the phase transition, we project them onto the d-wave pairing channel (which was found to be dominant [21, 34]). For χ_0, we apply the d-wave projection as $\chi_{0d}(\omega) = \sum_k \chi_0(\omega, q = 0)_k g_d(k)^2 / \sum_k g_d(k)^2$, where $g_d(k) = (\cos(k_x) - \cos(k_y))$ is the d-wave form factor. As for the pairing strength, we employ the projection as $V_d = \sum_{k,k'} g_d(k)\Gamma_{k,k'} g_d(k') / \sum_k g_d(k)^2$, using Γ at the lowest Mastsubara frequency [35].

To further explore the different contributions to the pairing vertex, we employ the formally exact parquet equations to decompose it into different components [35, 36]. Namely, the fully irreducible vertex Λ, the charge (S=0) particle-hole contribution, Φ_c, and the spin (S=1) particle-hole contribution, Φ_s, through: $\Gamma = \Lambda + \Phi_c + \Phi_s$. Similar
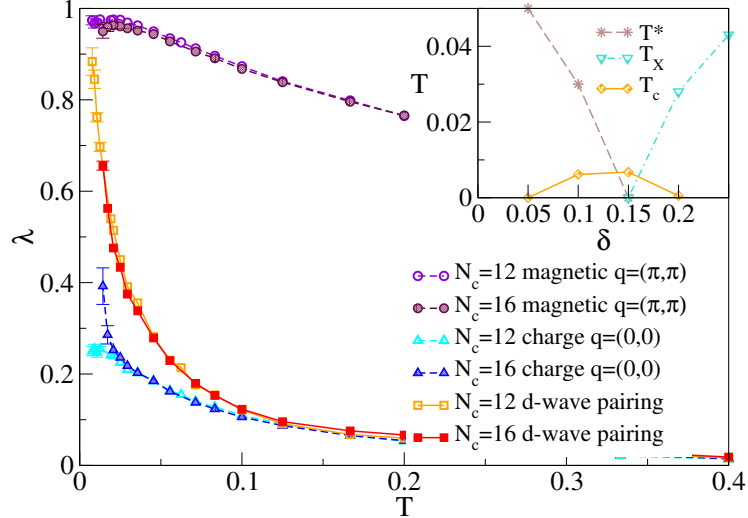
Figure 4.1: (Color online) Plots of leading eigenvalues for different channels at the critical doping for $N_c = 12$ and $N_c = 16$ site clusters. The inset shows the phase diagram with superconducting dome, pseudogap T^* and FL T_X temperatures from Ref. [20]

to the previous expression, one can write $V_d = V_d^\Lambda + V_d^c + V_d^m$, where each term is the d-wave component of the corresponding term. Using this scheme, we will be able to identify which component contributes the most to the d-wave pairing interaction.

4.3   Results

We use the BCS-like approximation, discussed above, to study the proximity of the superconducting dome to the QCP. We take $U = 6t$ ($4t = 1$) on 12 and 16 site clusters large enough to see strong evidence for a QCP near doping $\delta \approx 0.15$ [20, 22, 23]. We explore the physics down to $T \approx 0.11J$ on the 16 site cluster and $T \approx 0.07J$ on the 12-site cluster, where $J \approx 0.11$ [20] is the antiferromagnetic exchange energy. The fermion sign problem prevents access to lower T.

Fig. 4.1 displays the eigenvalues of different channels (pair, charge, magnetic) at the QC filling. The results for the two cluster sizes are nearly identical, and the pairing channel eigenvalue approaches one at low T, indicating a superconducting d-wave transition at roughly $T_c = 0.007$. However, in contrast to what was found previously [35], the $q = 0$ charge eigenvalue is also strongly enhanced, particularly for the larger $N_c = 16$ cluster, as it is expected from a QCP emerging as the terminus of a line of second-order critical points of charge separation transitions [23]. The inset shows the phase diagram, including the superconducting dome and the pseudogap T^* and FL T_X temperatures.

In Fig. 4.2, we show the strength of the d-wave pairing vertex V_d versus doping for a range of temperatures. Consistent with previous studies [37], we find that V_d falls monotonically with increasing doping. At the critical doping, $\delta_c = 0.15$, V_d shows no
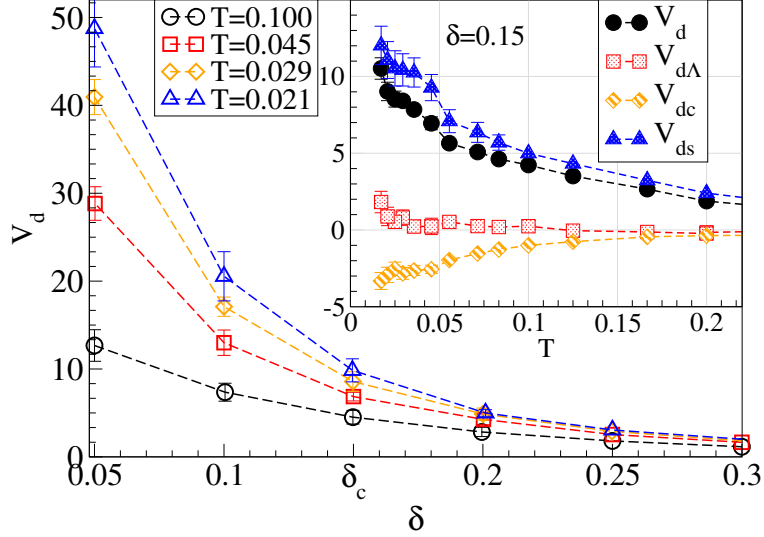
Figure 4.2: (Color online) Plots of V_d, the strength of the d-wave pairing interaction for various temperatures with $U = 1.5$ ($4t = 1$) and $N_c = 16$. V_d decreases monotonically with doping, and shows no feature at the critical doping. In the inset are plots of the contributions to V_d from the charge V_d^c and spin V_d^s cross channels and from the fully irreducible vertex V_d^Λ versus T at the critical doping. As the temperature is lowered, $T \ll J \approx 0.11$, the contribution to the pairing interaction from the spin channel is clearly dominant.

feature, invalidating the second scenario described above. The different components of V_d at the critical doping versus temperature are shown in the inset of Fig. 4.2. As the QCP is approached, the pairing originates predominantly from the spin channel. This is similar to the result of Ref. [35] where the pairing interaction was studied away from quantum criticality.

In contrast, the bare d-wave pairing susceptibility χ_{0d} exhibits significantly different features near and away from the QCP. As shown in Fig. 4.3, in the underdoped region (typically $\delta = 0.05$), the bare d-wave pairing susceptibility $\chi'_{0d}(\omega = 0)$ saturates at low temperatures. However, at the critical doping, it diverges quickly with decreasing temperature, roughly following the power-law behavior $1/\sqrt{T}$, while in the overdoped or FL region it displays a log divergence.

To better understand the temperature-dependence of $\chi'_{0d}(\omega = 0)$ at the QC doping, we looked into $T^{1.5}\chi''_{0d}(\omega)/\omega$ and plotted it versus ω/T in Fig. 4.4. When scaled this way, the curves from different temperatures fall on each other such that $T^{1.5}\chi''_{0d}(\omega)/\omega = H(\omega/T) \approx (\omega/T)^{-1.5}$ for $\omega/T \gtrsim 9 \approx 4t/J$. For $0 < \omega/T < 4t/J$, the curves deviate from the scaling function $H(x)$ and show nearly BCS behavior, with $\chi''_{0d}(\omega)/\omega|_{\omega=0}$ which is weakly sublinear in $1/T$ as shown in the inset. The curves away from the critical doping (not displayed) do not show such a collapse. In the underdoped region ($\delta = 0.05$) at low frequencies, $\chi''_{0d}(\omega)/\omega$ goes to zero with decreasing temperature (inset). In the FL region ($\delta = 0.25$) $\chi''_{0d}(\omega)/\omega$ develops a narrow peak at low ω of width $\omega \approx T_X$ and height
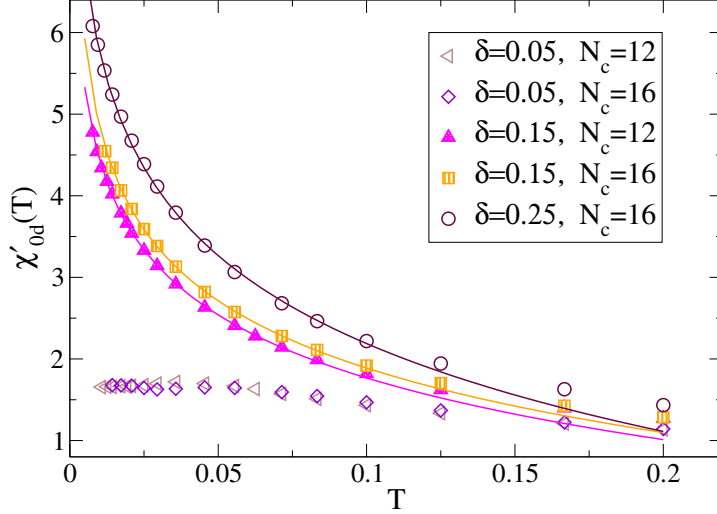
Figure 4.3: (Color online) Plots of $\chi'_{0d}(\omega = 0)$, the real part of the bare d-wave pairing susceptibility, at zero frequency vs. temperature at three characteristic dopings. The solid lines are fits to $\chi'_{0d}(\omega = 0) = B/\sqrt{T} + A\ln(\omega_c/T)$ for $T < J$. In the underdoped case ($\delta = 0.05$), $\chi'_{0d}(\omega = 0)$ does not grow with decreasing temperature. At the critical doping ($\delta = \delta_c = 0.15$), $\chi'_{0d}(\omega = 0)$ shows power-law behavior with $B = 0.04$ for the 12 site, and $B = 0.09$ for the 16-site clusters (in both $A = 1.04$ and $\omega_c = 0.5$). In the overdoped region ($\delta = 0.25$), a log divergence is found, with $B = 0$ obtained from the fit.

$\propto 1/T$ as shown in the inset.

4.4   Discussion

$\chi''_{0d}(\omega)/\omega$ reveals details about how the instability takes place. The overlapping curves found at the QC filling contribute a term $T^{-1.5}H(\omega/T)$ to $\chi''_{0d}(w)/w$ or $\chi'_{0d}(T) \propto 1/\sqrt{T}$ as found in Fig. 4.3. There is also a component which does not scale, especially at low frequencies. In fact, $\chi''_{0d}(\omega)/\omega$ at zero frequency increases more slowly than $1/T$ as expected for a FL. From this sublinear character, we infer that the contribution of the non-scaling part of $\chi''_{0d}(\omega)/\omega$ to the divergence of $\chi'_{0d}(T)$ is weaker than BCS and may cause us to overestimate A and underestimate B in the fits performed at the critical doping in Fig. 4.3. In addition, if $H(0)$ is finite, it would contribute a term to $\chi'_{0d}(T)$ that increases like $1/T^{1.5}$, so $H(0) = 0$. From Eq. 4.1 we see that the contribution to $\chi''_{0d}(\omega)/\omega$ at small ω comes only from states near the Fermi surface. $H(0) = 0$ would indicate that the enhanced pairing associated with $\chi'_{0d}(T) \propto 1/\sqrt{T}$ is due to higher energy states. The vanishing of $\chi''_{0d}(\omega)/\omega$ in the pseudogap region ($\delta = 0.05$) for small frequency when $T \to 0$ indicates that around the Fermi surface, the dressed particles do not respond to a pair field. Or, perhaps more correctly, none are available for pairing due to the pseudogap depletion of electron states around the Fermi surface. Thus, even the strong
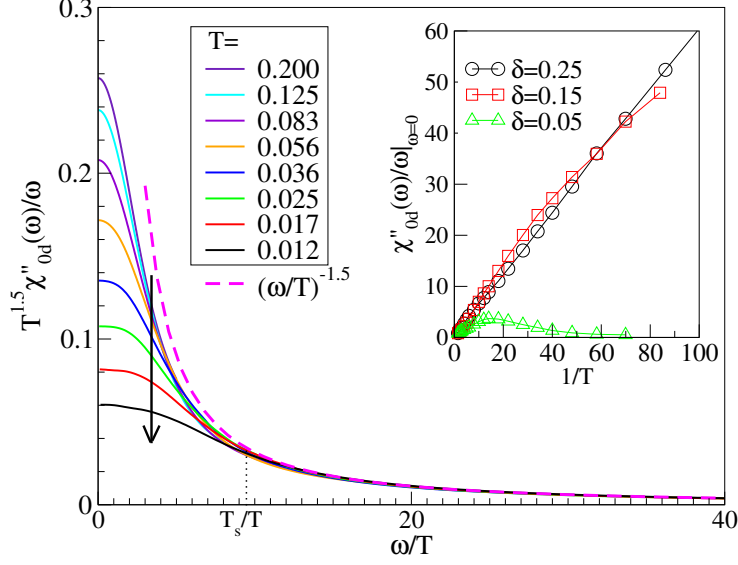
Figure 4.4: (Color online) Plots of $T^{1.5}\chi''_{0d}(\omega)/\omega$ versus ω/T at the QC doping ($\delta = 0.15$) for $N_c = 16$. The arrow denotes the direction of decreasing temperature. The curves coincide for $\omega/T > 9 \approx (4t/J)$ defining a scaling function $H(\omega/T)$, corresponding to a contribution to $\chi'_{0d}(T) = \frac{1}{\pi}\int d\omega \chi''_{0d}(w)/w \propto 1/\sqrt{T}$ as found in Fig. 4.3. For $\omega/T > 9 \approx (4t/J)$, $H(\omega/T) \approx (\omega/T)^{-1.5}$ (dashed line). On the x-axis, we add the label $T_s/T \approx (4t/J)$, where T_s represents the energy scale where curves start deviating from H. The inset shows the unscaled zero-frequency result $\chi''_{0d}(\omega)/\omega|_{\omega=0}$ plotted versus inverse temperature.

d-wave interaction, seen in Fig. 4.2, is unable to drive the system into a superconducting phase. In the overdoped region, $\chi''_{0d}(\omega)/\omega$ displays conventional FL behavior for $T < T_X$, and the vanishing V_d suppresses T_c.

Together, the results for χ_{0d} and V_d shed light on the shape of the superconducting dome in the phase diagram found previously [23]. With increasing doping, the pairing vertex V_d falls monotonically. On the other hand, $\chi'_{0d}(T)$ is strongly suppressed in the low doping or pseudogap region and enhanced at the critical and higher doping. These facts alone could lead to a superconducting dome. Futhermore, the additional algebraic divergence of $\chi'_{0d}(T)$ seen in Fig. 4.3 causes the superconductivity to be enhanced even more strongly near the QCP where one might expect $T_c \propto (V_d B)^2$, with $B = \frac{1}{\pi}\int dx H(x)$, compared to the conventional BCS form in the FL region.

Similar to the scenario for cuprate superconductivity suggested by Castellani *et al.* [26], we find that the superconducting dome is due to charge fluctuations adjacent to the QCP related to charge ordering. However, we differ in that we find the pairing in this region is due to an algebraic temperature dependence of the bare susceptibility χ_{0d} rather than an enhanced d-wave pairing vertex V_d, and that this pairing interaction is dominated by the spin channel.

Our observation in the Hubbard model offers an experimental accessible variant of

She-Zaanen's QCBCS. We use the bare pairing susceptibility χ_0 while She-Zaanen use the full χ, which includes all the effects of quantum criticality but not the correction from the pairing vertex (the pairing glue is added separately). This decomposition is not possible in numerical calculations or experiments since both quantum criticality and pairing originate from the Coulomb interaction. However, the effect of quantum criticality already shows up in the one-particle quantities, and the spectra have different behaviors for the three regions around the superconducting dome. She-Zaanen assume that $\chi''(\omega) \propto 1/\omega^\alpha$ for $T_s < \omega < \omega_c$, where ω_c is an upper cutoff, and that it is irrelevant $(\alpha < 0)$, marginal $(\alpha = 0)$, or relevant $(\alpha > 0)$, respectively in the pseudo gap region, FL region and QCP vincity. We find the same behavior in χ_0 and we have the further observation that near the QCP $T_s \approx (4t/J)T$ and $\alpha = 0.5$.

Experiments combining angle-resolved photo emission (ARPES) and inverse photo emission results, with an energy resolution of roughly J, could be used to construct χ_{0d} and explore power law scaling at the critical doping. Since the energy resolution of ARPES is much better than inverse photo emission, it is also interesting to study $\chi''_{0d}(\omega)/\omega|_{\omega=0}$, which only requires ARPES data, but not inverse photo emission.

4.5 Conclusion

Using the DCA, we investigate the d-wave pairing instability in the two-dimensional Hubbard model near critical doping. We find that the pairing interaction remains dominated by the spin channel and is not enhanced near the critical doping. However, we find a power-law divergence of the bare pairing susceptibility at the critical doping, replacing the conventional BCS logarithmic behavior. We interpret this behavior by studying the dynamic bare pairing susceptibility which has a part that scales like $\chi''_{0d}(\omega)/\omega \sim T^{-1.5}H(\omega/T)$, where $H(\omega/T)$ is a universal function. Apparently, the NFL character of the QCP yields an electronic system that is far more susceptible to d-wave pairing than the FL and pseudogap regions. We also suggest possible experimental approaches to exploit this interesting behavior.

Chapter 5

Dual Fermion Dynamical Cluster Approach

In this chapter, we will propose another multi-scale approach for the strongly correlated systems by combining the DCA and the recently introduced dual-fermion formalism. This approach employs an exact mapping from a real lattice to a DCA cluster of linear size L_c embedded in a dual fermion lattice. Short-length-scale physics is addressed by the DCA cluster calculation, while longer-length-scale physics is addressed diagrammatically using dual fermions. The bare and dressed dual fermionic Green functions scale as $\mathcal{O}(1/L_c)$, so perturbation theory on the dual lattice converges very quickly. E.g., the dual Fermion self-energy calculated with simple second order perturbation theory is of order $\mathcal{O}(1/L_c^3)$, with third order and three body corrections down by an additional factor of $\mathcal{O}(1/L_c)$.

In this project, I worked out the formalism with other collaborators. And I implemented the serial and MPI versions of dual fermion code, and carried out most of the calculation and analysis.

This work has been published in Phys. Rev. B 84, 155106 (2011). The following sections in this chapter are from that paper.

Reprinted by permission of "Phys. Rev. B".

5.1   Introduction

Dynamical mean-field theory [38, 39, 40] has been remarkably successful at capturing the physics of strongly correlated systems dominated by spatially local correlations. Successes include the description of the Mott transition in the Hubbard model, screening effects in the periodic Anderson model, as well as the description of correlation effects in realistic systems [41, 42, 43].

Since the introduction of the dynamical mean-field approximation (DMFA) there have been a number of attempts to develop formal extensions around the DMFA that incorporate non-local corrections. These include cluster extensions of the DMFA, such as

the dynamical cluster approximation (DCA) [28, 29, 31] or the cellular dynamical mean-field theory (CDMFT) [44], and multi-scale approximations where the DMFA or DCA vertices are used to parametrize two-particle field theories and longer ranged correlations can thus be captured [45, 17, 46]. One of the main limitations of these theories is that they converge slowly with the linear cluster size L_c, especially for the calculation of transition temperatures.

The dual fermion formalism [47, 48, 49] is however, distinctly different from other cluster extensions of the DMFA. In the dual fermion formalism, the lattice action is first mapped onto a dual fermion action where the interaction vertices are the n-body reducible vertices of the cluster. This mapping is exact, so the dual fermion formalism provides a complete and exact formalism for the lattice problem. Thus far, the dual fermion formalism has only been explored using the DMFA or the CDMFT as cluster solvers [50]. However, the CDMFT has the disadvantage in this context that it violates translational invariance, so that the CDMFT vertices are rank-4 tensors in the spatial or momentum indices, which are too large to be stored and manipulated on most computers, especially for large clusters. Thus in this manuscript we propose the dual fermion dynamical cluster approach (DFDCA), within which the long-ranged correlations can be systematically incorporated through the dual fermion lattice calculation. Since the DCA preserves the translational invariance of the lattice system, the DCA two-body vertices are rank-3 tensors which, for modest cluster sizes, will fit in the memory of modern computers. Another difference, which we will discuss in detail, is that the small parameter for the DFDCA is the dual fermion single-particle Green function, which scales as $G_d \sim \mathcal{O}(1/L_c)$ with L_c being the linear cluster size. As a result, perturbation theory on the dual fermion lattice converges very quickly. Simple second order perturbation theory on the dual fermion lattice already yields a dual fermion self-energy of order $\mathcal{O}(1/L_c^3)$ with two-body and three-body corrections down by an additional factor of $\mathcal{O}(1/L_c)$. Higher order approximations are also possible, since, e.g., the three-body vertex corrections to the DFDCA self-energy are small, $\mathcal{O}(1/L_c^4)$. Therefore, the resulting DFDCA formalism converges very quickly with increasing cluster size, with corrections to the self-energy no larger than $\mathcal{O}(1/L_c^4)$.

5.2 Mapping the DCA Formalism to Dual Fermions

We will derive the DFDCA formalism with the example of the Hubbard model. Its Hamiltonian is

$$H = -\sum_{<ij>} t_{ij}(c_{i\sigma}^\dagger c_{j\sigma} + \text{H.c.}) + U\sum_i (n_{i\uparrow} - 1/2)(n_{i\downarrow} - 1/2) \tag{5.1}$$

where t_{ij} is the matrix of hopping integrals, $c_{i\sigma}^{(\dagger)}$ is the annihilation (creation) operator for electrons on lattice site i with spin σ, $n_{i\sigma} = c_{i\sigma}^\dagger c_{i\sigma}$, and U the intra-atomic repulsion.

The DMFA, and its cluster extensions such as the DCA, are based upon the common idea of embedding a cluster in a lattice. We assume that the cluster, of size $N_c = L_c^D$,

dimensionality D, sites labeled by I and wavevectors K, is embedded in a large but finite-sized lattice of size N with sites i and wavevectors k. In the DCA, the reciprocal space of the lattice is divided into N_c cells of identical geometry and linear size Δk. The cell centers are labeled by K, and the points surrounding K within the coarse-graining cell are labeled with $\tilde{k}$. We will also invoke a dual space lattice which is of the same size and geometry as the real lattice.

The action for this model is

$$S[c^*, c] = -\sum_{\omega,k,\sigma} c^*_{\omega,k,\sigma}[(i\omega + \mu)\mathbf{1} - h_k]c_{\omega,k,\sigma} + \sum_i S_{loc}[c^*_i, c_i], \qquad (5.2)$$

where $S_{loc}[c^*_i, c_i]$ is the local part of the action including the Hubbard interaction term, c^*_i and c_i are now Grassmann numbers corresponding to creation and annihilation operators on the lattice, μ the chemical potential, h_k the lattice bare dispersion, and $\omega = (2n+1)\pi T$ the Matsubara frequencies. Decomposing the wavevector according to $k = K + \tilde{k}$, the lattice action becomes

$$S[c^*, c] = \sum_i S_{loc}[c^*_i, c_i] - \sum_{\omega,K,\tilde{k},\sigma} c^*_{\omega,K+\tilde{k},\sigma}[(i\omega + \mu)\mathbf{1} - h_{K+\tilde{k}}]c_{\omega,K+\tilde{k},\sigma}. \qquad (5.3)$$

The goal is to express this action in terms of the DCA cluster problem [1]

$$S_{\text{cluster}}[\bar{c}^*, \bar{c}] = \sum_I S_{loc}[\bar{c}^*_I, \bar{c}_I] - \sum_{\omega,K,\sigma} \bar{c}^*_{\omega,K,\sigma}[(i\omega + \mu)\mathbf{1} - \bar{h}_K - \Delta(K, i\omega)]\bar{c}_{\omega,K,\sigma}, \qquad (5.4)$$

where $\bar{c}^*_I$ and $\bar{c}_I$ are now Grassmann numbers corresponding to creation and annihilation operators on the DCA cluster, and $\Delta(K, i\omega)$ is the cluster hybridization function. To this end, we add and subtract the hybridization function and coarse-grained dispersion, i.e.,

$$\sum_{\omega,K,\tilde{k},\sigma} c^*_{\omega,K+\tilde{k},\sigma}[\bar{h}_K + \Delta(K, i\omega)]c_{\omega,K+\tilde{k},\sigma} = \frac{N}{N_c}\sum_{\omega,K,\sigma} \bar{c}^*_{\omega,K,\sigma}[\bar{h}_K + \Delta(K, i\omega)]\bar{c}_{\omega,K,\sigma}, \qquad (5.5)$$

where the last line follows from the DCA coarse-graining identity

$$\bar{c}^*_{\omega,K,\sigma}\bar{c}_{\omega,K,\sigma} \equiv \frac{N_c}{N}\sum_{\tilde{k}} c^*_{\omega,K+\tilde{k},\sigma}c_{\omega,K+\tilde{k},\sigma} \qquad (5.6)$$

and the coarse-grained dispersion is given by

$$\bar{h}_K = \frac{N_c}{N}\sum_{\tilde{k}} h_{K+\tilde{k}}. \qquad (5.7)$$

---

[1]Note that since the interaction is assumed to be local, it is unaffected by coarse-graining. Non-local interactions however will be coarse-grained.

The DCA coarse-graining identity preserves the Fermionic Lie algebra, despite the fact that it is not a canonical transformation,

$$\left\{ \bar{c}^{\dagger}_{K,\sigma}, \bar{c}_{K',\sigma'} \right\} = \frac{N_c}{N} \sum_{\tilde{k}} \left\{ c^{\dagger}_{K+\tilde{k},\sigma}, c_{K'+\tilde{k},\sigma'} \right\} = \delta_{K\sigma,K'\sigma'}, \tag{5.8}$$

where the last step follows since the coarse graining cells surrounding K and K' have the same geometry and contain the same number of states which, therefore, may be labeled with the same $\tilde{k}$. We then obtain

$$
\begin{aligned}
S[c^*, c] &= \sum_i S_{loc}[c^*_i, c_i] - \sum_{\omega, K, \tilde{k}, \sigma} c^*_{\omega, K+\tilde{k}, \sigma} [(i\omega + \mu)\mathbf{1} - \bar{h}_K - \Delta(K, i\omega)] c_{\omega, K+\tilde{k}, \sigma} \\
&\quad - \sum_{\omega, k, \sigma} c^*_{\omega, k, \sigma} [\Delta(M(k), i\omega) + \bar{h}_{M(k)} - h_k] c_{\omega, k, \sigma}.
\end{aligned}
\tag{5.9}
$$

In the third line of this equation we have introduced the function $M(k)$ which maps the momentum k in the DCA momentum cell to the cluster momentum contained in that cell. Coarse-graining the first and the second terms on the right hand side of the above equation yields the cluster action (5.4). Since the latter is independent of $\tilde{k}$, we may write

$$S[c^*, c] = \sum_{\tilde{k}} S_{\text{cluster}}[\bar{c}^*, \bar{c}] - \sum_{\omega, k, \sigma} c^*_{\omega, k, \sigma} [\Delta(M(k), i\omega) + \bar{h}_{M(k)} - h_k] c_{\omega, k, \sigma}. \tag{5.10}$$

Again, up to this point, we have only re-arranged terms and employed an identity which defines $\bar{c}$. No approximation has been made.

The dual fermions are now introduced by means of the following Gaussian identity

$$\int \exp(-f^*_\alpha a_{\alpha\beta} f_\beta - f^*_\alpha b_{\alpha\beta} c_\beta - c^*_\alpha b_{\alpha\beta} f_\beta) \Pi_\gamma df^*_\gamma df_\gamma = \det(a) \exp[c^*_\alpha (ba^{-1}b)_{\alpha\beta} c_\beta] \tag{5.11}$$

for Grassmann variables in the path integral representation for the partition function

$$\int \exp(-S[c^*, c]) \mathcal{D}[c^*, c]. \tag{5.12}$$

To be specific, we choose the (diagonal) matrices according to

$$
\begin{aligned}
a_{\omega, k, \sigma} &= \bar{g}^{-2}(M(k), i\omega)[\Delta(M(k), i\omega) + \bar{h}_{M(k)} - h_k]^{-1}; \\
b_{\omega, k, \sigma} &= \bar{g}^{-1}(M(k), i\omega).
\end{aligned}
\tag{5.13}
$$

where $\bar{g}$ is the single-particle Green function calculated on the DCA cluster. Applying the above identity to the second term in (5.10) yields

$$\sum_{\omega,k,\sigma} \frac{f^*_{\omega,k,\sigma}\, f_{\omega,k,\sigma}}{\bar{g}^2(M(k),i\omega)[\Delta(M(k),i\omega) + \bar{h}_{M(k)} - h_k]}$$
$$+ \sum_{\omega,k,\sigma}[f^*_{\omega,k,\sigma}\bar{g}^{-1}(M(k),i\omega)c_{\omega,k,\sigma} + H.c.]. \qquad (5.14)$$

The essential observation now is that, since $\bar{g}^{-1}(M(k),i\omega) \equiv \bar{g}^{-1}(K,i\omega)$ is independent of $\tilde{k}$, the second line of (5.14) may be coarse grained using again the DCA coarse-graining identity

$$\overline{f}^*_{\omega,K,\sigma}\overline{c}_{\omega,K,\sigma} \equiv \frac{N_c}{N}\sum_{\tilde{k}} f^*_{\omega,K+\tilde{k},\sigma}c_{\omega,K+\tilde{k},\sigma}. \qquad (5.15)$$

As a consequence the lattice action, Eq. (5.10), can be expressed in the form

$$S[c^*,c;f^*,f] = \sum_{\tilde{k}} S_{\text{restr}}[\overline{c}^*,\overline{c};\overline{f}^*,\overline{f}] + \sum_{\omega,K,\tilde{k},\sigma} \frac{f^*_{\omega,K+\tilde{k},\sigma}\, f_{\omega,K+\tilde{k},\sigma}}{\bar{g}^2(K,i\omega)[\Delta(K,i\omega) + \bar{h}_K - h_k]} \qquad (5.16)$$

where

$$S_{\text{restr}}[\overline{c}^*,\overline{c};\overline{f}^*,\overline{f}] = S_{\text{cluster}}[\overline{c}^*,\overline{c}] + \sum_{\omega,K,\sigma}[\overline{f}^*_{\omega,K,\sigma}\bar{g}^{-1}(K,i\omega)\overline{c}_{\omega,K,\sigma} + h.c.] \qquad (5.17)$$

is the action *restricted* to the cluster.

The transformation to dual fermions is completed by integrating out the fermionic degrees of freedom corresponding to $\overline{c}$ and $\overline{c}^*$. Since S_{restr} is independent of $\tilde{k}$, this can be done individually for each cluster

$$\frac{1}{Z_{\text{cluster}}} \int \exp(-S_{\text{restr}}[\overline{c}^*,\overline{c};\overline{f}^*,\overline{f}])\mathcal{D}[\overline{c}^*,\overline{c}]$$
$$= \exp\left(-\sum_{\omega,K,\sigma} \overline{f}^*_{\omega,K,\sigma}\bar{g}^{-1}(K,i\omega)\overline{f}_{\omega,K,\sigma} - V[\overline{f}^*,\overline{f}]\right). \qquad (5.18)$$

Eq. (5.18) defines the dual potential which can be obtained by expanding both sides and comparing the resulting expressions order by order. It is given by [51]:

$$
\begin{aligned}
V[\overline{f}^*,\overline{f}] &= \frac{1}{4}\sum_{KK'Q}\sum_{\omega\omega'\nu}\sum_{\sigma_1,\sigma_2,\sigma_3,\sigma_4} \gamma_{\sigma_1,\sigma_2,\sigma_3,\sigma_4}(K,K',Q;i\omega,i\omega',i\nu) \\
&\quad \times \overline{f}^*_{\omega+\nu,K+Q,\sigma_1}\overline{f}_{\omega,K,\sigma_2}\overline{f}^*_{\omega',K',\sigma_3}\overline{f}_{\omega'+\nu,K'+Q,\sigma_4} + \dots
\end{aligned} \qquad (5.19)
$$

36

where γ is the full (reducible) vertex of the cluster quantum impurity model, and the higher order contributions involve the n-body (for $n > 2$) reducible vertices as the bare interaction. Integrating out the lattice fermions results in an action which depends only on the dual fermion degrees of freedom given by

$$S_d[f^*, f] = -\sum_{k\omega\sigma} f^*_{\omega k\sigma} G^0_d(k, i\omega)^{-1} f_{\omega k\sigma} + \sum_{\tilde{k}} V[\overline{f}^*, \overline{f}], \tag{5.20}$$

where G^0_d is the bare dual Green function defined by

$$G^0_d(k, i\omega) = -\frac{\overline{g}(K, i\omega)^2}{\overline{g}(K, i\omega) + \left(\Delta(K, i\omega) + \overline{h}_K - h_k\right)^{-1}}. \tag{5.21}$$

This quantity together with the dual potential $V[\overline{f}^*, \overline{f}]$ provides sufficient input for a many-body diagrammatic perturbation calculation on the dual lattice.

Note that besides the DCA coarse-graining process introduced here, the above derivation is a natural generalization of the dual fermion DMFA formulation of Rubtsov *et al.* [47]

5.2.1   Self-consistency Condition

In rewriting the lattice action in terms of the cluster impurity model in the above derivation, the DCA hybridization function has been added and subtracted and hence is an arbitrary quantity. In order to fix this quantity we impose the condition

$$G^0_d(K, i\omega) = \frac{N_c}{N} \sum_{\tilde{k}} G^0_d(K + \tilde{k}, i\omega) \overset{!}{=} 0. \tag{5.22}$$

To appreciate the consequences of this condition, first consider the DCA lattice Green function

$$G^{-1}_{\mathrm{DCA}}(K + \tilde{k}, i\omega) = (i\omega + \mu)\mathbf{1} - h_{K+\tilde{k}} - \Sigma_c(K, i\omega), \tag{5.23}$$

which can be expressed in terms of the cluster Green function

$$\overline{g}^{-1}(K, i\omega) = (i\omega + \mu)\mathbf{1} - \overline{h}_K - \Sigma_c(K, i\omega) - \Delta_c(K, i\omega), \tag{5.24}$$

as

$$G^{-1}_{\mathrm{DCA}}(K + \tilde{k}, i\omega) = \overline{g}^{-1}(K, i\omega) + \Delta_c(K, i\omega) + \overline{h}_K - h_{K+\tilde{k}}. \tag{5.25}$$

Using the last expression, one may straightforwardly derive the following identity relating the DCA lattice Green function to the bare dual Green function

$$G^{d,0}(K + \tilde{k}, i\omega) = G_{\mathrm{DCA}}(K + \tilde{k}, i\omega) - \overline{g}(K, i\omega). \tag{5.26}$$

Hence the above condition (5.22) is equivalent to requiring that the coarse-grained DCA lattice Green function be equal to the Green function of the cluster impurity model. This

is exactly the DCA self-consistency condition. The DCA solution is therefore obtained if no diagrammatic corrections are taken into account and the hybridization is determined such that (5.22) holds. Consequently, we have a perturbation theory around the DCA as the starting point. While the DCA solution only depends on the cluster momentum K, the dependence on $\tilde{k}$ can be introduced by solving the dual problem perturbatively.

5.2.2 Scaling of the Dual Fermion DCA Approach with Cluster Size

The bare dual Green function is given by Eq. (5.21). If we introduce the linear cluster size L_c through $N_c = L_c^D$, one finds that the term $\left(\Delta(K, i\omega) + \overline{h}_K - h_k\right) \sim \mathcal{O}(1/L_c)$. The small nature of this term for large L_c should ensure rapid convergence of the DFDCA. In particular, we then have

$$G_d^0(k, i\omega) = -\overline{g}(K, i\omega)\left(\Delta(K, i\omega) + \overline{h}_K - h_k\right)\overline{g}(K, i\omega) + \mathcal{O}(1/L_c^2), \qquad (5.27)$$

i.e., the bare dual Green function also scales like

$$G_d^0(k, i\omega) \sim \mathcal{O}(1/L_c). \qquad (5.28)$$

However, at points of high symmetry, where $\overline{h}_K - h_k \sim \mathcal{O}(1/L_c^2)$, $G_d^0(k, i\omega)$ will fall more quickly than $\mathcal{O}(1/L_c)$.

To illustrate the typical scaling behavior of the bare dual Green function, we plot in Fig. 5.1, as a function of $1/L_c$, the ratio of $|G_d^0(k, i\omega = i\pi T, L_c)|$ averaged over k to the average $|G_d^0(k, i\omega = i\pi T, L_c = 1)|$. We also plot the average of the ratios. The former initially falls more quickly than $\mathcal{O}(1/L_c)$, while the latter displays a slower initial slope. However, for $L_c \geq 4$ both fall roughly linearly in $1/L_c$. This behavior is found to be independent of temperature (not shown), since it is a purely algebraic effect.

Applying the standard tools to the dual fermion action, one obtains the formal expression

$$G_d(k, i\omega) = G_d^0(k, i\omega) + G_d^0(k, i\omega)T_d(k, i\omega)G_d^0(k, i\omega), \qquad (5.29)$$

for the full dual fermion Green function $G_d(k, i\omega)$, where the reducible self-energy or scattering matrix $T_d(k, i\omega)$ of the dual system is introduced. We will show later, that $T_d(k, i\omega)$ will be at most of order $\mathcal{O}(1/L_c^3)$, and we can infer the scaling

$$G_d(k, i\omega) \sim \mathcal{O}(1/L_c) \qquad (5.30)$$

for the full dual fermion Green function too.

Once the dual fermion Green function is known, one can reconstruct the real lattice Green function as

$$\begin{aligned} G(k, i\omega) &= \overline{g}(K, i\omega)^{-2}\left(\Delta(K, i\omega) + \overline{h}_K - h_k\right)^{-2}G_d(k, i\omega) \\ &+ \left(\Delta(K, i\omega) + \overline{h}_K - h_k\right)^{-1}. \end{aligned} \qquad (5.31)$$
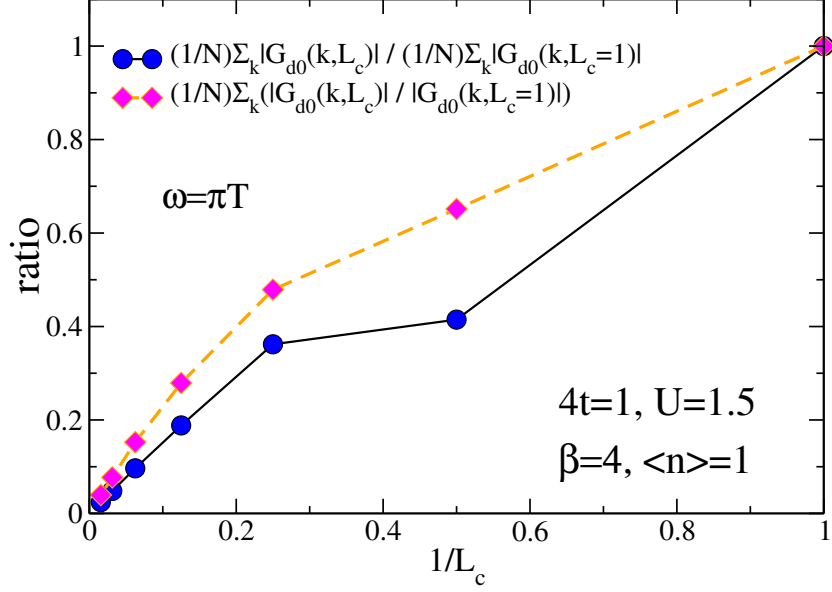
Figure 5.1: Scaling plot for the bare dual Green function. Here we have used the 1-D Hubbard model to analyze its scaling behavior. Except for very small L_c values, the two ratios scale linearly according to Eq. (5.28).

Since $G(k, i\omega)$ is the Green function of the real lattice, it should scale as

$$G(k, i\omega) \sim \mathcal{O}(1) \tag{5.32}$$

with respect to any length scale. On the other hand, for the two terms on the right hand side in (5.31) we find

$$\overline{g}(K, i\omega)^{-2} \left(\Delta(K, i\omega) + \overline{h}_K - h_k \right)^{-2} G_d(k, i\omega) \sim \mathcal{O}(L_c) \tag{5.33}$$

and

$$\left(\Delta(K, i\omega) + \overline{h}_K - h_k \right)^{-1} \sim \mathcal{O}(L_c) . \tag{5.34}$$

Thus, the two $\mathcal{O}(L_c)$ terms must cancel each other. To verify this requirement, we insert the zeroth order contribution of the dual Green function into the original Green function, and after some algebra we indeed obtain

$$G(k, i\omega) \sim \overline{g}(K, i\omega) \sim \mathcal{O}(1), \tag{5.35}$$

with a correction given by

$$\Delta G(k, i\omega) \sim T_d(k, i\omega). \tag{5.36}$$

Therefore, the correction to the real Green function through the dual fermion approach scales the same way as the dual self-energy.

Presently, the dual potential Eq. (5.19) still contains an infinite hierarchy of vertices. The previous discussion now provides a very important insight into the contributions of these vertices to a perturbative expansion: Each n-body diagrammatic insertion will involve a vertex and n Green function lines. In the parameter region away from a critical point the dual potential will be of order $\mathcal{O}(1)$. As noted before, the dual Green function is of order $\mathcal{O}(1/L_c)$, i.e., each dual space diagrammatic insertion is of order $\mathcal{O}(1/L_c^2)$ when it involves the two-body dual space interaction, of order $\mathcal{O}(1/L_c^3)$ for the three-body interaction, and so on. This means that the two-body contribution to V, explicitly shown in Eq. (5.19), will actually dominate and low-order perturbation theory will be sufficient to accurately capture the corrections to the DCA from the dual fermion lattice.

5.2.3 Mapping Back from the Dual Fermion to the Real Lattice

The relation of the real fermion Green function to the dual Green function has been been established in Eq. (5.31). This is an exact relation which follows by taking the functional derivative of two equivalent partition functions. They are linked through the same Gaussian identity that has been used to introduce the dual fermions (Eq. (5.11)). Higher order derivatives then allow us to derive relations between higher order cumulants. From this recipe, we find the following relation between the two-particle reducible vertex functions

$$
\begin{aligned}
F_{k,k',q;i\omega,i\omega',i\nu} &= T(k+q, i\omega + i\nu)T(k, i\omega)\, F^d_{k,k',q;i\omega,i\omega',i\nu} \\
&\times\ T(k', i\omega')T(k'+q, i\omega' + i\nu)
\end{aligned}
\tag{5.37}
$$

in real and dual space, where

$$
\begin{aligned}
T(k, i\omega) &= \frac{G_d(k, i\omega)}{G(k, i\omega)(\Delta(K, i\omega) + \bar{h}_K - h_k)\bar{g}(K, i\omega)} \\
&= -[1 + \bar{g}(K, i\omega)\Sigma_d(k, i\omega)]^{-1}.
\end{aligned}
\tag{5.38}
$$

Similar relations hold for many-particle vertex functions. With the help of the two-particle vertex function we can now express the corresponding susceptibility as $\chi = \chi_0 + \chi_0 F\chi_0$. Since from Eq. (5.38) it follows that $T(k, i\omega)$ is always finite, a divergence of χ, signaling an instability or phase transition in real space, necessarily corresponds to an instability in the quantity F^d in the dual fermion space. In order to locate the instabilities, it is hence sufficient to search for a divergence of the Bethe-Salpeter equation in the dual space. For the special case when no diagrammatic corrections to the dual self-energy and vertex are taken into account, $T(k, i\omega) = -1$ and both DFDCA and DCA would produce the same phase diagram. In general cases, the DFDCA will produce results more realistic than DCA due to the inclusion of additional long-ranged correlations from the dual fermion lattice diagrammatic calculation.

5.3   Dual Fermion Diagrams

In the DFDCA formalism, the dual fermion Green function is $\mathcal{O}(1/L_c)$(c.f. Eq. (5.28)), i.e., it acts as the small parameter in the diagrammatic expressions. In addition, in the strong coupling limit, the Green function is proportional to the hopping t/U,[51] so each Green function leg contributes a factor of $\mathcal{O}((t/U)/L_c)$. In the weak coupling limit, the Green function remains $\mathcal{O}(1/L_c)$, but the vertices are now small, with the two-body vertex behaving like $\mathcal{O}(U/t)$, the three-body vertex like $\mathcal{O}(U^2)$, and so on. Each two-body diagrammatic insertion, composed of a two-body vertex and two dual fermion Green function legs, then scales like $\mathcal{O}(1/L_c^2)$, with an additional factor of U or t^2 in the weak and strong coupling limits, respectively. Each three-body diagrammatic insertion, composed of a three-body vertex and three dual fermion Green function legs, scales like $\mathcal{O}(1/L_c^3)$ with additional factors U^2 or t^3 in the weak and strong coupling limits, respectively.
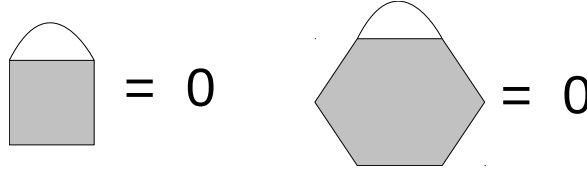

Figure 5.2: Lowest order contributions to the dual fermion self-energy from the two-body interaction (left) and to the two-body interaction from the three-body term (right). Since the bare n-body vertices depend only upon the small cluster K, the dual Green function line may be coarse-grained and are therefore zero according to Eq. (5.22).

The boundary condition Eq. (5.22) also constraints the diagrammatics. For example, the first-order contribution to the dual self-energy from the 2-body interaction is the Hartree-Fock contribution shown in Fig. 5.2. Since the vertex depends only upon the small cluster K, the dual Green function line may be coarse-grained. The result is zero by virtue of Eq. (5.22). Physically, this term must be zero since the Hartree term is already included in the cluster contribution to the self-energy. Therefore, the first finite contribution to the dual fermion self-energy comes from the second order graph which contains three dual fermion Green function lines. This and all higher order contributions described by the Schwinger-Dyson equation already are of order $\mathcal{O}(1/L_c^3)$, or smaller. Therefore, the fully dressed dual fermion Green function retains the scaling of the bare dual fermion Green function

$$G_d(k, i\omega) \sim \mathcal{O}(1/L_c) \tag{5.39}$$

as anticipated earlier.

Similarly, the first-order 3-body contribution to the dual two-body vertex, also shown in Fig. 5.2, is zero. To see this, suppose the top leg is labeled by momentum $k = K + \tilde{k}$. Since the remainder of the 3-body vertex does not depend upon $\tilde{k}$, we may freely sum over this label. Again, the result is then zero through Eq. (5.22).

41

As the cluster size becomes large, the DFDCA cluster problem may be accurately solved using low order perturbation theory, keeping only the 2-body interaction vertex. As described above, two-body vertex insertion contributes an extra factor of $\mathcal{O}(1/L_c^2)$, while three-body vertex insertion contributes an extra factor of $\mathcal{O}(1/L_c^3)$. It is therefore possible to use standard perturbation theory based on a two-body vertex to solve the dual fermion DCA cluster problem, with an accuracy which turns out to be at least of order $\mathcal{O}(1/L_c^4)$.

For example, simple second order perturbation theory yields a self-energy $\mathcal{O}(1/L_c^3)$. Two-body corrections, composed of a two-body vertex and two further Green function legs will contribute an extra factor $\mathcal{O}(1/L_c^2)$. The first three-body contribution is the second order graph composed of one 2-body vertex and one 3-body vertex. It has four internal Green function legs, and is of order $\mathcal{O}(1/L_c^4)$ so that the first three-body correction is smaller than the simple second order dual fermion self-energy composed of 2-body vertices by a factor of $\mathcal{O}(1/L_c)$. Self consistency, needed to impose the boundary condition Eq. (5.22), is more important for the self-energy than higher order or three-body contributions.

Generally, the leading non-trival n-body ($n \geq 3$) vertex contribution to the self-energy is constructed from an n-body vertex and an $(n-1)$-body vertex, which are connected by $(2n-2)$ internal legs, as shown in Fig. 5.3. Thus this contribution scales as $\mathcal{O}(1/L_c^{2n-2})$.
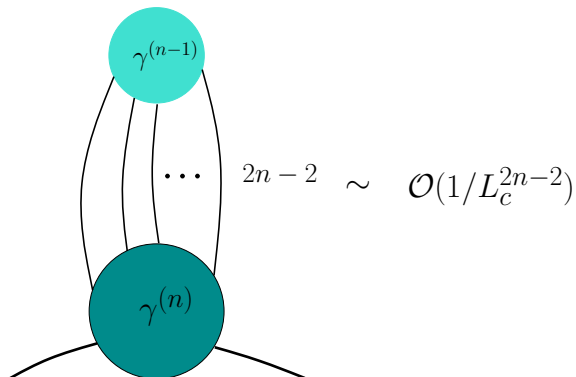

Figure 5.3: Leading non-trivial n-body vertex contribution to the self-energy. It is contructed by one n-body vertex and one (n-1)-body vertex. Since there are (2n-2) internal legs, this contribution scales as $\mathcal{O}(1/L_c^{2n-2})$.

As another example, consider the equation for a transition, in the pairing matrix formalism (Fig. 5.4)

$$\Gamma_d \chi_d^0 \Phi = \Phi \tag{5.40}$$

where Φ is the leading eigenvector of the pairing matrix $\Gamma_d \chi_d^0$. A transition is indicated by the corresponding eigenvalue approaching one. To lowest order, the irreducible dual fermion vertex $\Gamma_d \approx \gamma$ is just the bare dual fermion interaction, and the legs in χ_d^0 are not dressed by the dual fermion self-energy. In this case the transition temperatures of

the DCA are reproduced (e.g., see Fig. 5.5). The lowest order corrections to the DCA come from the second order corrections to the vertex, which contain two dual fermion Green function legs and are therefore $\mathcal{O}(1/L_c^2)$. The low order contributions to χ_d^0 are $\chi_d^0 \approx G_d^0(1 + \Sigma_d G_d^0 + \cdots)G_d^0$, and thus the lowest relative correction to χ_d^0 is of order $\mathcal{O}(1/L_c^4)$. Therefore, the cross channel second order corrections to the vertex are more important than the second-order corrections to the self-energy when the DCA cluster size is large. We note that this is not only true for the DFDCA, but also for the DFDMFA in the strong coupling limit where the small parameter t/U replaces $1/L_c$. Furthermore, higher order approximations such as the ladder approximation that do not include these cross channel contributions are not appropriate for the solution of the dual fermion lattice in the limit of large DCA cluster size or small t/U.

Figure 5.4: (a) Equation for T_c. Transition temperatures on the dual fermion lattice are identical to those calculated on the real lattice. (b) The low order corrections to the dual fermion irreducible vertex Γ_d. The second order terms are of the order $\mathcal{O}(1/L_c^2)$ with corrections $\mathcal{O}(1/L_c^3)$. (c) Contributions to the dual fermion self-energy. It is dominated by the second-order term which is of the order $\mathcal{O}(1/L_c^3)$ with corrections $\mathcal{O}(1/L_c^4)$. The self-energy adds relative corrections to χ_d^0 of order $\mathcal{O}(1/L_c^4)$ (see the text for the detail), so the most important contributions to the equation for T_c come from the second-order cross channel contributions to Γ_d.

Higher order approximations like the fluctuation-exchange approximation (FLEX) [6], which include the cross channel contributions to Γ_d, should on the other hand be quite accurate. In fact, the FLEX contains all two-particle diagrams to third order. The first diagram neglected by the FLEX is composed of one three-body and one two-body vertex and would contribute a correction $\mathcal{O}(1/L_c^4)$ to the self-energy or $\mathcal{O}(1/L_c^3)$ to the vertices.

5.4 Results

In this section, we will present numerical results from a DFDCA calculation, where the interaction expansion continous-time quantum Monte Carlo method[52] is employed to solve the cluster problem within the DCA calculation. We will restrict the discussion
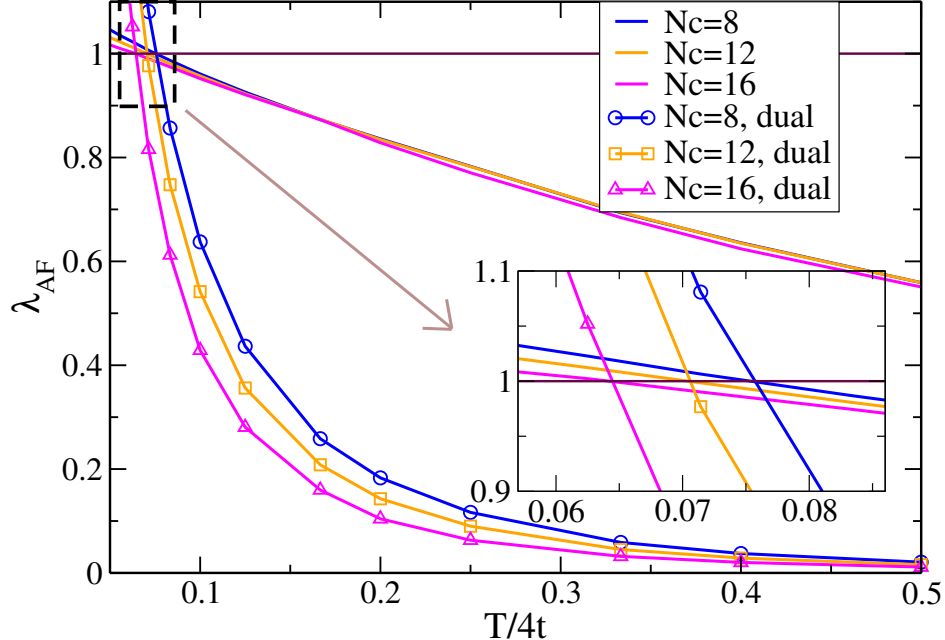
Figure 5.5: (Color online) Plots of leading eigenvalues for different cluster sizes for the anti-ferromagnetic channel with $U = 6t$ and filling $\langle n \rangle = 0.95$. Lines without symbols are results from the DCA calculation for clusters with sizes $N_c = 8$, 12 and 16, while lines with symbols are results from the DFDCA calculation without self-energy correction. For the latter, we have used a linear size of the dual fermion lattice as large as several hundreds ($N = L \times L$, $L \sim 200$). The inset is an enlarged view around the transition point. Note that both calculations produce the same transition temperatures as expected.

to the two-dimensional Hubbard model on the square lattice with only nearest neighbor hopping. Thus, for half-filling we expect strong antiferromagnetic correlations, which will drive an antiferromagnetic transition within DCA. In this case, as the Mermin-Wagner theorem prohibits long-range order except at zero temperature, we expect strong renormalization of the Néel temperature, T_N, from DFDCA.

To check the correctness of our implementation of the DFDCA approach, we first carry out calculations with the correction from the dual fermion lattice turned off. For this trivial case, one expects DFDCA to reproduce the same physics as DCA. Fig. 5.5 displays the leading eigenvalues for different cluster sizes at filling $\langle n \rangle = 0.95$ for the antiferromagnetic channel. Note that for each cluster size, both the DFDCA and the DCA leading eigenvalues cross the line $\lambda = 1$ at the same temperature, which is the mean-field Néel temperature, and that with increasing cluster size T_N decreases, as expected. It is also interesting to note that the DFDCA provides a sensitive way to monitor the finite-temperature transitions since the DFDCA leading eigenvalues have a steeper slope when crossing the $\lambda = 1$ line.

For the non-trivial DFDCA calculation, we expect to see for a fixed cluster size a reduction of the Néel temperature since correlations beyond the cluster scale are now
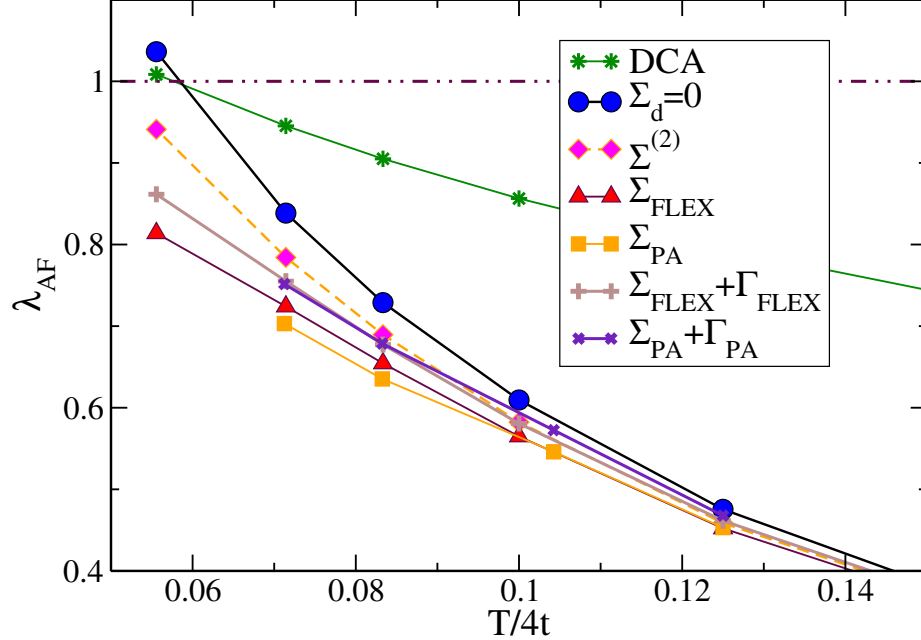
Figure 5.6: (Color online) Plots of leading eigenvalues for the anti-ferromagnetic channel. They are calculated with different approximate methods in the dual fermion lattice. The parameters used are $U = 4t$, $\langle n \rangle = 1$, the DCA cluster of size $N_c = 1$, and the dual fermion lattice of a size $N = 4 \times 4$.

incorporated by the dual fermion calculation. For the dual fermion lattice, we employ different approximation schemes: the self-consistent second-order perturbation theory (SOPT), FLEX and the parquet approximation (PA) [36]. The results are collected in Fig. 5.6, where the power of DFDCA manifests itself clearly. The simple second-order correction from the self-energy is already able to reduce the Néel temperature by ten percent. Taking into account more Feynman diagrams with higher orders, for example by FLEX or PA, continues to reduce the Néel temperature. However, the inclusion of vertex correction tends to increase the Néel temperature again. For example, the eigenvalues labeled Σ_{FLEX} are calculated with a bare dual fermion vertex and FLEX dressed legs, while those labeled $\Sigma_{FLEX} + \Gamma_{FLEX}$ are calculated with both FLEX dressed legs and vertex (see b and c in Fig. 5.4 for contributions up to second-order in the bare dual fermion vertex γ).

Up to now we have only discussed the leading eigenvalues of the vertex function. Of course, the DFDCA also allows to calculate the full susceptibility from the Bethe-Salpeter equation. Two typical results for an $N_c = 2 \times 2$ DCA cluster are shown in Fig. 5.7, as function of temperature for $U = 8t$. In the left panel, the inverse staggered susceptibility for half filling is displayed, while the right one contains results for the inverse d-wave pairing susceptibility at a filling $\langle n \rangle = 0.95$. Due to the heavy computational cost for the parquet calculation, here we only use the SOPT and FLEX in our dual fermion lattice calculation. Although $L_c = 2$ is not really large, the DFDCA is still able
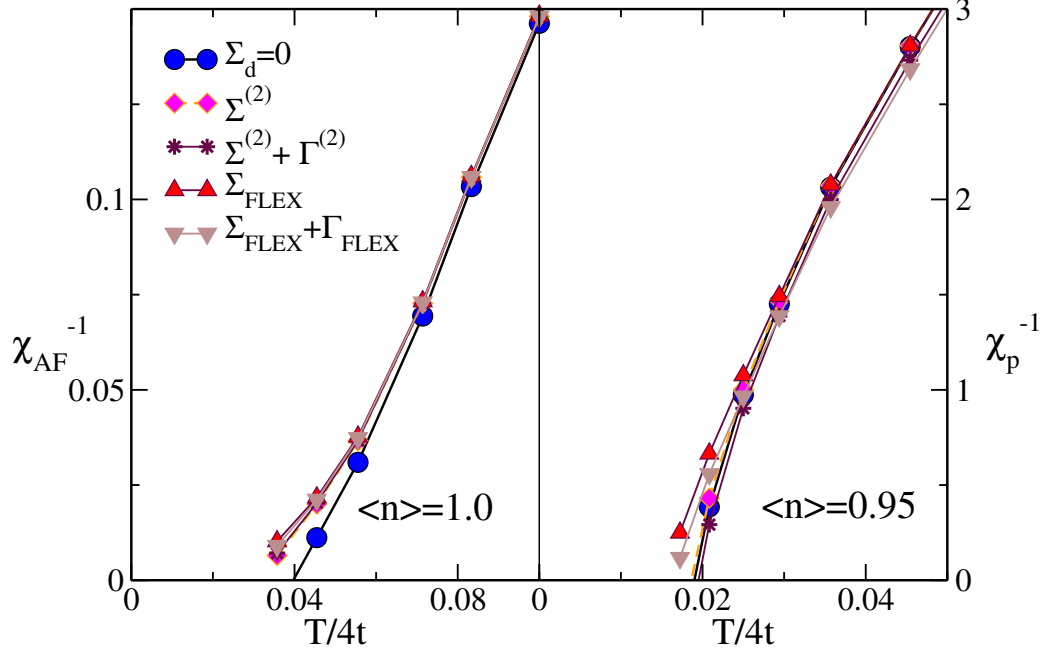
Figure 5.7: (Color online) Plots of the inverse anti-ferromagnetic and d-wave pairing susceptibilities calculated with different approximate methods in the dual fermion calculation. The parameters used are $U = 8t$ and $N_c = 4$. The linear dependence of the results with $1/L^2$ (see Fig. 5.8) is used to extrapolate the $L = \infty$ limit results.

to significantly reduce the mean-field Néel and the abnormally large superconducting transition temperatures.

It is quite interesting to note, that for the anti-ferromagnetic channel at half-filling, SOPT and FLEX produce similar results, both being different from the DCA results. The effect of vertex correction is small in this case. For the d-wave pairing susceptibility at $\langle n \rangle = 0.95$, on the other hand, SOPT in dual space makes almost no difference from the DCA results, but the FLEX tends to significantly reduce the pairing susceptibility. Again, the inclusion of vertex correction has the opposite effect, i.e., it leads to a slight increase of the critical temperatures.

In the derivation of the DFDCA approach, we have assumed that the dual fermion lattice is infinite. However, in practical calculations, the size is limited due to the algebraic increase of the computational cost. This results in some deviations from the infinite size system. Fig. 5.8 shows the L ($N = L \times L$) dependence of the leading eigenvalues for different DCA clusters. The nice linear dependence of the leading eigenvalues on $1/L^2$ can be readily observed. This is due to the periodic boundary conditions used in the dual fermion calculation. This property allows us to reduce the computational cost of our calculation by using two small $L's$ and extrapolating to obtain a rather accurate approximation of the $L = \infty$ result.
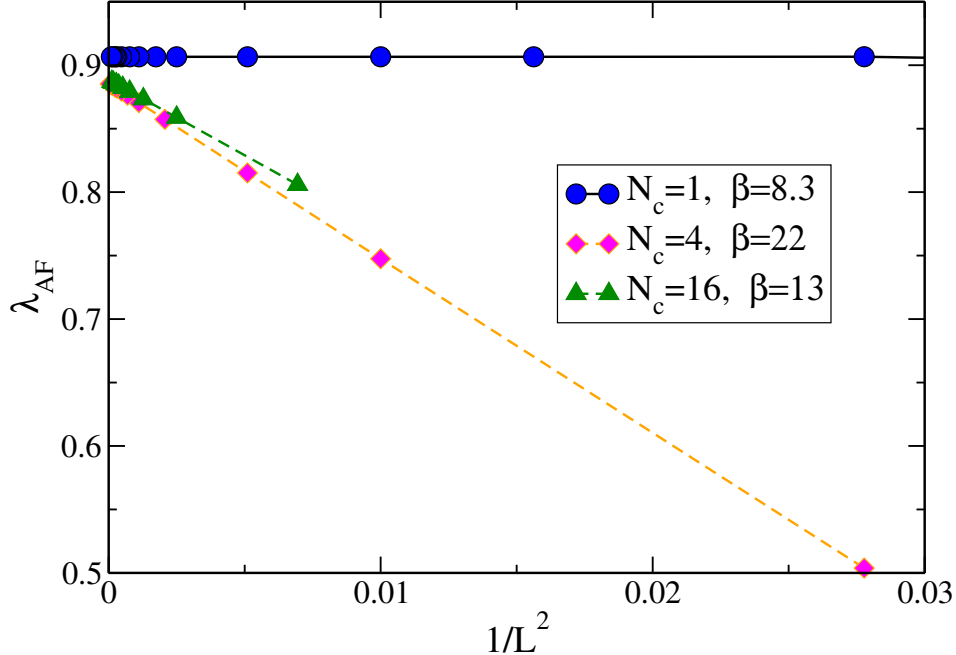
Figure 5.8: (Color online) The L dependence of the leading eigenvalue for different DCA clusters. The parameters used are $U = 8t$, $\langle n \rangle = 1$, $\Sigma_{dual} = 0$ and $\beta = 4t/T$. The nice linear dependence of $1/L^2$ can be readily observed, which is due to the periodic boundary conditions used in the dual fermion calculation.

5.5   Discussion

The dual fermion mapping as discussed in section 5.2 is exact, and the approximation is made only when performing the diagrammatic calculation for the dual fermion lattice. Justified by the scaling behavior of the dual fermion Green function, it suffices to consider the 2-body term of the interaction and use low order perturbation theory. Correlations beyond the DCA cluster size are systematically restored through the dual fermion calculation on the lattice. In this sense, the DFDCA can be seen as a diagrammatic expansion around DCA. This is manifested in Fig. 5.5 and 5.6 where we see that not including the dual fermion self-energy and vertex corrections reproduces the DCA transition temperature. When these corrections are included, we observe a systematic suppression of the DCA transition temperature resulting in a more realistic value. This is clearly seen in Fig. 5.6 and 5.7. Since correlations at intermediate length-scale are taken into account by the dual fermion lattice calculation, we can use small clusters in the underlying DCA calculation. As a result, we are able to greatly reduce the adverse effect of the minus sign problem encountered in QMC simulations for larger clusters, and access a wider region of parameter space.

The DFDCA has an additional advantage that it is parameterized by the full (reducible) vertex function calculated on the DCA cluster. Other multi-scale methods[45, 17, 46] rely upon the calculation of the cluster irreducible or fully irreducible vertices.

Our recent numerical experiments show that inverting the Bethe-Salpeter equation to obtain the irreducible vertex, which is also the first step in the calculation of the fully irreducible vertex, fails in some parameter regions, especially for large U or near half filling. This difficulty is avoided in the DFDCA.

The dual fermion mapping also assumes that the dual fermions are treated on an infinitely large lattice. In practice however, they are treated on a finite-size lattice. Thanks to the finite-size scaling behavior observed in Fig. 5.8, finite-size calculations are used to extrapolate to the infinite-size lattice, leading to a reduction of the computational cost in the dual fermion lattice calculation.

Note that in the calculations presented here, we have not performed the full self-consistency where the dual fermion result is used to determine the DCA cluster hybridization that is fed back into the DCA calculation until convergence. However, this first iteration already produces more satisfactory values for the Néel temperature as well as the d-wave superconducting transition temperature. We can anticipate that the full self-consistency will further improve the performance of this approach.

With the full self-consistency implemented and tested, we are planning to apply this approach to map out the phase diagram for the 2-D Hubbard model in the hole-doped region. In addition, we are also working on applying this approach to the Falicov-Kimball model and the Anderson disorder model recently.

5.6 Conclusion

We have designed a new multi-scale many body approach, the dual fermion dynamical cluster approach (DFDCA), by combining the DCA and the recently introduced dual fermion formalism. The DFDCA uses both single and two particle quantities calculated in DCA as the input for the dual fermion calculation. Different self-consistent diagrammatic approximations can be used in the dual fermion lattice, which systematically restores the long-ranged correlation ignored during the DCA calculation.

This approach is a systematic expansion around the DCA calculation. Our numerical experiments show that the zeroth order result ($\Sigma_d = 0$) reproduces the original DCA, and for any non-trivial dual fermion calculation, it is an improvement on the DCA calculation. We applied different self-consistent diagrammatic methods, self-consistent 2nd-order, FLEX and parquet approximation, on the dual fermion lattice. They all improved the DCA calculation by reducing the mean-field Néel temperature by different amounts. In addition, the abnormally large superconducting transition temperature of the four site cluster calculation can be reduced by this approach as well.

Chapter 6

Response to Dynamical Modulation of the Optical Lattice for Fermions in the Hubbard Model

In this chapter, we studied the responses to dynamical modulation of the optical lattice potential by studying properties of the repulsive fermionic Hubbard model in an optical lattice. With the help of quantum Monte Carlo simulations and Maximum Entropy Method as well as Hubbard-I approximation, the numerical evidence shows that the modulations by on-site local interaction cannot be ignored, and can even strongly contribute to the dynamical behaviors of the system in highly-doped cases. The filling of the system plays a very important role to the responses and it also determines the non-equilibrium dynamics of the system under perturbation.

In this project, I was involved in the derivation of the formalism needed for the QMC measurement, and helped to implement the measurement part of code in the DCA code.

This work has been published in Phys. Rev. A 84, 021607(R) (2011)[53]. The following sections in this chapter are from that paper.

Reprinted by permission of "Phys. Rev. A".

6.1   Introduction

A number of key properties of strongly correlated electron systems appear to be well described by simplified tight-binding Hamiltonians. For example, the square lattice Hubbard model, with one particle per site, is known to possess the long range antiferromagnetic order manifest in the parent compounds of high temperature superconductors, whose CuO_2 sheets have square arrays of copper atoms with one hole per $3d$ shell. There are many analytic and numerical clues that suggest the doped Hubbard model might also possess the d-wave superconducting phase exhibited by the cuprates, as well as other non-trivial properties including stripes and pseudogap physics [54]. If this could be demonstrated rigorously, it would provide important insight into the mechanism of

superconductivity in these materials.

Ultracold atomic systems offer an opportunity for closer connection between experiments and calculations for such model Hamiltonians. At present, experiments on fermionic atoms are exploring temperatures T which are of the order of the hopping integral J_0, probing correlations such as double occupancy, D, and short range spin order that develops at that temperature scale. In particular, the evolution of D with the ratio of interaction strength U to hopping J_0 has been shown to indicate the presence of a Mott metal-insulator transition [55, 56]. The presence of a Mott gap in the excitation spectrum has also been inferred through peaks in D which arise through a dynamic modulation of the optical lattice depth V [55].

The possibility that such a modulation might provide a useful probe was first suggested by Kollath *et al.* [57], based on earlier work with bosonic systems [58]. Using a time dependent Density Matrix Renormalization Group method, it was shown that a peak existed in the induced double occupation at a frequency ω which matched the interaction strength U. In this treatment, the response kernel was approximated to include only changes δJ in the hopping operator, neglecting corresponding variation δU in the on-site interactions. Within this approximation, the authors emphasized that the measurement was sensitive to near neighbor spin correlations, and the exchange gap, as well as the charge gap.

This 'modulation spectroscopy' has been further explored theoretically by Huber[59] and Sensarma[60]. In the former work, the frequency dependence of the shift in D was studied in the atomic and two particle limits, and within a slave boson mean field theory. The latter work focused on observing local antiferromagnetic order at the superexchange scale. As with the earlier study of Kollath, in both of these papers, the modulation was assumed to couple only to the kinetic energy.

In this chapter, we extend previous work by studying the effect of both the modulation of the tunneling strength δJ and of the on-site interaction strength δU due to varying the optical lattice depth V, for the two dimensional repulsive fermionic Hubbard Hamiltonian. The modulation by δU is shown to be quite significant in the parameter range of interest to current experiments. We find that the filling of the system plays a very important role in the response. Crucially, through the use of Determinant Quantum Monte Carlo (DQMC) [61] and the maximum entropy method [62, 32], we provide results which treat the electron-electron correlations exactly.

6.2   Formalism

In the low energy limit, two species of repulsively interacting fermions confined to a periodic optical potential with wavelength λ and amplitude $V(t)$ can be described by the one-band Hubbard model [63],

$$\hat{H} = -J\hat{K} + U\hat{D} - \mu\hat{N}, \tag{6.1}$$

where the hopping or kinetic-energy operator is $\hat{K} = \sum_{<ij>,\sigma}[\hat{c}_{i\sigma}^{\dagger}\hat{c}_{j\sigma}+\text{h.c.}]$, $\hat{D} = \sum_i \hat{N}_{i\uparrow}\hat{N}_{i\downarrow}$ is the double occupancy, and $\hat{N} = \sum_i \hat{N}_{i\uparrow} + \hat{N}_{i\downarrow}$, the total number of particles, with $\hat{c}_{i\sigma}^{\dagger}(\hat{c}_{i\sigma})$ the fermion creation (annihilation) operator, $\sigma =\uparrow,\downarrow$ the spin index, $\hat{N}_{i\sigma} = \hat{c}_{i\sigma}^{\dagger}\hat{c}_{j\sigma}$, and μ the chemical potential. The hopping (J) and interaction (U) can be expressed as [63] $J \approx (4/\sqrt{\pi}) E_R v^{3/4} \exp(-2\sqrt{v})$ and $U \approx 4\sqrt{2\pi}(a_s/\lambda) E_R v^{3/4}$, where $v = V/E_R$ is the ratio of lattice depth to recoil energy, and a_s is the short ranged s-wave scattering length.

It is clear from these expressions that a small time-dependent modulation of V changes both J and U. Writing $V(t) = V_0 + \delta V \sin(\omega t)$ and expanding J and U in the limit $\delta V \ll V_0$ yields $\hat{H} = \hat{H}_0 + \delta\hat{H}\sin(\omega t)$ with $\hat{H}_0$ given by Eq. (6.1) with J replaced by J_0 and U by U_0, and $\delta\hat{H} = -\delta J\hat{K} + \delta U\hat{D}$ with the time-dependent perturbations

$$
\begin{aligned}
\delta J &= J_0(\frac{3}{4} - \sqrt{V_0/E_R})\frac{\delta V}{V_0} \\
\delta U &= \frac{3}{4}U_0\frac{\delta V}{V_0}
\end{aligned}
\tag{6.2}
$$

For $\delta V > 0$, we have $\delta J < 0$ and $\delta U > 0$ so that an increase in the optical lattice amplitude suppresses hopping and increases the Hubbard repulsion. We emphasize that one cannot a priori neglect δJ or δU as they can be of the same order of magnitude if using the experimental parameters as in Ref. [55].

Our aim is to understand how such a simultaneous modulation of the hopping and interaction parameters, as provided by fermions in a time-dependent optical lattice, probes fermion correlations in the Hubbard model. To this end, we study the time dependence of the average double occupancy $D(t) = \langle\hat{D}\rangle$. Within standard time-dependent perturbation theory, $D(t)$ satisfies, to linear order,

$$
D(t) = D(t_0) - i \int_{t_0}^{t} dt' \, \langle[\hat{D}(t), \delta\hat{H}(t')]\rangle_0 sin(\omega t'),
\tag{6.3}
$$

where $\langle\hat{\mathcal{O}}\rangle_0 = Z_0^{-1}Tr\,e^{-\beta\hat{H}_0}\mathcal{O}$ and $\mathcal{O}(t) = e^{i\hat{H}_0 t}\hat{\mathcal{O}}e^{-i\hat{H}_0 t}$. Equation (6.3) can be simplified by rewriting $\delta\hat{H}$ in terms of $\hat{H}_0$ as $\delta\hat{H} = (\delta J/J_0)(\hat{H}_0 + U_0[\alpha - 1]\hat{D})$, with $\alpha = (1-\frac{4}{3}\sqrt{V_0/E_R})^{-1}$. When inserted into Eq. (6.3), the first term will give a vanishing contribution, leading to

$$
D(t) = D(t_0) + \frac{U_0}{J_0}(\alpha - 1) \int_{t_0}^{\infty} dt' \, \delta J \chi_{DD}(t - t')sin(\omega t'),
\tag{6.4}
$$

where $\chi_{\mathcal{O}\mathcal{O}}(t - t') = -i\langle[\hat{\mathcal{O}}(t), \hat{\mathcal{O}}(t')]\rangle_0\theta(t - t')$. Formally setting $\alpha = 0$ amounts to neglecting the modulation of the interaction term. In contrast, experimentally, α typically varies within the range $-0.41 < \alpha < -0.28$. The simplification leading to Eq. (6.4), can be generalized to show that $\chi_{\text{DD}}(t) = (J_0/U_0)^2\chi_{\text{KK}}(t)$, a fact that we shall use below in our analysis.

Numerically, we calculate the imaginary-time quantity $\chi_{DD}(\tau)$ from Determinant Quantum Monte Carlo simulations [61] and analytically extrapolate to the corresponding imaginary part of the real frequency quantity $\chi''_{DD}(\omega)$ by inverting

$$\chi_{DD}(i\nu_n) = -\frac{1}{\pi} \int_{-\infty}^{\infty} d\omega \, \frac{\chi''_{DD}(\omega)}{i\nu_n - \omega},\tag{6.5}$$

via the Maximum Entropy method [62, 32]. In Eq. 6.5 $i\nu_n = 2n\pi T$ is the bosonic Matsubara frequency, T is the temperature, and ω the real frequency.

6.3 Results
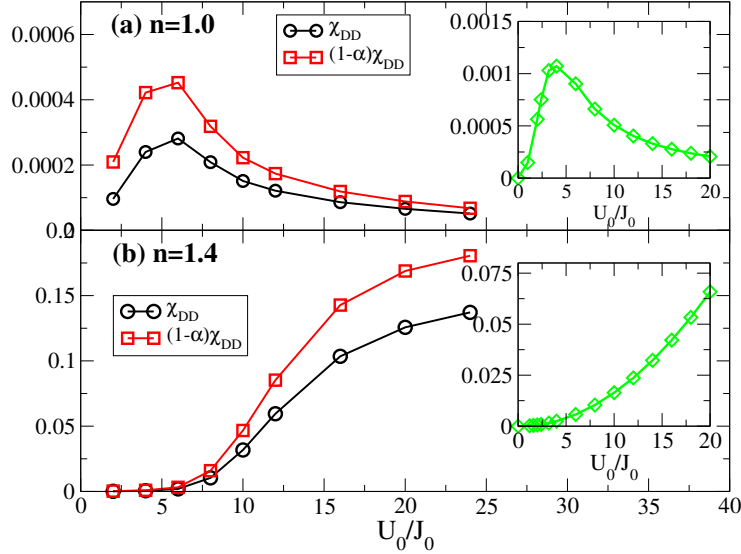
Figure 6.1: (Color online). Top panel (a) shows data for half filling, and panel (b) for a filling of $n = 1.4$, for a two-dimensional 4×4 Hubbard lattice. Red curves (squares) show the quantity $(1 - \alpha)\chi_{DD}$, that appears in the linear response of the double occupancy, evaluated at zero Matsubara frequency as a function of U_0/J_0. Neglecting the modulation of the Hubbard interaction amounts to setting $\alpha = 0$, yielding a smaller result (black curve, circles). For comparison, the green diamonds in the insert in both (a) and (b) are exact results for $(1 - \alpha)\chi_{DD}$ for a two-site Hubbard model. α is determined by assuming $a_s/\lambda = 0.0119$, where $a_s = 240a_0$ (a_0 is Bohr radius) and $\lambda = 1,064$ nm (following Ref. [55]), thus α can be found as a single-valued function of U_0/J_0.

To illustrate the importance of incorporating the modulation of the interaction parameter U, in Fig. 6.1 we show the dependence with U_0/J_0 of the double-occupancy response function $\chi_{DD}(i\nu_n = 0)$ (black curves), for $n = \langle n_{i\uparrow} + n_{i\downarrow} \rangle = 1.0$ and $n = 1.4$ along with this quantity multiplied by $(1 - \alpha)$ (red curve). Therefore, the black curves

is the result from modulating δJ only, while the red curve also includes the effect of modulating δU. The difference between the curves illustrates that δU should not be neglected. We observe from Fig. 6.1 that at half-filling (n=1), the double occupancy response is largest in the intermediate interaction region and decreases with increasing U_0/J_0. This is in striking contrast to the behavior at $n = 1.4$, in which the double occupancy response is small at weak coupling and saturates at large U_0/J_0. To confirm our numerical calculation, we analytically solved the case of a two-site Hubbard model and found qualitatively similar behavior. (See green curves in Fig. 6.1.)
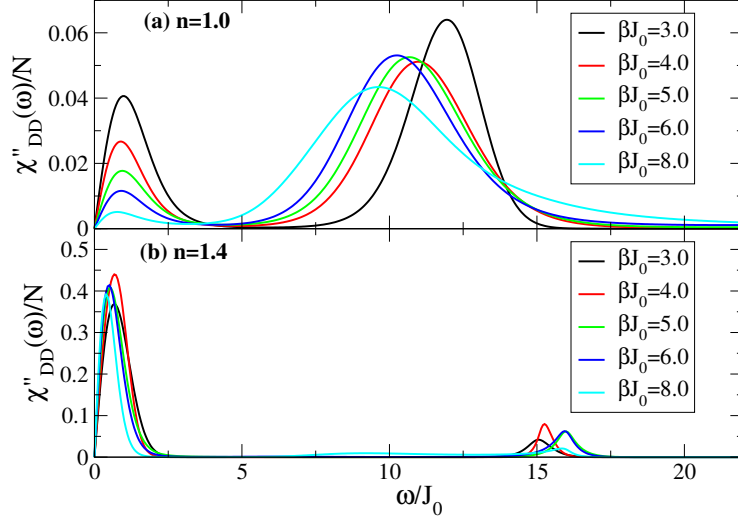

Figure 6.2: (Color online). The imaginary component of the double-occupancy susceptibility $\chi''_{\mathrm{DD}}(\omega)/N$ for $U_0/J_0 = 10.0$, a 4×4 square lattice, and various values of inverse temperature ($\beta = 1/T$). Panel (a) shows half-filling $n = 1.0$ results, and panel (b) a filling of $n = 1.4$. $N = 16$ is the system size.

We now turn to the full frequency dependent dynamical susceptibility, which determines the response to the dynamical modulation, showing its evolution as a function of temperature (expressed in terms of $\beta J_0 = J_0 \beta_B T$) in Fig. 6.2. Panel (a) displays results at half-filling, where Mott-insulating physics dominates. At this filling the low frequency response is strongly suppressed for temperatures approaching zero (so that this quasi-peak represents thermally-excited states, not coherent excitations), with the predominant response occurring at frequencies close to U_0. This energy scale, corresponding to the Mott gap, is consistent with recent experimental results [55] which find a strong response in the double occupancy when $\omega \sim U_0$. The presence of the Mott gap also accounts for the much smaller values of χ'' in the top panels of Figs. 6.1 and 6.2. Panel (b) shows a filling $n = 1.4$, where an $\omega = 0$ peak remains robust for $T \to 0$. We attribute this peak to the presence of gapless excitations reflecting Fermi liquid behavior in this region. The peak at high ω represents coherent excitations at the band-gap scale which should be the distance between the lower and upper Hubbard bands.

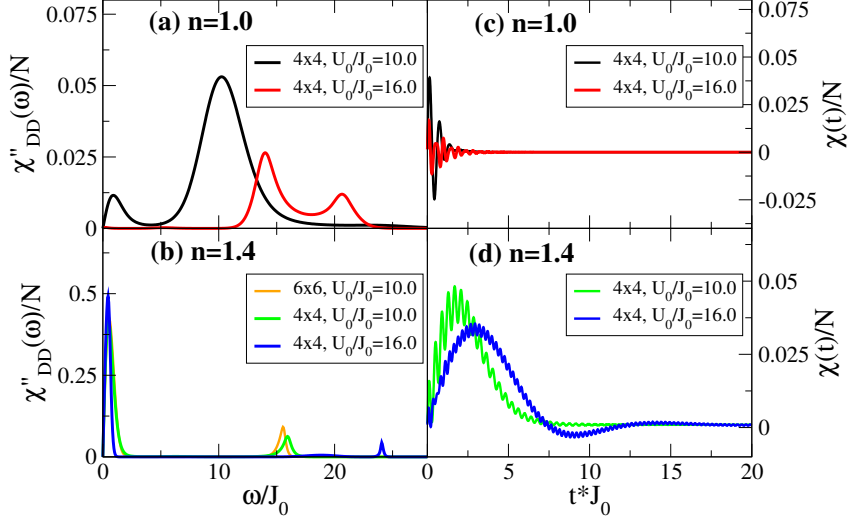In Fig. 6.3, we show the interaction dependence of $\chi''_{\mathrm{DD}}(\omega)$. Panel (a) displays the half-

Figure 6.3: (Color online). Left column: The imaginary part of the double-occupancy susceptibility $\chi''_{DD}(\omega)/N$ for $U_0/J_0 = 10$ and 16. Panel (a) shows half-filling $n = 1.0$ results for a 4×4 lattice, $U_0/J_0 = 10.0$ (black solid curve) and $U_0/J_0 = 16.0$ (red solid curve). Panel (b) shows results for a filling $n = 1.4$ and for $U_0/J_0 = 10.0$, 6×6 square lattice (orange curve), $U_0/J_0 = 10.0$, 4×4 (green curve), and $U_0/J_0 = 16.0$, 4×4 (blue curve). Right column: The real-time double-occupancy response function $\chi_{DD}(t)$ for a 4×4 square lattice at half filling (panel (c)) for $U_0/J_0 = 10.0$ (black solid curve) and $U_0/J_0 = 16.0$ (red solid); and for $n = 1.4$ (panel (d)) with $U_0/J_0 = 10.0$ (green curve) and $U_0/J_0 = 16.0$ (blue curve). All results are at a temperature $T/J_0 = 2/3$.

filled case where the peaks are centered at U_0. In panel (b), filling $n = 1.4$, we include the case of a larger lattice size (6×6) to show that finite size effects are small. These results further verify the important role of filling in the response to dynamical modulation. Our findings can be qualitatively reproduced by neglecting vertex corrections in χ_{KK} and expressing the single particle Green's function in the Hubbard-I approximation. The latter corresponds to using a approximate self-energy of the form

$$\Sigma_\sigma(\omega) \sim \frac{U_0^2\, n_{\bar{\sigma}}(1 - n_{\bar{\sigma}})}{\omega + i\delta}. \tag{6.6}$$

We find that $\chi''_{KK}(\omega)$ (and hence $\chi''_{DD}(\omega)$) possess poles at $\omega \sim 0, \pm\sqrt{(\epsilon_{\boldsymbol{k}})^2 + 4U_0^2\, n_\sigma(1 - n_\sigma)}$, where $\epsilon_{\boldsymbol{k}}$ is the energy of a non-interacting quasiparticle with momentum $\epsilon_{\boldsymbol{k}}$. In the low energy region, there are quasi-elastic peaks at approximately $\omega \sim 0$. Note that the peak vanishes at $\omega = 0$ because the imaginary part of the real frequency susceptibility is an odd function $\chi''_{KK}(-\omega) = -\chi''_{KK}(\omega)$. In the high energy region, the peaks are located at roughly $\omega \sim U_0 + \dfrac{\epsilon_{\boldsymbol{k}}^2}{2U_0}$. Therefore, at half-filling, the peaks are at $\omega = U_0$ but they sit at higher frequencies away from half filling.

We now turn to the question of how the features in $\chi_{DD}(\omega)$ would be reflected in a

experimental measurement of the double occupancy, by inserting our results for $\chi_{\mathrm{DD}}(t)$ into Eq. (6.4). For this task, we need to obtain the real part of $\chi_{\mathrm{DD}}(\omega)$ via Kramers-Kronig; upon Fourier transforming we find the real-time dynamical response functions for the double occupancy to be strikingly different at half filling and away from half filling, as seen in panels (c) and (d) of Fig. 6.3. We see that filling $n = 1$ shows a response function that is tightly peaked at $t \to 0$, characterized by a single frequency scale $\omega \sim U_0$, while at $n = 1.4$ we see a broad behavior dominated by the two distinct frequencies associated with $\omega \sim 0$ and $\omega \sim U_0 + \dfrac{\epsilon_{\boldsymbol{k}}^2}{2U_0}$.
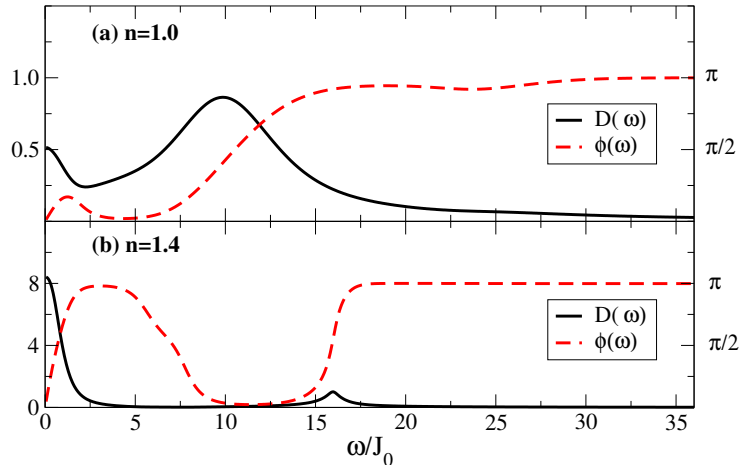
Figure 6.4: (Color online). The frequency dependence of the double occupancy linear response for a 4×4 lattice, interaction strength $U_0/J_0 = 10.0$, and temperature $T/J_0 = 2/3$. Panel (a) shows half-filling results; panel (b), $n = 1.4$. Solid (black) curves shows the amplitude $D(\omega)$ while the dashed (red) curves display the phase shift $\phi(\omega)$ induced by the dynamical modulation.

As in standard linear response theory, the real and imaginary parts of $\chi_{\mathrm{DD}}(\omega)$ correspond to the in-phase and out of phase parts of the response, respectively. Thus, to linear order, an oscillatory driving of the optical lattice potential yields an oscillatory response at the same frequency, but with a phase lag characterized by the ratio of $\tan\phi(\omega) = \chi_{\mathrm{DD}}''(\omega)/\chi_{\mathrm{DD}}'(\omega)$. This response has recently been observed directly [64]. We can then write the time-dependent double occupancy as

$$D(t) = D(0) + D(\omega)sin[\omega t - \phi(\omega)] \qquad (6.7)$$

where $D(\omega) = U_0/J_0(\alpha - 1)\delta J|\chi_{\mathrm{DD}}(\omega)|$. We plot $D(\omega)$ and $\phi(\omega)$ in Fig. 6.4 for the case of $U_0/J_0 = 10$. We first note that, at low frequency $\omega \to 0$, Eq. (6.7) implies the time dependence of $D(t)$ to be precisely π out of phase with $\delta V(t)$. Therefore, an adiabatic increase of the optical lattice amplitude leads to a corresponding *suppression* of the double occupancy. At higher ω these plots show how the time-dependent linear response of the double occupancy probes the underlying fermion correlations. As we

expected, the half filled case shows the strongest response when the driving frequency $\omega \sim U$, and with a phase that is shifted, by $\phi \approx \pi/2$, relative to the imposed modulation. At $\langle n \rangle = 1.4$, however, the predominant response is for $\omega = 0$, with phase shift $\phi \approx 0$.

6.4 Conclusion

In conclusion, we have investigated the dynamical properties of fermions in an optical lattice, realized by the Hubbard model subject to a periodic optical lattice modulation. We show that the modulation of the on-site interaction cannot be neglected and that, even at the level of linear response, the dynamical double occupancy provides a sensitive probe of fermion correlations. Recent cold-atom experiments [64] studying the dynamical modulation of the optical lattice find a linear in time contribution to the double occupancy, known to emerge at quadratic order in the modulation parameter δV [57]. Thus, we expect that our linear-response results apply at smaller $\delta V/V_0$, or after subtracting off this t-linear contribution to focus on the oscillatory component. A future extension of our work will analyze the linear and quadratic-order contributions in detail. In addition, the effects of inhomogeneity due to trapping effects is an issue for future calculations.

Chapter 7

General Conclusion and Outlook

Vertex decomposition technique can be used widely to analyze the underlying mechnism of the second-order phase transition. Since we have known that the proximity of the superconducting dome to the phase seperation Quantum Critical Point provides the essential glue for the forming of superconducting pairing, we might ask what the underlying driving force for the phase separation is, which will be of much theoretical importance and interest.

In the thesis, we have developed formalism for the dual fermion dynamical cluster approach, and implemented an initial working code for this method. It is far from mature, and further development is required. As a future application, we can use this method to quickly map out the phase diagram for the 2-D Hubbard model in the holed doped region. We can also apply it on the Falicov-Kimball model. For this model an analytical dynamical mean field solution exists and the dual fermion mapping results in a very simpled t-V model, rendering it an ideal paradigm to test this new approach.

The cold atom system provides a large playground for the theoretical and numerical work. One can suggest different experiments to explore new physics and vary both theoretical and numerical results. We might apply our new dual fermion approach on the cold atom system.

Bibliography

[1] M. Troyer and U.-J. Wiese. Computational complexity and fundamental limitations to fermionic quantum monte carlo simulations. *Phys. Rev. Lett.*, 94(17):170201, May 2005.

[2] D. Galanakis, S. Yang, F. F. Assaad, M. Jarrell, P. Werner, and M. Troyer. Comment on "exact bosonization for an interacting fermi gas in arbitrary dimensions". *Phys. Rev. Lett.*, 105(15):159701, Oct 2010.

[3] G. Baym and L. P. Kadanoff. Conservation laws and correlation functions. *Phys. Rev.*, 124(2):287–299, Oct 1961.

[4] G. Baym. Self-consistent approximations in many-body systems. *Phys. Rev.*, 127(4):1391–1401, Aug 1962.

[5] N. E. Bickers and S. R. White. Conserving approximations for strongly fluctuating electron systems. II. numerical results and parquet extension. *Phys. Rev. B*, 43(10):8044–8064, Apr 1991.

[6] N. E. Bickers and D. J. Scalapino. Conserving approximations for strongly fluctuating electron systems. I. formalism and calculational approach. *Annals of Physics*, 193(1):206 – 251, 1989.

[7] A.-M. S. Tremblay S. Allen and Y. M. Vilk. *Theoretical Methods for Strongly Correlated Electrons.* p. 341, Eds. D. Senechal, A. Tremblay, C. Bourbonnais (Springer-Verlag, New-York, 2004).

[8] C. de Dominicis and P. C. Martin. Stationary Entropy Principle and Renormalization in Normal and Superfluid Systems. I. Algebraic Formulation. *J. Math. Phys.*, 5:14–30, 1964.

[9] C.-X. Chen and N. E. Bickers. Numerical solution of parquet equations for the anderson impurity model. *Solid State Communications*, 82(5):311 – 315, 1992.

[10] D. W. Hess, J. J. Deisz, and J. W. Serene. Low-energy excitations in an incipient antiferromagnet. *Philosophical Magazine Part B*, 74(5):457–468, 1996.

[11] G. L. G. Sleijpen and D. R. Fokkema. BiCGstab(l) for Linear Equations involving Unsymmetric Matrices with Complex Spectrum. *Electric Transactions on Numerical Analysis*, 1:11–32, 1993.

[12] Y. Saad and M. H. Schultz. Gmres: A generalized minimal residual algorithm for solving nonsymmetric linear systems. *Electric Transactions on Numerical Analysis*, 7:856–869, 1986.

[13] D. D. Johnson. Modified broyden's method for accelerating convergence in self-consistent calculations. *Phys. Rev. B*, 38(18):12807–12813, Dec 1988.

[14] T. Paiva, R. T. Scalettar, C. Huscroft, and A. K. McMahan. Signatures of spin and charge energy scales in the local moment and specific heat of the half-filled two-dimensional Hubbard model. *Phys. Rev. B*, 63(12):125116, Mar 2001.

[15] S. Moukouri and M. Jarrell. Absence of a slater transition in the two-dimensional Hubbard model. *Phys. Rev. Lett.*, 87(16):167010, Oct 2001.

[16] J. E. Hirsch. Two-dimensional Hubbard model: Numerical simulation study. *Phys. Rev. B*, 31(7):4403–4419, Apr 1985.

[17] C. Slezak, M. Jarrell, Th. Maier, and J. Deisz. Multi-scale extensions to quantum cluster methods for strongly correlated electron systems. *Journal of Physics: Condensed Matter*, 21(43):435604, 2009.

[18] D. M. Broun. What lies beneath the dome? *Nature Physics*, 4(3):170–172, Oct 2008.

[19] S. Sachdev. Where is the quantum critical point in the cuprate superconductors? *physica status solidi (b)*, 247(3):537–543, 2010.

[20] N. S. Vidhyadhiraja, A. Macridin, C. Şen, M. Jarrell, and Michael Ma. Quantum critical point at finite doping in the 2D Hubbard model: A dynamical cluster quantum Monte Carlo study. *Phys. Rev. Lett.*, 102(20):206407, May 2009.

[21] M. Jarrell, Th. Maier, M. H. Hettler, and A.N. Tahvildarzadeh. Phase Diagram of the Hubbard Model: Beyond the Dynamical Mean Field. *EuroPhys. Letters*, 56:563–569, 2001.

[22] K. Mikelsons, E. Khatami, D. Galanakis, A. Macridin, J. Moreno, and M. Jarrell. Thermodynamics of the quantum critical point at finite doping in the two-dimensional Hubbard model studied via the dynamical cluster approximation. *Phys. Rev. B*, 80(14):140505, Oct 2009.

[23] E. Khatami, K. Mikelsons, D. Galanakis, A. Macridin, J. Moreno, R. T. Scalettar, and M. Jarrell. Quantum criticality due to incipient phase separation in the two-dimensional Hubbard model. *Phys. Rev. B*, 81(20):201101, May 2010.

[24] K. Haule and G. Kotliar. Avoided criticality in near-optimally doped high-temperature superconductors. *Phys. Rev. B*, 76(9):092503, Sep 2007.

[25] J.-H. She and J. Zaanen. BCS superconductivity in quantum critical metals. *Phys. Rev. B*, 80(18):184518, Nov 2009.

[26] C. Castellani, C. Di Castro, and M. Grilli. Non-fermi-liquid behavior and d-wave superconductivity near the charge-density-wave quantum critical point. *Zeitschrift für Physik B Condensed Matter*, 103:137–144, 1997. 10.1007/s002570050347.

[27] E.-G. Moon and A. Chubukov. Quantum-critical pairing with varying exponents. *Journal of Low Temperature Physics*, 161:263–281, 2010. 10.1007/s10909-010-0199-y.

[28] M. H. Hettler, A. N. Tahvildar-Zadeh, M. Jarrell, T. Pruschke, and H. R. Krishna-murthy. Nonlocal dynamical correlations of strongly interacting electron systems. *Phys. Rev. B*, 58(12):R7475–R7479, Sep 1998.

[29] M. H. Hettler, M. Mukherjee, M. Jarrell, and H. R. Krishnamurthy. Dynamical cluster approximation: Nonlocal dynamics of correlated electron systems. *Phys. Rev. B*, 61(19):12739–12756, May 2000.

[30] J. E. Hirsch and R. M. Fye. Monte Carlo method for magnetic impurities in metals. *Phys. Rev. Lett.*, 56(23):2521–2524, Jun 1986.

[31] M. Jarrell, Th. Maier, C. Huscroft, and S. Moukouri. Quantum Monte Carlo algorithm for nonlocal corrections to the dynamical mean-field approximation. *Phys. Rev. B*, 64(19):195130, Oct 2001.

[32] M. Jarrell and J. E. Gubernatis. Bayesian inference and the analytic continuation of imaginary-time quantum Monte Carlo data. *Physics Reports*, 269(3):133 – 195, 1996.

[33] N. Bulut, D. J. Scalapino, and S. R. White. Effective particle-particle interaction in the two-dimensional Hubbard model. *Phys. Rev. B*, 47(10):6157–6160, Mar 1993.

[34] T. A. Maier, M. Jarrell, T. C. Schulthess, P. R. C. Kent, and J. B. White. Systematic study of d-wave superconductivity in the 2d repulsive Hubbard model. *Phys. Rev. Lett.*, 95(23):237001, Nov 2005.

[35] T. A. Maier, M. S. Jarrell, and D. J. Scalapino. Structure of the pairing interaction in the two-dimensional Hubbard model. *Phys. Rev. Lett.*, 96(4):047005, Feb 2006.

[36] S. X. Yang, H. Fotso, J. Liu, T. A. Maier, K. Tomko, E. F. D'Azevedo, R. T. Scalettar, T. Pruschke, and M. Jarrell. Parquet approximation for the 4×4 Hubbard cluster. *Phys. Rev. E*, 80(4):046706, Oct 2009.

[37] T. A. Maier, A. Macridin, M. Jarrell, and D. J. Scalapino. Systematic analysis of a spin-susceptibility representation of the pairing interaction in the two-dimensional Hubbard model. *Phys. Rev. B*, 76(14):144516, Oct 2007.

[38] Y. Kuramoto. *Springer Series in Solid State Science, Eds. T. Kasuya and T. Saso*, 62:p152, 1985.

[39] W. Metzner and D. Vollhardt. Correlated lattice fermions in $d = \infty$ dimensions. *Phys. Rev. Lett.*, 62(3):324–327, Jan 1989.

[40] E. Müller-Hartmann. Correlated fermions on a lattice in high dimensions. *Zeitschrift für Physik B Condensed Matter*, 74:507–512, 1989. 10.1007/BF01311397.

[41] Th. Pruschke, M. Jarrell, and J. K. Freericks. Anomalous normal-state properties of high-T_c superconductors: intrinsic properties of strongly correlated electron systems? *Advances in Physics*, 44(2):187–210, 1995.

[42] A. Georges, G. Kotliar, W. Krauth, and M. J. Rozenberg. Dynamical mean-field theory of strongly correlated fermion systems and the limit of infinite dimensions. *Rev. Mod. Phys.*, 68(1):13, Jan 1996.

[43] G. Kotliar, S. Y. Savrasov, K. Haule, V. S. Oudovenko, O. Parcollet, and C. A. Marianetti. Electronic structure calculations with dynamical mean-field theory. *Rev. Mod. Phys.*, 78(3):865–951, Aug 2006.

[44] G. Kotliar, S. Y. Savrasov, G. Pálsson, and G. Biroli. Cellular dynamical mean field approach to strongly correlated systems. *Phys. Rev. Lett.*, 87(18):186401, Oct 2001.

[45] A. Toschi, A. A. Katanin, and K. Held. Dynamical vertex approximation: A step beyond dynamical mean-field theory. *Phys. Rev. B*, 75(4):045118, Jan 2007.

[46] H. Kusunose. Influence of spatial correlations in strongly correlated electron systems: Extension to dynamical mean field approximation. *Journal of the Physical Society of Japan*, 75(5):054713, 2006.

[47] A. N. Rubtsov, M. I. Katsnelson, and A. I. Lichtenstein. Dual fermion approach to nonlocal correlations in the Hubbard model. *Phys. Rev. B*, 77(3):033101, Jan 2008.

[48] A. N. Rubtsov, M. I. Katsnelson, A. I. Lichtenstein, and A. Georges. Dual fermion approach to the two-dimensional hubbard model: Antiferromagnetic fluctuations and fermi arcs. *Phys. Rev. B*, 79:045133, Jan 2009.

[49] H. Hafermann, G. Li, A. N. Rubtsov, M. I. Katsnelson, A. I. Lichtenstein, and H. Monien. Efficient perturbation theory for quantum lattice models. *Phys. Rev. Lett.*, 102(20):206401, May 2009.

[50] H. Hafermann, S. Brener, A. Rubtsov, M. Katsnelson, and A. Lichtenstein. Cluster dual fermion approach to nonlocal correlations. *JETP Letters*, 86:677–682, 2008. 10.1134/S0021364007220134.

[51] H. Hafermann. *Numerical Approaches to Spatial Correlations in Strongly Interacting Fermion Systems.* Cuvillier Verlag Göttingen, June 2010. ISBN 978-3-86955-347-4.

[52] Emanuel Gull, Andrew J. Millis, Alexander I. Lichtenstein, Alexey N. Rubtsov, Matthias Troyer, and Philipp Werner. Continuous-time monte carlo methods for quantum impurity models. *Rev. Mod. Phys.*, 83:349–404, May 2011.

[53] Zhaoxin Xu, Simone Chiesa, Shuxiang Yang, Shi-Quan Su, Daniel E. Sheehy, Juana Moreno, Richard T. Scalettar, and Mark Jarrell. Response to dynamical modulation of the optical lattice for fermions in the hubbard model. *Phys. Rev. A*, 84:021607, Aug 2011.

[54] D. J. Scalapino. Proceedings of the international school of physics (july 1992), edited by R.A. Broglia and J.R. Schrieffer (North-Holland, New York, 1994), and references cited therein.

[55] R. Jordens, N. Strohmaier, K. Gunter, H. Moritz, and T. Esslinger. A mott insulator of fermionic atoms in an optical lattice. *Nature*, 455(7210):204–207, September 2008.

[56] U. Schneider, L. Hackermüller, S. Will, Th. Best, I. Bloch, T. A. Costi, R. W. Helmes, D. Rasch, and A. Rosch. Metallic and insulating phases of repulsively interacting fermions in a 3D optical lattice. *Science*, 322(5907):1520–1525, 2008.

[57] C. Kollath, A. Iucci, I. P. McCulloch, and T. Giamarchi. Modulation spectroscopy with ultracold fermions in an optical lattice. *Phys. Rev. A*, 74(4):041604, Oct 2006.

[58] T. Stöferle, H. Moritz, C. Schori, M. Köhl, and T. Esslinger. Transition from a strongly interacting 1D superfluid to a mott insulator. *Phys. Rev. Lett.*, 92(13):130403, Mar 2004.

[59] S. D. Huber and A. Rüegg. Dynamically generated double occupancy as a probe of cold atom systems. *Phys. Rev. Lett.*, 102(6):065301, Feb 2009.

[60] R. Sensarma, D. Pekker, M. D. Lukin, and E. Demler. Modulation spectroscopy and dynamics of double occupancies in a fermionic mott insulator. *Phys. Rev. Lett.*, 103(3):035303, Jul 2009.

[61] R. Blankenbecler, D. J. Scalapino, and R. L. Sugar. Monte Carlo calculations of coupled boson-fermion systems. I. *Phys. Rev. D*, 24(8):2278–2286, Oct 1981.

[62] J. E. Gubernatis, Mark Jarrell, R. N. Silver, and D. S. Sivia. Quantum Monte Carlo simulations and maximum entropy: Dynamics from imaginary-time data. *Phys. Rev. B*, 44(12):6011–6029, Sep 1991.

[63] I. Bloch, J. Dalibard, and W. Zwerger. Many-body physics with ultracold gases. *Rev. Mod. Phys.*, 80(3):885–964, Jul 2008.

[64] D. Greif, L. Tarruell, T. Uehlinger, R. Jördens, and T. Esslinger. Probing nearest-neighbor correlations of ultracold fermions in an optical lattice. *Phys. Rev. Lett.*, 106(14):145302, Apr 2011.

[65] R. R. dos Santos. Introduction to quantum Monte Carlo simulations for fermionic systems. *Brazilian Journal of Physics*, 33:36 – 54, 03 2003.

[66] K. B. Efetov, C. Pépin, and H. Meier. Exact bosonization for an interacting fermi gas in arbitrary dimensions. *Phys. Rev. Lett.*, 103(18):186403, Oct 2009.

[67] M. Jarrell, Th. Maier, C. Huscroft, and S. Moukouri. Quantum Monte Carlo algorithm for nonlocal corrections to the dynamical mean-field approximation. *Phys. Rev. B*, 64(19):195130, Oct 2001.

Appendix A

Permissions

The author has the right to use the article or a portion of the article in a thesis or dissertation without requesting permission from APS, provided the bibliographic citation and the APS copyright credit line are given on the appropriate pages.
From the website of the American Physical Society (APS).

Appendix B

Minus Sign Problem for QMC Simulations

Although it has been proved that the minus-sign problem in QMC simulations is NP-hard, many people are still proposing different approaches to eliminate this minus-sign problem. Recently Efetov et al. propose an exact mapping of an interacting fermion system onto a new model that is supposed to allow sign-problem free Monte Carlo simulations. In our comment published in Phys. Rev. Lett. 105, 159701 (2010), we show that their formalism is equivalent to the standard approach of Blackenbecker, Scalapino and Sugar (BSS) for fermionic systems and has the same sign statistics and minus sign problem.

B.1 Minus-Sign Problem

For high-dimension integration, the Monte Carlo (MC) method is often the only practical method. Instead of dividing the phase space evenly and summing up all the contributions at each small cell, the MC method samples in the phase space and sum over those sampling point contributions. In this way, the complexity can be controlled with a polynomial, instead of exponential, dependence of the dimension of the system. One can use the importance sampling technique, in which the more important contributions are sampled more frequently, to accelerate the calculation.

For any physical quantity, we can measure it as

$$\langle A \rangle = \frac{1}{Z} Tr[A \, e^{-\beta H}] = \frac{\sum_c A(c) p(c)}{\sum_c p(c)}. \tag{B.1}$$

The D-dimension quantum system can be mapped into a $(D+1)$-dimension classical system by using the path integral formalism, forming the so-called quantum Monte Carlo (QMC) method. For a quantum fermionic system, it happens that the "probability" p(c) can be negative, then we cannot interpret it as the possibility weight any more. To avoid this difficulty, we separate its sign from its magnitude, namely
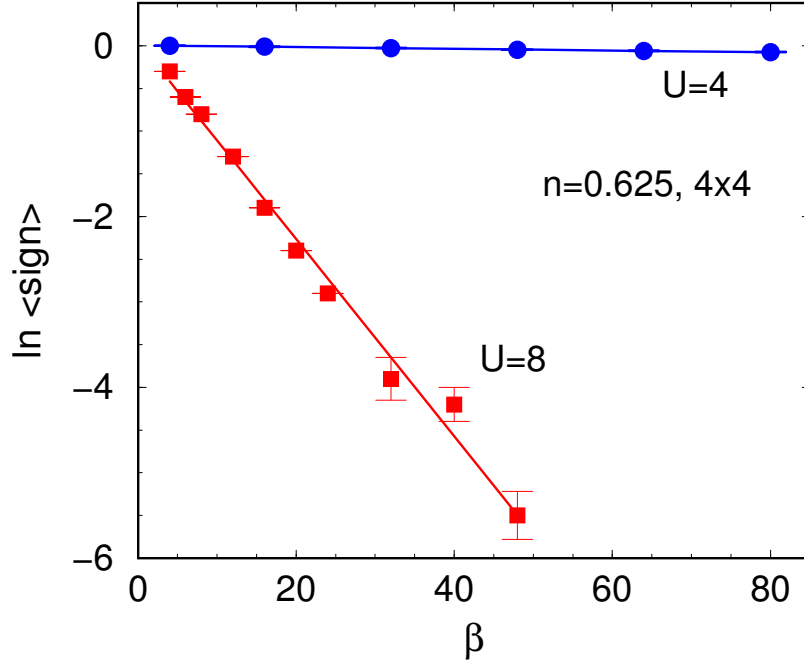
Figure B.1: (Color online) The inverse temperature dependence of the average sign. The exponential dependence can be easily identified. And the larger the Coulomb interaction, the larger the rate of the dependence. The data is from Ref. [65].

$$p(c) = s(c)|p(c)|. \tag{B.2}$$

Thus the weight is positive definite again, as required in the MC simulation. The measurement formula then has a different form

$$
\begin{aligned}
\langle A \rangle &= \frac{\sum_c A(c) s(c) |p(c)|}{\sum_c s(c) |p(c)|} \\
&= \frac{\sum_c A(c) s(c) |p(c)| / \sum_c |p(c)|}{\sum_c s(c) |p(c)| / \sum_c |p(c)|} \\
&= \frac{\langle As \rangle_{|p(c)|}}{\langle s \rangle_{|p(c)|}}.
\end{aligned}
\tag{B.3}
$$

The price we pay is that we have to measure the combination $\langle As \rangle_{|p(c)|}$ and the sign $\langle s \rangle_{|p(c)|}$. The minus sign problem is exemplified in the exponentially decreasing values of $\langle s \rangle_{|p(c)|}$ with increasing system size or decreasing temperature, see Fig. B.1 for an example.

The minus sign problem in QMC for the fermionic system is proved to be non-deterministic polynomial (NP) hard [1]. This means that there is no generic solution,

66

which only needs polynomial time, for this problem. In spite of this, a variety of new approaches aimed at solving the minus sign problem are proposed from time to time. The recently proposed bosonization scheme [66] is one of them. In the following, we will provide a comment on this proposal.

B.2   Comment on the Bosonization Proposal [1]

In a recent Letter [66] Efetov *et al.* propose an exact mapping of an interacting fermion system onto a new model that is supposed to allow sign-problem free Monte Carlo simulations. In this Comment, we show that their formalism is equivalent to the standard approach of Blackenbecker, Scalapino and Sugar (BSS) [61] for fermionic systems and has the same sign statistics and minus sign problem.

Our first observation is that the partition function for a given configuration of the auxiliary fields ϕ is the same in the standard formulation Z_f [Eq. (8) in Ref. [66]] and in their new bosonized scheme Z_b [Eq. (9)]:

$$Z_f [\phi] = Z_b [\phi].\tag{B.4}$$

This observation is trivial in the limit of the time step $\Delta\tau \to 0$, where both schemes reproduce the same partition function. Since Z_f can be negative also in this limit [61], Z_b is also not sign-positive. Both Z_f and Z_b are positive if ϕ is a smooth path [61], but restricting the configuration space to smooth paths amounts to a semi-classical approximation.

We next show that $Z_f [\phi] = Z_b [\phi]$ also holds for finite $\Delta\tau$ and piecewise constant paths where the field $\phi_r(\tau)$ is constant on the interval $[(l + 1)\Delta, l\Delta]$. Efetov *et al.*'s Eq. (9) is equivalent to $Z_b [\phi] = \mathrm{Tr} \left(e^{-\beta H_0} U_I(\beta, 0)\right)$ where $\frac{\partial}{\partial \tau_1} U_I(\tau_1, \tau_0) = -H_{I,1}(\tau_1) U_I(\tau_1, \tau_0)$ and $H_{I,1}(\tau) = -\sum_r \phi_r(\tau) e^{\tau H_0} m_{z,r} e^{-\tau H_0}$. Since $U_I(\tau_2, \tau_0) = U_I(\tau_2, \tau_1) U_I(\tau_1, \tau_0)$, $Z_b [\phi] = \mathrm{Tr} \left[e^{-\beta H_0} \prod_{n=0}^{N} U_I(l\Delta, (l - 1)\Delta)\right]$. We are left with the task of evaluating $U_I (l\Delta, (l - 1)\Delta)$ on the lth time interval where the fields are constant and take the values ϕ_{rl}. For this constant in time field configuration, $U_I(l\Delta, (l - 1)\Delta) = e^{l\Delta H_0} e^{-\Delta h_l} e^{-(l-1)\Delta H_0}$ with $H_l = H_0 - \sum_r \phi_{r,l} m_{z,r}$. Hence,

$$Z_b [\phi] = \det \left[1 + \prod_{l=0}^{N} e^{-\Delta h_l}\right] \equiv Z_f [\phi].\tag{B.5}$$

We also demonstrate that the proposed formalism is equivalent to that of BSS [61]. Starting from the expression for Z found between Eq. (9) and Eq. (10) and using a matrix notation the partition function reads

$$\ln \frac{Z_b [\phi]}{Z_0} = \int_0^1 du \sum_\sigma Tr \Phi G_\sigma,\tag{B.6}$$

---

[1] This work has been published in Phys. Rev. Lett. 105, 159701 (2010).

where Φ is a matrix with elements $\Phi\left(rl, r'l'\right) = \phi_{r,l}\delta_{rr'}\delta_{ll'}$, the trace is over the space time indices and

$$G_\sigma = G^0 + u\sigma G^0 \Phi G_\sigma = \left(1 - u\sigma G^0 \Phi\right)^{-1} G^0, \tag{B.7}$$

where G^0 is the non interacting Green function. From Eqs. (B.6) and (B.7) we get

$$\ln \frac{Z_b\left[\phi\right]}{Z_0} = \int_0^1 du \sum_\sigma Tr \frac{1}{1 - u\sigma G^0 \Phi} \sigma G^0 \Phi. \tag{B.8}$$

The integral in terms of u and σ can be carried out analytically yielding the BSS partition function

$$\begin{aligned} Z_b\left[\phi\right] &= Z_0 \exp\left(-Tr\left[\ln\left(1 - (G^0\Phi)^2\right)\right]\right) \\ &= \frac{Z_0}{\det\left(1 - (G^0\Phi)^2\right)} = \prod_{\sigma=\uparrow\downarrow} \frac{1}{\det G_\sigma}. \end{aligned} \tag{B.9}$$

A sign problem is present in Eq. (B.6), but is hidden in the u integral. If $G^0\Phi$ has eigenvalues on the real axis with absolute value greater than 1, then the u integral runs over poles. This will give phases of $i\pi$ in the exponent which can lead to negative values of the exponential.

Finally, Efetov's *et al.* suggest an alternative way of evaluating the same weight Z_b from a bosonic field $A_{rr'}\left(\tau\right)$; however, the equation of motion that A satisfies, [their Eq. (13)], is singular. Furthermore, the equation of motion cannot uniquely determine A – not even with their additional constraint $\sum_r A_{rr}\left(\tau\right) = 0$. The latter can be shown, for example, using a two site cluster and a single time slice.

In conclusion, we have shown that for piecewise continuous paths the partition function obtained from Efetov *et al.*'s method [66] is equivalent to the standard BSS formulation and has, in particular, the same sign problem. However, their method provides a new perspective on the minus sign problem, as it can be viewed as originating from poles of the coupling constant (u) integral, or as branch cuts of a logarithm when the integral over u is performed analytically.

Appendix C

Measurement of Two-Particle Green Function

In the multi-scale quantum simulations, we employ the quantum Monte Carlo (QMC) algorithm to analyze the prorperties of strongly interacting systems with small cluster sizes. Within QMC, the interacting system is cast into a non-interacting system of electorns scattered off a set of Ising fields, thanks to the Hubbard-Stratonavich transformation. The averaging of those Ising spin fields would restore the full interaction. We thus introduce an extra degree of freedom, but the benefit is that we can make use of the Wick's theorem for the non-interacting system during the QMC simulation, and we can construc n-particle Green function by the single-particle Green function readily. We are most interested in the two-particle quantities which are essential in the determination of phase diagrams. In this chapter we will show explictly how to measure the two-particle Green functions for different scattering channels in the QMC simulation.

C.1 Definitions of Green Functions

Single-particle Green's function is defined as (ignoring the k or r labels):

$$G(\tau) \equiv - < T_\tau c(\tau) c^\dagger(0) > \tag{C.1}$$

Its Fourier transform is:

$$G(i\omega_n) = \int_0^\beta e^{i\omega_n \tau} G(\tau) d\tau \tag{C.2}$$

and the inversed Fourier transform

$$G(\tau) = T \sum_{i\omega_n} e^{-i\omega_n \tau} G(i\omega_n) \tag{C.3}$$

Noting that the Green function in the imaginary time space is dimensionless, the Green's function in the frequency space thus has the inverse energy unit:

$$G(i\omega_n) \sim \frac{1}{E} \tag{C.4}$$

Note that

$$G(i\omega_n, i\omega_{n'}) \sim \frac{1}{E^2} \tag{C.5}$$

which is used in the QMC measurement.

The two-particle Green's function for the p-h channel is defined as:

$$\chi^{ph}(\tau_1, \tau_2; \tau_3, \tau_4) \equiv < T_\tau c(\tau_1) c^\dagger(\tau_2) c(\tau_4) c^\dagger(\tau_3) > - < T_\tau c(\tau_1) c^\dagger(\tau_2) >< T_\tau c(\tau_4) c^\dagger(\tau_3) > \tag{C.6}$$

while for p-p channel

$$\chi^{pp}(\tau_1, \tau_2; \tau_3, \tau_4) \equiv < T_\tau c(\tau_1) c(\tau_2) c^\dagger(\tau_4) c^\dagger(\tau_3) > \tag{C.7}$$

in which other degrees of freedom can be added accordingly as the imaginary time index.

Its Fourier transform:

$$\chi(i\nu_m)_{i\omega_n, i\omega_{n'}} = \int_0^\beta e^{(i\omega_n + i\nu_m)\tau_1} d\tau_1 \int_0^\beta e^{-i\omega_n \tau_2} d\tau_2 \int_0^\beta e^{-(i\omega_{n'} + i\nu_m)\tau_3} d\tau_3 \chi(\tau_1, \tau_2; \tau_3, 0) \tag{C.8}$$

which is of the unit:

$$\chi(i\nu_m)_{i\omega_n, i\omega_{n'}} \sim \frac{1}{E^3} \tag{C.9}$$

C.2 Particle-Particle Channel

C.2.1 Definition and Measurement

$\chi^{pp}_{\uparrow\downarrow;\uparrow\downarrow}$:
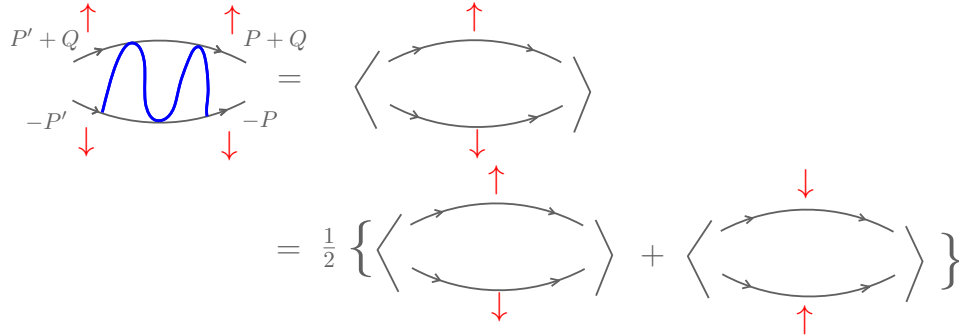
$$\chi^p(Q)_{P,P'} \equiv \chi^{pp}_{\uparrow\downarrow;\uparrow\downarrow}(Q)_{P,P'} = \frac{1}{2N_c\beta} \{ < G_\downarrow(-P, -P')G_\uparrow(P+Q, P'+Q) >_{\{QMC\}} \tag{C.10}$$
$$+ < G_\uparrow(-P, -P')G_\downarrow(P+Q, P'+Q) >_{\{QMC\}} \}$$

Note that the volume of the space-time is divided on the righ hand side of the equation to fix the dimension. $\beta \equiv 1/T$ and N_c is the number of cluster sites.

In the QMC measurement, this quantity is represented by gamats(i,j,l)=chi_p(Q)_P,P'.

$\chi^{pp}_{\uparrow\downarrow;\downarrow\uparrow}$:
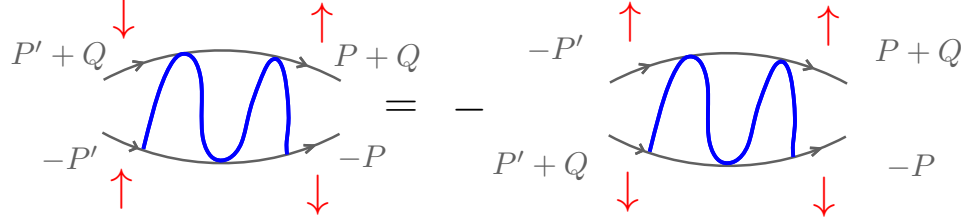
$$\chi^{pp}_{\uparrow\downarrow;\downarrow\uparrow}(Q)_{P,P'} = -\chi^p(Q)_{P,-P'-Q} \tag{C.11}$$

Here we have used the crossing symmetry, so that for the particle-particle channel, we only need to measure the quantity $\chi^{pp}_{\uparrow\downarrow;\uparrow\downarrow}$.

Singlet and Triplet Channels:

Quantities for singlet and triplet channels, if needed, can be thus defined as

$$
\begin{aligned}
\chi_{s/t}(Q)_{P,P'} &= \chi^{pp}_{\uparrow\downarrow;\uparrow\downarrow}(Q)_{P,P'} \mp \chi^{pp}_{\uparrow\downarrow;\downarrow\uparrow}(Q)_{P,P'} \\
&= \chi^p(Q)_{P,P'} \pm \chi^p(Q)_{P,-P'-Q}
\end{aligned} \tag{C.12}
$$

and for the reducible and irreducible vetices, they are

$$
\begin{aligned}
F_{s/t}(Q)_{P,P'} &= F^{pp}_{\uparrow\downarrow;\uparrow\downarrow}(Q)_{P,P'} \mp F^{pp}_{\uparrow\downarrow;\downarrow\uparrow}(Q)_{P,P'} \\
&= F^p(Q)_{P,P'} \pm F^p(Q)_{P,-P'-Q}
\end{aligned} \tag{C.13}
$$

and

$$
\begin{aligned}
\Gamma_{s/t}(Q)_{P,P'} &= \Gamma^{pp}_{\uparrow\downarrow;\uparrow\downarrow}(Q)_{P,P'} \mp \Gamma^{pp}_{\uparrow\downarrow;\downarrow\uparrow}(Q)_{P,P'} \\
&= \Gamma^p(Q)_{P,P'} \pm \Gamma^p(Q)_{P,-P'-Q}
\end{aligned} \tag{C.14}
$$

C.2.2 Bethe-Salpeter Equation for χ^p
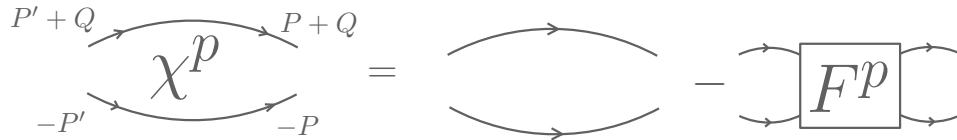
$$
\begin{aligned}
\chi^p(Q)_{P,P'} =\ & N_c\beta * G(-P)G(P+Q)\delta_{P,P'} \\
& - G(P+Q)G(-P)F^p(Q)_{P,P'}G(P'+Q)G(-P')
\end{aligned} \tag{C.15}
$$

$$\chi^p(Q)_{P,P'} = N_c\beta * G(-P)G(P+Q)\delta_{P,P'}$$
$$- \frac{1}{N_c\beta}\sum_{P''}\chi^p(Q)_{P,P''}\Gamma^p(Q)_{P'',P'}G(P'+Q)G(-P') \qquad (C.16)$$

One should be very careful about the minus sign for the second terms in the above equations. The first order contribution of U to the two-particle Green's function is

$$\chi^p(Q)_{P,P'}^{(2)} = -UG(P+Q)G(P'+Q)G(-P)G(-P') \qquad (C.17)$$

and noticing that the high-frequency limit of both F^P and Γ^P is U, thus we would have to conclude that the sign for the second terms should be minus.

If we define the un-perturbed two-particle Green's function as:

$$\chi_0^p(Q)_{P,P'} \equiv N_c\beta * G(-P)G(P+Q)\delta_{P,P'} \equiv \chi_0^p(Q)_P\delta_{P,P'} \qquad (C.18)$$

then we have

$$\chi^p(Q)_{P,P'} = \chi_0^p(Q)_{P,P'} - \frac{1}{(N_c\beta)^2}\sum_{P'',P'''}\chi^p(Q)_{P,P''}\Gamma^p(Q)_{P'',P'''}\chi_0^p(Q)_{P''',P'} \qquad (C.19)$$

Thus

$$\Gamma^p(Q)_{P,P'} = -\ (N_c\beta)^2(\chi_0^p(Q)^{-1} - \chi^p(Q)^{-1})_{P,P'} \qquad (C.20)$$

and similarly,

$$F^p(Q)_{P,P'} = -\ \chi_0^p(Q)_P^{-1}(\chi^p(Q) - \chi_0^p(Q))_{P,P'}\chi_0^p(Q)_{P'}^{-1} \qquad (C.21)$$

C.3 Particle-Hole Channel

C.3.1 Definition and Measurement

$\chi^{ph}_{\uparrow\uparrow;\uparrow\uparrow}$:

$$\chi^{ph}_{\uparrow\uparrow;\uparrow\uparrow}(Q)_{P,P'} = \frac{1}{N_c\beta}[-\frac{1}{2}\{< G_\uparrow(P',P)G_\uparrow(P+Q,P'+Q) >_{\{QMC\}}$$
$$+ \; < G_\downarrow(P',P)G_\downarrow(P+Q,P'+Q) >_{\{QMC\}}\}$$
$$+\frac{1}{2}\{< G_\uparrow(P+Q,P)G_\uparrow(P',P'+Q) >_{\{QMC\}}$$
$$+ \; < G_\downarrow(P+Q,P)G_\downarrow(P',P'+Q) >_{\{QMC\}}\}$$
$$-\frac{1}{4}\{< (G_\uparrow(P+Q,P) + \; G_\downarrow(P+Q,P)) >_{\{QMC\}})$$
$$< (G_\uparrow(P',P'+Q) + G_\downarrow(P',P'+Q)) >_{\{QMC\}}\}] \quad (C.22)$$

$\chi^{ph}_{\uparrow\uparrow;\downarrow\downarrow}$:

$$\chi^{ph}_{\uparrow\uparrow;\downarrow\downarrow}(Q)_{P,P'} = \frac{1}{N_c\beta}[\frac{1}{2}\{< G_\uparrow(P+Q,P)G_\downarrow(P',P'+Q) >_{\{QMC\}}$$
$$+ < G_\downarrow(P+Q,P)G_\uparrow(P',P'+Q) >_{\{QMC\}}\}$$
$$-\frac{1}{4}\{< (G_\uparrow(P+Q,P)+ G_\downarrow(P+Q,P)) >_{\{QMC\}})$$
$$< (G_\uparrow(P',P'+Q)+G_\downarrow(P',P'+Q)) >_{\{QMC\}}\}] \quad (C.23)$$

χ^{ph}_{d}:

74

$$
\begin{aligned}
\chi_d^{ph}(Q)_{P,P'} &= \chi_{\uparrow\uparrow;\uparrow\uparrow}^{ph}(Q)_{P,P'} + \chi_{\uparrow\uparrow;\downarrow\downarrow}^{pp}(Q)_{P,P'} \\
&= \frac{1}{N_c\beta}\Big[-\frac{1}{2}\{< G_\uparrow(P',P)G_\uparrow(P+Q,P'+Q) >_{\{QMC\}} \\
&\quad + \; < G_\downarrow(P',P)G_\downarrow(P+Q,P'+Q) >_{\{QMC\}}\} \\
&\quad +\frac{1}{2}\{< (G_\uparrow(P+Q,P)+ \; G_\downarrow(P+Q,P)) \\
&\qquad (G_\uparrow(P',P'+Q)+G_\downarrow(P',P'+Q)) >_{\{QMC\}}\} \\
&\quad -\frac{1}{2}\{< (G_\uparrow(P+Q,P)+ \; G_\downarrow(P+Q,P)) >_{\{QMC\}}) \\
&\qquad < (G_\uparrow(P',P'+Q)+G_\downarrow(P',P'+Q)) >_{\{QMC\}}\}\Big] \quad \text{(C.24)}
\end{aligned}
$$

In the QMC measurement, this quantity is represented by gamatc(i,j,l)=chi_d(Q)_P,P'.

$\chi_{m^0}^{ph}$:

$$
\begin{aligned}
\chi_{m^0}^{ph}(Q)_{P,P'} &= \chi_{\uparrow\uparrow;\uparrow\uparrow}^{ph}(Q)_{P,P'} - \chi_{\uparrow\uparrow;\downarrow\downarrow}^{pp}(Q)_{P,P'} \\
&= \frac{1}{N_c\beta}\Big[-\frac{1}{2}\{< G_\uparrow(P',P)G_\uparrow(P+Q,P'+Q) >_{\{QMC\}} \\
&\quad + \; < G_\downarrow(P',P)G_\downarrow(P+Q,P'+Q) >_{\{QMC\}}\} \\
&\quad +\frac{1}{2}\{< (G_\uparrow(P+Q,P) - \; G_\downarrow(P+Q,P)) \\
&\qquad (G_\uparrow(P',P'+Q) - G_\downarrow(P',P'+Q)) >_{\{QMC\}}\}\Big] \quad \text{(C.25)}
\end{aligned}
$$

In the QMC measurement, this quantity is represented by gamat(i,j,l)=2*chi_m(Q)_P,P'.

C.3.2 Bethe-Salpeter Equations

χ_d^{ph}:

$$\begin{aligned}
\chi_d^{ph}(Q)_{P,P'} &= -N_c\beta * G(P)G(P+Q)\delta_{P,P'} \\
&\quad - G(P+Q)G(P)F_d(Q)_{P,P'}G(P'+Q)G(P')
\end{aligned} \tag{C.26}$$

The situation of determining the sign for the second term is exactly the same as that for $\chi_P(Q)_{P,P'}$. So it should be a minus sign.

$\chi_{m^0}^{ph}$:

$$\begin{aligned}
\chi_{m^0}^{ph}(Q)_{P,P'} &= -N_c\beta * G(P)G(P+Q)\delta_{P,P'} \\
&\quad - G(P+Q)G(P)F_{m^0}(Q)_{P,P'}G(P'+Q)G(P')
\end{aligned} \tag{C.27}$$

The minus sign for the second term is due to the first order contribution of U

$$\chi_{m^0}^{p}(Q)_{P,P'}^{(2)} = UG(P+Q)G(P'+Q)G(-P)G(-P') \tag{C.28}$$

and that F_{m^0} approaches to $-U$ for the large frequency limit.

The un-perturbed two-particle Green's function for the p-h channel can be defined as:

$$\chi_0^{ph}(Q)_{P,P'} \equiv -N_c\beta * G(P)G(P+Q)\delta_{P,P'} \equiv -N_c\beta * \chi_0^{ph}(Q)_P\delta_{P,P'} \tag{C.29}$$

So

$$\Gamma_{d/m}(Q)_{P,P'} = -(N_c\beta)^2(\chi_0^{ph}(Q)^{-1} - \chi_{d/m}(Q)^{-1})_{P,P'} \tag{C.30}$$

and similarly,

$$F_{d/m}(Q)_{P,P'} = - \chi_0^{ph}(Q)_P^{-1}(\chi_{d/m}(Q) - \chi_0^{ph}(Q))_{P,P'}\chi_0^{ph}(Q)_{P'}^{-1} \tag{C.31}$$

Appendix D

High-Frequency Expansion of Two-Particle Quantities

Both the vertex functions and the two-particle Green functions are represented by 3-D arrays, which are imposing a great challenge in either the memory requirement or computational complexity. On the other hand, there is a huge redundancy in the information contained in these 3-D arrays, especially in the high-frequency sector. This property can be used to greatly reduce the computational and memory requirement for any calculation at the two-particle level. In the following, we will show how to derive a complete form for the high-frequency expansion of those two-particle quantities, by closely analyzing the parquet equation and Bethe-Salpeter equation, and doing the Taylor expansion on the Coulomb interaction. And we will also present some numerical results, showing that the high-frequency information is captured very well by the high-frequency expansion up to second-order in U.

D.1   Analytical Results

Vertex Ladders

Let us consider the particle-particle channel first. The vertex ladder is defined as

$$\Phi^p(Q)_{P,P'} \equiv \frac{1}{N_c\beta} \sum_{P''} \Gamma^p(Q)_{P,P''} \chi_0^{pp}(Q)_{P''} F^p(Q)_{P'',P'} \tag{D.1}$$

where the un-perturbed two-particle Green function is defined as

$$\chi_0^{pp}(Q)_P \equiv -G(P+Q)G(-P) \tag{D.2}$$

From Eq. C.15 and Eq. C.16, we have

$$G(P+Q)G(-P)F^p(Q)_{P,P'} = \frac{1}{N_c\beta} \sum_{P''} \chi^p(Q)_{P,P''} \Gamma^p(Q)_{P'',P'} \tag{D.3}$$

Then we have

$$\Phi_p(Q)_{P,P'} = -\frac{1}{(N_c\beta)^2}\sum_{P''}\Gamma_p(Q)_{P,P''}\chi_p(Q)_{P'',P'''}\Gamma_p(Q)_{P''',P'} \tag{D.4}$$

$$= -\frac{1}{(N_c\beta)^2}\sum_{P'',P'''}U\chi_p(Q)_{P'',P'''}U + \mathcal{O}(U^3) \tag{D.5}$$

$$= -U^2\chi_p(Q) + \mathcal{O}(U^3) \tag{D.6}$$

in which we have used the particle-particle polarization function

$$\chi_p(Q) \equiv \frac{1}{(N_c\beta)^2}\sum_{P,P'}\chi_p(Q)_{P,P'} \tag{D.7}$$

Similarly, for the particle-hole channel, we have

$$\Phi_{d/m}(Q)_{P,P'} = -U^2\chi_{d/m}(Q) + \mathcal{O}(U^3) \tag{D.8}$$

and

$$\chi_{d/m}(Q) \equiv \frac{1}{(N_c\beta)^2}\sum_{P,P'}\chi_{d/m}(Q)_{P,P'} \tag{D.9}$$

$$\chi_0^{ph}(Q)_P \equiv G(P+Q)G(P) \tag{D.10}$$

In the high-frequency limit, we have

$$\Phi_p^\infty(Q)_{P,P'} = -U^2\chi_p(Q) \tag{D.11}$$

and

$$\Phi_{d/m}^\infty(Q)_{P,P'} = -U^2\chi_{d/m}(Q) \tag{D.12}$$

Note that in this limit, the two fermionic indices P and P' are not relevant.

Vertex Functions

Now we can start to derive the expression of the high-frequency expansion for the vertex functions. Parquet equations read

$$\Gamma_d(Q)_{PP'} = \Lambda_d(Q)_{PP'} - \frac{1}{2}\Phi_d(P'-P)_{P,P+Q} - \frac{3}{2}\Phi_m(P'-P)_{P,P+Q}$$
$$+ 2\Psi(P+P'+Q)_{-P-Q,-P} - \Psi(P+P'+Q)_{-P',-P} \tag{D.13}$$

$$\Gamma_m(Q)_{PP'} = \Lambda_m(Q)_{PP'} - \frac{1}{2}\Phi_d(P'-P)_{P,P+Q} + \frac{1}{2}\Phi_m(P'-P)_{P,P+Q}$$
$$- \Psi(P+P'+Q)_{-P',-P} \qquad (D.14)$$

$$\Gamma_p(Q)_{PP'} = \Lambda_p(Q)_{PP'} + \frac{1}{2}\Phi_d(P'-P)_{-P',P+Q} - \frac{1}{2}\Phi_m(P'-P)_{-P',P+Q}$$
$$-\Phi_m(P+P'+Q)_{-P',-P} \qquad (D.15)$$

Inserting the asymptotic expression of the vertex ladders derived from the above, we have for the p-p channel

$$\Gamma_p^\infty(Q)_{PP'} = U - \frac{1}{2}\chi_d(P'-P)U^2 + \frac{1}{2}\chi_m(P'-P)U^2 + \chi_m(P+P'+Q)U^2 \qquad (D.16)$$

And since

$$F_p(Q)_{P,P'} = \Gamma_p(Q)_{P,P'} + \Psi(Q)_{P,P'} \qquad (D.17)$$

we have

$$F_p^\infty(Q)_{PP'} = \Gamma_p^\infty(Q)_{PP'} - \chi_p(Q)U^2 \qquad (D.18)$$
$$= U - \chi_p(Q)U^2 - \frac{1}{2}\chi_d(P'-P)U^2 + \frac{1}{2}\chi_m(P'-P)U^2 + \chi_m(P+P'+Q)U^2$$

Similarly for particle-hole channel

$$F_d^\infty(Q)_{PP'} = \Gamma_d^\infty(Q)_{PP'} - \chi_d(Q)U^2 \qquad (D.19)$$
$$= U - \chi_d(Q)U^2 + \frac{1}{2}\chi_d(P'-P)U^2 + \frac{3}{2}\chi_m(P'-P)U^2 - \chi_p(P+P'+Q)U^2$$

$$F_m^\infty(Q)_{PP'} = \Gamma_m^\infty(Q)_{PP'} - \chi_m(Q)U^2 \qquad (D.20)$$
$$= -U - \chi_m(Q)U^2 + \frac{1}{2}\chi_d(P'-P)U^2 - \frac{1}{2}\chi_m(P'-P)U^2 + \chi_p(P+P'+Q)U^2$$

Two-Particle Green Functions

We can derive similar high-frequency expansion for the 2-p Green's functions by using the two-particle Dyson equations

$$\chi_p(Q)_{PP'} = -\chi_{pp}^0(Q)_P\delta_{P,P'} - T * \chi_{pp}^0(Q)_P F_p(Q)_{PP'}\chi_{pp}^0(Q)_{P'} \qquad (D.21)$$

$$\chi_{d/m}(Q)_{PP'} = -\chi_{ph}^0(Q)_P\delta_{P,P'} - T * \chi_{ph}^0(Q)_P F_{d/m}(Q)_{PP'}\chi_{ph}^0(Q)_{P'} \tag{D.22}$$

Therefore

$$\chi_p^\infty(Q)_{PP'} = -\chi_{pp}^0(Q)_P\delta_{P,P'} - T * \chi_{pp}^0(Q)_P F_p^\infty(Q)_{PP'}\chi_{pp}^0(Q)_{P'} \tag{D.23}$$

$$\chi_{d/m}^\infty(Q)_{PP'} = -\chi_{ph}^0(Q)_P\delta_{P,P'} - T * \chi_{ph}^0(Q)_P F_{d/m}^\infty(Q)_{PP'}\chi_{ph}^0(Q)_{P'} \tag{D.24}$$

Hubbard Atom

The hamiltonian for Hubbard atom at half-filling is:

$$H = -\frac{U}{2}(n_\uparrow + n_\downarrow) + U n_\uparrow n_\downarrow \tag{D.25}$$

For this toy model, the susceptibilities are

$$\chi_p(i\nu) = \frac{\beta}{Z}\delta_{i\nu,0} \equiv \chi_p\delta_{i\nu,0} \tag{D.26}$$

$$\chi_d(i\nu) = \frac{\beta}{Z}\delta_{i\nu,0} \equiv \chi_d\delta_{i\nu,0} \tag{D.27}$$

$$\chi_m(i\nu) = \beta(\frac{1}{2} - \frac{1}{Z})\delta_{i\nu,0} \equiv \chi_m\delta_{i\nu,0} \tag{D.28}$$

in the above, Z is the partition function

$$Z = 2(e^{\beta U/2} + 1) \tag{D.29}$$

Therefore, we have

$$F_p^\infty(i\nu)_{i\omega_n i\omega_{n'}} = U - \chi_p U^2\delta_{i\nu,0} - \frac{1}{2}\chi_d U^2\delta_{i\omega_n i\omega_{n'}} + \frac{1}{2}\chi_m U^2\delta_{i\omega_n i\omega_{n'}} + \chi_m U^2\delta_{i\omega_n + i\omega_{n'} + i\nu,0} \tag{D.30}$$

$$F_d^\infty(i\nu)_{i\omega_n i\omega_{n'}} = U - \chi_d U^2\delta_{i\nu,0} + \frac{1}{2}\chi_d U^2\delta_{i\omega_n i\omega_{n'}} + \frac{3}{2}\chi_m U^2\delta_{i\omega_n i\omega_{n'}} - \chi_p U^2\delta_{i\omega_n + i\omega_{n'} + i\nu,0} \tag{D.31}$$

$$F_m^\infty(i\nu)_{i\omega_n i\omega_{n'}} = -U - \chi_m U^2\delta_{i\nu,0} + \frac{1}{2}\chi_d U^2\delta_{i\omega_n i\omega_{n'}} - \frac{1}{2}\chi_m U^2\delta_{i\omega_n i\omega_{n'}} + \chi_p U^2\delta_{i\omega_n + i\omega_{n'} + i\nu,0} \tag{D.32}$$

D.2 Numerical Results of the High-Frequency Expansion

In the following, we will show numerical results for the Hubbard atom system from the above exact result compared with the high-frequency expansion result. The parameters used are: $U = 0.73$, $T = 0.3333$, $\langle n \rangle = 1$, $i\nu = 0$, and we only look into the charge channel.

Results for Feducible and Irreducible Vertex Functions

- One of the fermionic frequencies is set to be $\omega_{n'} = 21\pi T$, which is in the high-frequency sector. See Fig. D.1.
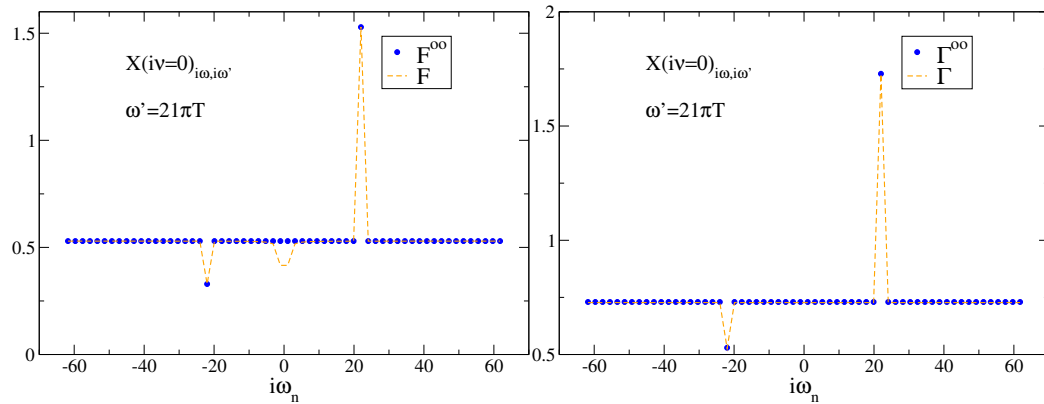
Figure D.1: (Color online) Comparison of the numerical result and the high-frequency expansion result for the reducible vertex (left) and the irreducible vertex (right).

- Diagonal part. See Fig. D.2.

- Anti-diagonal part. See Fig. D.3.

Results for the Two-Particle Green Function

See Fig. D.4.
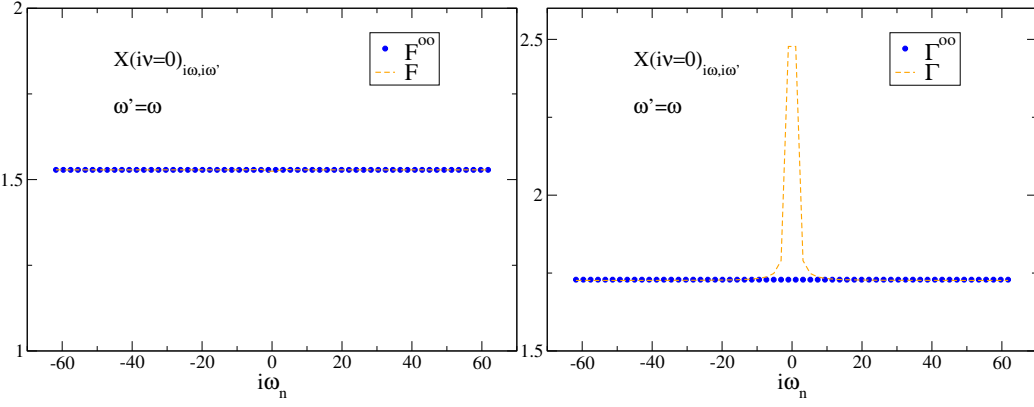
Figure D.2: (Color online) Comparison of the numerical result and the high-frequency expansion result for the reducible vertex (left) and the irreducible vertex (right) for the diagonal part.
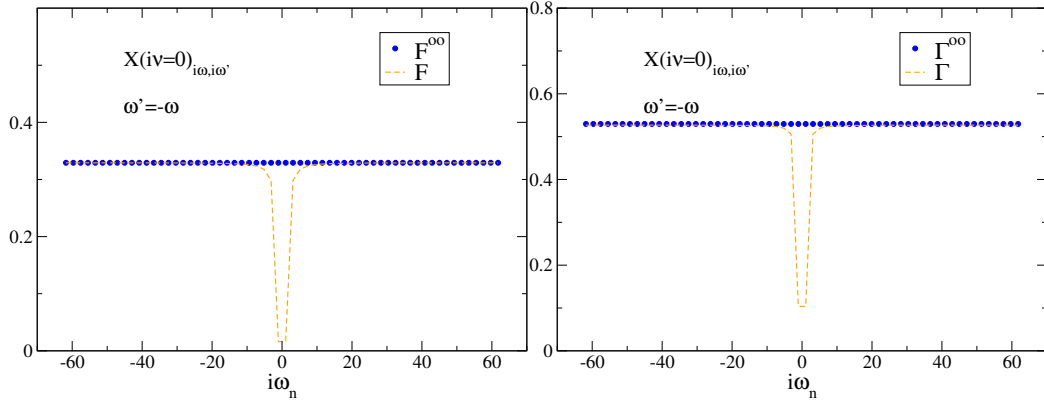

Figure D.3: (Color online) Comparison of the numerical result and the high-frequency expansion result for the reducible vertex (left) and the irreducible vertex (right) for the anti-diagonal part.
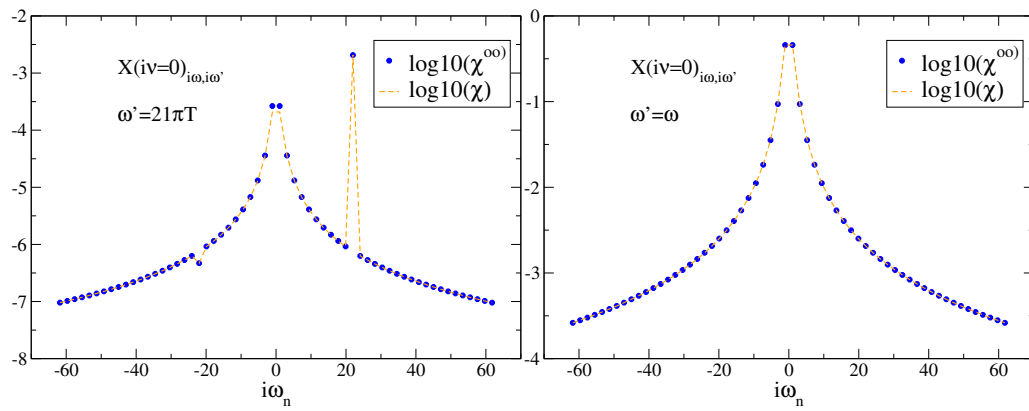
Figure D.4: (Color online) Comparison of the numerical result and the high-frequency expansion result for the two-particle Green function.

Appendix E

Parquet Approximation for Anharmonical Classical Oscillator System

In this chapter, we will show how the parquet formalism can be developed for the anharmonical classical oscillator system. A hierarchy of approximate methods can then be designed and numerical results are shown, which exemplifies that the lower level the approximation is made on, the better result would yield by comparing with the exact result.

E.1   Parquet Formalism

Starting from the hamiltonian for the anharmonical classical oscillator system, one can form the functional representatin of the system. From the latter, one has the bare Green function and bare interaction, which are all the input needed for any conventional digrammatic perturbation theory. And thus one can develop the parquet formalism and design the hierarchy of different approximate methods. Especially for this system, we have a analytical form for the solution of the parquet equation and Bethe-Salpeter equation.

Hamiltonian and Generating Functional

The Hamiltonian for the classical anharmonic oscillator is

$$H = \frac{p^2}{2m} + \frac{1}{2}m\omega_0^2 x^2 + ux^4 \tag{E.1}$$

Its partition function is

$$\frac{Z_c}{Z_{c,0}} = \frac{1}{Z_{c,0}} \int_{-\infty}^{\infty} dp \int_{-\infty}^{\infty} dx e^{-\beta H} = \frac{1}{\sqrt{2\pi G^0}} \int_{-\infty}^{\infty} d\psi e^{-\frac{\psi^2}{2G^0}} e^{-\frac{g}{4!}\psi^4} \tag{E.2}$$

where $G^0 = 1/(\beta m \omega_0^2)$, $\beta u = g/4!$ and $\psi \equiv x$. Note that this is a classical system, therefore, there is no dynamical information. Both the Green function and the self-energy are thus scalars instead of functions of frequencies.

Feynman's Rule for the Self-Energy

The Feynman's rule is essentially the same as the one for the Bosonic system. The only difference is that the function in the quantum case is reduced to a single number (in this sense, the generating funcional is actually a generating function).

1. Each bare Green function G^0 is represented by a single solid line

2. The bare interaction is denoted by a cross

3. Draw all topologically different and linked diagrams using the solid line and cross

4. When evaluating the contribution of each diagram, one will have the following result

$$\Sigma = \alpha \frac{1}{n!} \left(\frac{-g}{4!}\right)^n G^{2n-1} \tag{E.3}$$

in which n is the order of perturbation, α the symmetry factor and G can be the bare Green function or the mean-field dressed one. As for the symmetry factor, there are some examples in the following section.
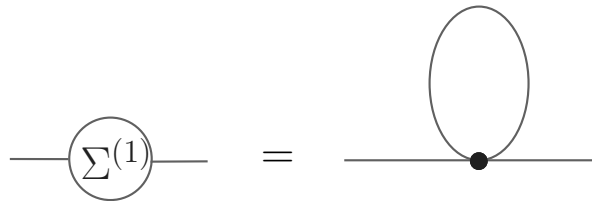
One-Particle Quantities

- Dyson equation

$$G = \frac{1}{G_0^{-1} - \Sigma} \tag{E.4}$$

- first-order (Hartree) contribution to the self-energy

$$\Sigma^{(1)} = -\frac{g}{2} G \tag{E.5}$$

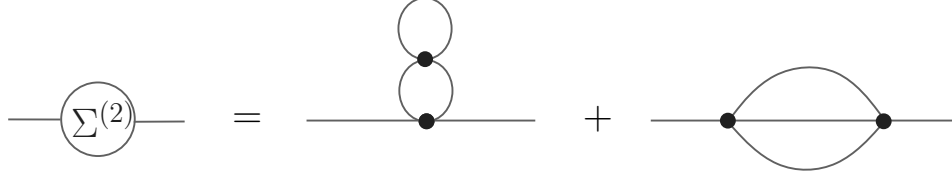For this case, the symmetry factor is estimated as

$$\alpha = C_4^2 = \frac{4!}{2} \tag{E.6}$$

- 2nd-order contribution to the self-energy

$$\Sigma^{(2)} = \frac{1}{4}g^2 G^3 + \frac{1}{6}g^2 G^3 = \frac{5}{12}g^2 G^3 \tag{E.7}$$

The symmetry factor for the first term is

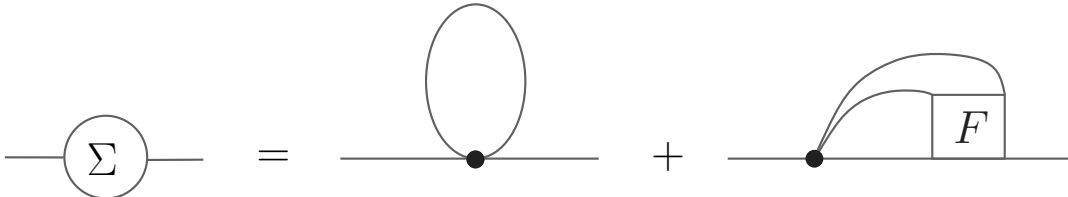$$\alpha_1 = C_2^2 C_4^2 C_4^2 = \frac{2!(4!)^2}{4} \tag{E.8}$$

and the second term

$$\alpha_2 = C_2^2 C_4^1 C_4^3 = \frac{2!(4!)^2}{6} \tag{E.9}$$

Note that the first one is non-skeleton type of diagram. Thus it shouldn't be included in the Mean-Field calculation of the self-energy. Instead we should use the second one only

$$\Sigma^{(2)} = \frac{1}{6}g^2 G^3 \tag{E.10}$$

Schwinger-Dyson Equation

$$\Sigma = -\frac{g}{2}G - \frac{1}{6}gFG^3 \tag{E.11}$$

Note that the 2nd-order self-energy is recovered if one replaces the reducible F by the bare interaction g.

Bethe-Salpeter Equations

- Horizontal channel

$$F = \Gamma^h + F\chi_0\Gamma^h \tag{E.12}$$

$$\boxed{F} = \boxed{\Gamma^h} + \boxed{\Gamma^h}\,\boxed{\chi_0}\,\boxed{F}$$

- Vertical channel

$$F = \Gamma^v + F\chi_0\Gamma^v \tag{E.13}$$

$$\boxed{F} = \boxed{\Gamma^v} + \begin{array}{c}\boxed{\Gamma^v}\\ \boxed{\chi_0}\\ \boxed{F}\end{array}$$

- Crossed channel

$$F = \Gamma^c + F\chi_0\Gamma^c \tag{E.14}$$

$$\boxed{F} = \boxed{\Gamma^c} + \begin{array}{c}\boxed{\Gamma^c}\\ \boxed{\chi_0}\\ \boxed{F}\end{array}$$

From the above three Bethe-Salpeter equations, we have

$$\Gamma = \Gamma^h = \Gamma^v = \Gamma^c = \frac{F}{1 + F\chi_0} \tag{E.15}$$

in which the non-perturbed susceptibility χ_0 is defined as

$$\chi_0 \equiv \frac{1}{2}GG \tag{E.16}$$

the one-half factor is needed to avoid the double-counting.

87

Parquet Equations

- Horizontal channel

$$\Gamma^h = \Lambda + F\chi_0\Gamma^v + F\chi_0\Gamma^c \tag{E.17}$$

- Vertical channel

$$\Gamma^v = \Lambda + F\chi_0\Gamma^h + F\chi_0\Gamma^c \tag{E.18}$$

- crossed channel

$$\Gamma^c = \Lambda + F\chi_0\Gamma^h + F\chi_0\Gamma^v \tag{E.19}$$

Because of the result(E.15) from the Bethe-Salpeter equations, the three Parquet equations are reducible to one

$$\Gamma = \Lambda + 2F\chi_0\Gamma \tag{E.20}$$

Inserting result(E.15), then we end up with the following equaiton

$$2\chi_0\Lambda F^2 + (\chi_0\Lambda - 1)F + \Lambda = 0 \tag{E.21}$$

whose solution is

$$F = \frac{(1 - \chi_0\Lambda) - \sqrt{(\chi_0\Lambda - 1)^2 - 8\chi_0\Lambda}}{4\chi_0} \tag{E.22}$$

Note that another solution is ruled out since $F \to -\Lambda$ for small g.

Parquet Approximation

We have a closed formalism (Eq (E.4), (E.11) and (E.22)) to determine the Green function if given addtionally the information of fully irreducible vertex Λ. The simplest approximation on Λ is just letting it approximated by the bare interation $-g$, then we have the Parquet approximation equations

$$G = \frac{1}{G_0^{-1} - \Sigma} \tag{E.23}$$

$$\Sigma = -\frac{g}{2}G - \frac{1}{6}gFG^3 \tag{E.24}$$

$$F = \frac{(1 - g\chi_0) - \sqrt{(g\chi_0 - 1)^2 - 8g\chi_0}}{4\chi_0} \tag{E.25}$$

in which the non-perturbed susceptibility χ_0 is defined as

$$\chi_0 \equiv \frac{1}{2}GG \tag{E.26}$$

and G_0 is chosen to be one in the calculation.

E.2 Numerical Results

After self-consistently iterating the above equations, one can get almost exact result for the self-energy (See Fig. E.1). In addition to the good result for the parquet approximation, it's interesting to observe that the Hartree method always converges and produces quite good result, while the higher-order methods (2nd-order, self-consistent 2nd-order and fluctuation exchange (FLEX)) diverge at some critical g.
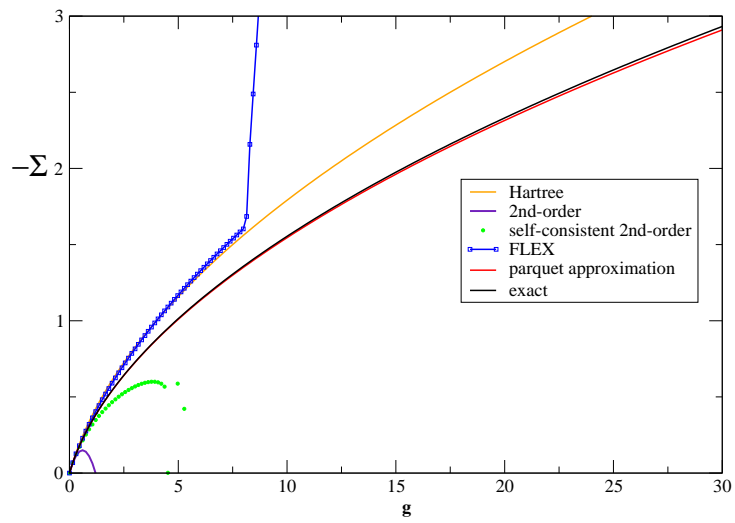
Figure E.1: (color online) Results from different methods. From 2nd-order approximation, FLEX, to parquet approximation, the results become better and closer to the exacct result.

Appendix F

Crossing-Symmetric Parquet Formalism

Our numerical experiments on the parquet approximation show that the instability problem encountered in the parquet calcualtion is partially due to the violation of the crossing symmetries, which are the consequence of the Pauli exclusion principle. How to preserve the crossing symmetries thus becomes an essential point in stablizing the parquet calculation. In the following, we will show how these crossing symmetries can be encoded in the parquet formalism, forming so-named crossing-symmetric parquet formalism. With the crossing symmetries built in, the parquet calculation would become much more stable, and both the number of independent variables and the number of equations can also be reduced.

F.1 Two-Particle Quantities

Vertex Functions

The full vertex F and the fully irreducible Λ have all the crossing symmetries, and thus only one out of four of them (density, magnetic, particle-particle singlet and triplet channels) is truly independent. The irreducible vertex Γ only has the crossing symmetries within the particle-particle channel, so that we need three channels to describe these vertices.

- Particle-Particle Channel

For the particle-particle channel, we only need the vertex function defined in the following:

$$X(Q)_{P,P'} \quad \equiv \quad$$

$$X(Q)_{P,P'} \equiv X^{pp}_{\uparrow\downarrow;\uparrow\downarrow}(P + Q, -P; P' + Q, -P'). \tag{F.1}$$

Due to the crossing symmetry, the other component can be written down as

$$X^{pp}_{\uparrow\downarrow;\downarrow\uparrow}(P + Q, -P; P' + Q, -P') = -X^{pp}_{\uparrow\downarrow;\uparrow\downarrow}(P + Q, -P; -P', P' + Q) = -X(Q)_{P,-P'-Q}. \tag{F.2}$$

We can thus construct the singlet and triplet vertices according to the following definition:

$$X_{s/t} = X^{pp}_{\uparrow\downarrow;\uparrow\downarrow} \mp X^{pp}_{\uparrow\downarrow;\downarrow\uparrow}, \tag{F.3}$$

so that

$$X_{s/t} = X(Q)_{P,P'} \pm X(Q)_{P,-P'-Q}. \tag{F.4}$$

- Particle-Hole Channel

For the particle-hole channel, we can express the two components in terms of $X(Q)_{P,P'}$ (for F and Λ only) as

$$\begin{aligned} X^{ph}_{\uparrow\uparrow;\uparrow\uparrow}(P + Q, P; P' + Q, P') &= -X^{pp}_{\uparrow\uparrow;\uparrow\uparrow}(P + Q, P'; P' + Q, P) \\ &= -X_t(P + P' + Q)_{-P',-P} \\ &= -X(P + P' + Q)_{-P',-P} + X(P + P' + Q)_{-P',-P'-Q} \end{aligned} \tag{F.5}$$

and

$$X^{ph}_{\uparrow\uparrow;\downarrow\downarrow}(P+Q,P;P'+Q,P') \;=\; -X^{ph}_{\uparrow\downarrow;\uparrow\downarrow}(P+Q,P'+Q;P,P')$$
$$=\; X^{pp}_{\uparrow\downarrow;\uparrow\downarrow}(P+Q,P';P,P'+Q)$$
$$=\; X(P+P'+Q)_{-P',-P'-Q}. \tag{F.6}$$

Since the definition for the density and magnetic vertices is

$$X_{d/m} = X^{ph}_{\uparrow\uparrow;\uparrow\uparrow} \pm X^{ph}_{\uparrow\uparrow;\downarrow\downarrow}, \tag{F.7}$$

we have

$$X_d = 2X(P+P'+Q)_{-P',-P'-Q} - X(P+P'+Q)_{-P',-P} \tag{F.8}$$

$$X_m = -X(P+P'+Q)_{-P',-P}. \tag{F.9}$$

Two-Particle Green Functions

From the Bethe-Salper equations, we can easily derive the expressions for the two-particle Green functions as

$$\chi(Q)_{P,P'} \equiv \chi^{pp}_{\uparrow\downarrow;\uparrow\downarrow}(P+Q,-P;P'+Q,-P') \tag{F.10}$$

$$\chi_{s/t}(Q)_{P,P'} = \chi(Q)_{P,P'} \pm \chi(Q)_{P,-P'-Q} \tag{F.11}$$

$$\chi_d(Q)_{P,P'} = 2\chi(P+P'+Q)_{-P',-P'-Q} - \chi(P+P'+Q)_{-P',-P} - 2G(P)G(P')\delta_{Q,0} \tag{F.12}$$

$$\chi_m(Q)_{P,P'} = -\chi(P+P'+Q)_{-P',-P}. \tag{F.13}$$

Note that for the density channel, the vacuum term should be subtracted explicitly.

F.2 Two-Particle Equations

parquet equations

Now that we have expressed the vertices in terms of only the p-p channel vertex, next we will re-write the parquet equations.

In the parquet equations, we need to rotate the vertices according to the following four different rotation patterns:

- rotation 1:

$$F_d(P' - P)_{P,P+Q} = 2F(P + P' + Q)_{-P-Q,-P'-Q} - F(P + P' + Q)_{-P-Q,-P}$$
$$= 2F(P + P' + Q)_{-P',-P} - F(P + P' + Q)_{-P-Q,-P} \qquad (F.14)$$

$$F_m(P' - P)_{P,P+Q} = -F(P + P' + Q)_{-P-Q,-P} \qquad (F.15)$$

- rotation 2:

$$F_s(P + P' + Q)_{-P-Q,-P} = F(P + P' + Q)_{-P-Q,-P} + F(P + P' + Q)_{-P-Q,-P'-Q}$$
$$= F(P + P' + Q)_{-P-Q,-P} + F(P + P' + Q)_{-P',-P} \qquad (F.16)$$

$$F_t(P + P' + Q)_{-P-Q,-P} = F(P + P' + Q)_{-P-Q,-P} - F(P + P' + Q)_{-P-Q,-P'-Q}$$
$$= F(P + P' + Q)_{-P-Q,-P} - F(P + P' + Q)_{-P',-P} \qquad (F.17)$$

- rotation 3:

$$F_d(P' - P)_{-P',P+Q} = 2F(Q)_{-P-Q,-P'-Q} - F(Q)_{-P-Q,P'}$$
$$= 2F(Q)_{P,P'} - F(Q)_{-P-Q,P'} \qquad (F.18)$$

$$F_m(P' - P)_{-P',P+Q} = -F(Q)_{-P-Q,P'} \qquad (F.19)$$

- rotation 4:

$$F_d(P + P' + Q)_{-P',-P} = 2F(Q)_{P,-P'-Q} - F(Q)_{P,P'} \qquad (F.20)$$

$$F_m(P + P' + Q)_{-P',-P} = -F(Q)_{P,P'} \qquad (F.21)$$

Therefore, we can re-write the parquet equations as:

parquet equation 1:

$$\Gamma_d(Q)_{PP'} = \Lambda_d(Q)_{PP'} - \frac{1}{2}\Phi_d(P' - P)_{P,P+Q} - \frac{3}{2}\Phi_m(P' - P)_{P,P+Q}$$
$$+ \frac{1}{2}\Psi_s(P + P' + Q)_{-P-Q,-P} + \frac{3}{2}\Psi_t(P + P' + Q)_{-P-Q,-P}$$
$$= \Lambda_d(Q)_{PP'} + 4F(P + P' + Q)_{-P-Q,-P} - 2F(P + P' + Q)_{-P',-P}$$
$$+ \frac{1}{2}\Gamma_d(P' - P)_{P,P+Q} + \frac{3}{2}\Gamma_m(P' - P)_{P,P+Q}$$
$$- 2\,\Gamma(P + P' + Q)_{-P-Q,-P} + \Gamma(P + P' + Q)_{-P',-P} \qquad (F.22)$$

parquet equation 2:

$$
\begin{aligned}
\Gamma_m(Q)_{PP'} &= \Lambda_m(Q)_{PP'} - \frac{1}{2}\Phi_d(P'-P)_{P,P+Q} + \frac{1}{2}\Phi_m(P'-P)_{P,P+Q} \\
&\quad - \frac{1}{2}\Psi_s(P+P'+Q)_{-P-Q,-P} + \frac{1}{2}\Psi_t(P+P'+Q)_{-P-Q,-P} \\
&= \Lambda_m(Q)_{PP'} - 2F(P+P'+Q)_{-P',-P} \\
&\quad + \frac{1}{2}\Gamma_d(P'-P)_{P,P+Q} - \frac{1}{2}\Gamma_m(P'-P)_{P,P+Q} \\
&\quad + \Gamma(P+P'+Q)_{-P',-P}
\end{aligned}
\tag{F.23}
$$

parquet equation 3&4:

$$
\begin{aligned}
\Gamma(Q)_{PP'} &= \Lambda(Q)_{PP'} + \frac{1}{2}\Phi_d(P'-P)_{-P',P+Q} - \frac{1}{2}\Phi_m(P'-P)_{-P',P+Q} \\
&\quad - \Phi_m(P+P'+Q)_{-P',-P} \\
&= \Lambda(Q)_{PP'} + 2F(Q)_{P,P'} \\
&\quad - \frac{1}{2}\Gamma_d(P'-P)_{-P',P+Q} + \frac{1}{2}\Gamma_m(P'-P)_{-P',P+Q} \\
&\quad + \Gamma_m(P+P'+Q)_{-P',-P}
\end{aligned}
\tag{F.24}
$$

Parquet equations + Bethe-Salpeter equations

To summarize, we have

$$
\begin{aligned}
\Gamma_d(Q)_{PP'} &= 2\Lambda(P+P'+Q)_{-P',-P'-Q} - \Lambda(P+P'+Q)_{-P',-P} \\
&\quad + 4F(P+P'+Q)_{-P-Q,-P} - 2F(P+P'+Q)_{-P',-P} \\
&\quad + \frac{1}{2}\Gamma_d(P'-P)_{P,P+Q} + \frac{3}{2}\Gamma_m(P'-P)_{P,P+Q} \\
&\quad - 2\,\Gamma(P+P'+Q)_{-P-Q,-P} + \Gamma(P+P'+Q)_{-P',-P}
\end{aligned}
\tag{F.25}
$$

$$
\begin{aligned}
\Gamma_m(Q)_{PP'} &= -\Lambda(P+P'+Q)_{-P',-P} - 2F(P+P'+Q)_{-P',-P} \\
&\quad + \frac{1}{2}\Gamma_d(P'-P)_{P,P+Q} - \frac{1}{2}\Gamma_m(P'-P)_{P,P+Q} \\
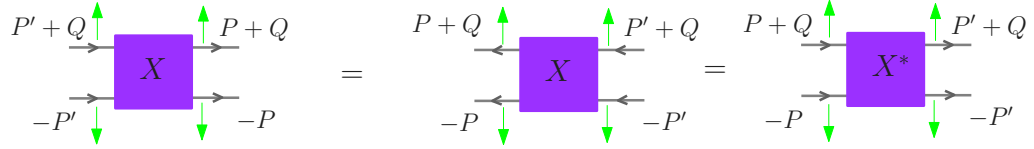&\quad + \Gamma(P+P'+Q)_{-P',-P}
\end{aligned}
\tag{F.26}
$$

$$
\begin{aligned}
\Gamma(Q)_{PP'} &= \Lambda(Q)_{PP'} + 2F(Q)_{P,P'} \\
&\quad - \frac{1}{2}\Gamma_d(P'-P)_{-P',P+Q} + \frac{1}{2}\Gamma_m(P'-P)_{-P',P+Q} \\
&\quad + \Gamma_m(P+P'+Q)_{-P',-P}
\end{aligned}
\tag{F.27}
$$

$$F = \Gamma + \Gamma\chi_0^{pp}F \tag{F.28}$$

$$F_{d/m} = \Gamma_{d/m} + \Gamma_{d/m}\chi_0^{ph}F_{d/m} \tag{F.29}$$

F.3   Other Symmetries

There are extra symmetries associated with the vertex functions. The first one is the graphic symmetry. For particle-particle vertex $X(Q)_{P,P'}$, we can rotate it by an angle of π around the vertical axis without changing its value. Thus we have

$$X(Q)_{P,P'} = X(-Q)_{-P',-P} = X^*(Q)_{P',P} \tag{F.30}$$

With this symmetry (the first identity), we can store vertex functions with positive external momenta and frequencies, and the other half of the information is implied. The second identity is a manifestation of the inversion symmetry, which can be used to further reduce the size of vertex functions.

As another graphic symmetry, we can rotate the vertex graph around the horizontal axis, such that
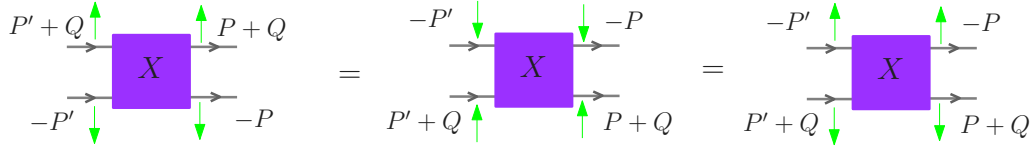
$$X(Q)_{P,P'} = X_{\downarrow\uparrow;\downarrow\uparrow}(Q)_{-P-Q,-P'-Q} = X(Q)_{-P-Q,-P'-Q} \tag{F.31}$$

The second identify is from the rotation invariance in spin space. The special case is for $Q = 0$, then we have

$$X(Q = 0)_{P,P'} = X(Q = 0)_{-P,-P'} = X^*(Q = 0)_{P,P'} \tag{F.32}$$

So $X(Q = 0)_{P,P'}$ is real.

Appendix G

Determination of the Phase Digram for the 2-D Hubbard Model

Around the phase transitions, most of the interesting physics happens. The paramters at which these phase transitions happen define the boundaries of different phases in the phase diagrams of a given material. In nature, almost all of the phase transitions are either the first-order or the second-order. For the cuprate materials, we are most interested in the second-order transitions, such as the anti-ferromagneticphase transition or the d-wave superconducting phase transition. In the following, we will discuss how to determin a second-order phase transition numerically, and then show how to get a phase diagram for the 2-D Hubbard model.

G.1 Pairing Matrix Formalism

There are two ways to detect a second-order phase transition. One can explicitly introduce the symmetry breaking fields and thus define the order parameter. The temperature where the order parameter begin to vanish is the phase transition temperater. Equivalently, one can start from a symmetric system and look into the susecptibility of perturbed field. The divergence of suscepbiltiy would also tell the happening of phase transition, just as shown in Fig. G.1.

Note that the susceptibility can be expressed as

$$\chi(T) = \frac{\chi_0}{1 - \Gamma \chi_0} \tag{G.1}$$

Obviously, the singularity is caused by the zeros in the dominator. This happens when the LEV of the so-called paring matrix, which is constructed by the irreducible vertex and the bare susceptibility as

$$M \equiv \Gamma \chi_0 \tag{G.2}$$

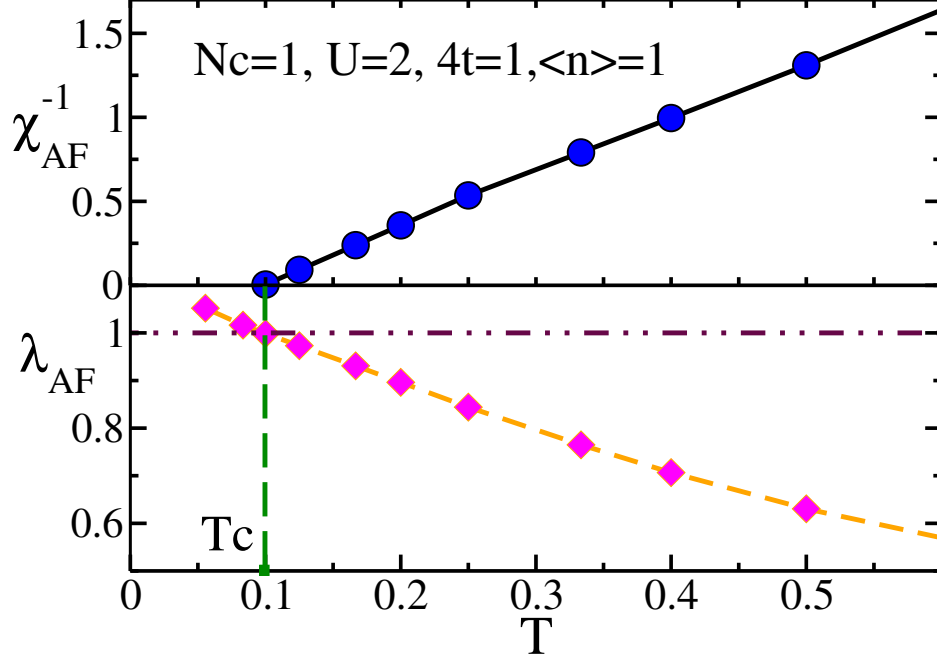goes across the unity. Namely, at the transition temperature, we have $\lambda \to 1$ in the eigen-equation

Figure G.1: (color online) Temperature dependence of the inversed anti-ferromagnetic susceptibility and the leading eigen value of the paring matrix. Note that at the transition temperature, the susceptibility diverges and the leading eigen values crosses unity.

$$\Gamma \chi_0 \phi = \lambda \phi \qquad (G.3)$$

As shown in Fig. G.1, the LEV going across unity at the same temperature where the susceptibility diverges for the anti-ferromagnetic channel. Therefore, monitoring the change of λ by changing other control parameters, such as temperature, provides anther way to detect whether the system goes through a transition.

G.2 Determination of Phase diagram of the 2-D Hubbard Model

In the following section, we will show to determine the phase diagram for the 2-D Hubbard model.
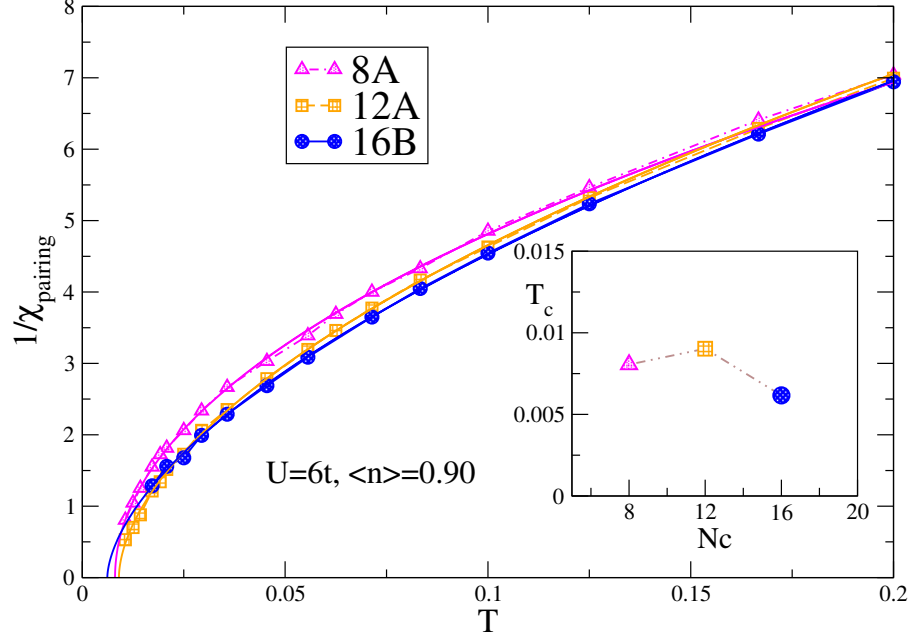
Figure G.2: (color online) Temperature dependence of the inversed d-wave paring susceptibility for different cluster geometries at filling $\langle n \rangle = 0.90$. . The solid line are fitted using the formula $\chi(T) = a_0 * abs(T - a_1)^{a_2}/(T - a_1)$, from which one can extract the transition temperature (results are shown in the inset).

G.2.1 Determination of the Superconducting Phase Transition Line

G.2.2 Determination of the Pseudo-Gap Temperature Line

The pseudo-gap temperature is defined where the pseudo-gap is formed in the density of states. This happens at the same temperature where the bulk spin susceptibility achieves its maximum value [21]. Therefore, by looking into the temperature dependence of the spin susceptibility, one can detect the pseudo-gap temperature.

G.2.3 Determination of the Fermi-liquid Cross-Over Temperature Line

The Fermi-liquid cross-over temperature T_X is determined by fitting the quasi-particle weight to the combined expression of marginal Fermi-liquid and Fermi-liquid behaviors (see ref [20] for more details).

Collecting all the information extracted from the above procedure, we can thus determine the phase diagram for the 2-D Hubbard model. See Fig. G.4 for the resulting phase-diagram.
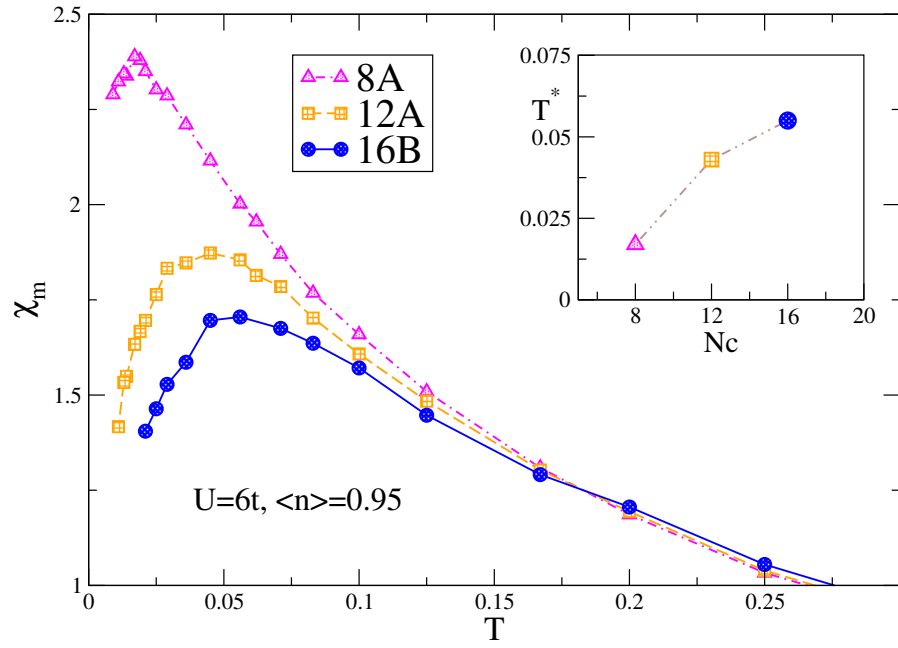
Figure G.3: (color online) Temperature dependence of bulk magnetic susceptibility for different cluster geometries at filling $\langle n \rangle = 0.95$. The temperature where the susceptibility has maximum value is identified as the pseudo-gap temperature T^*. The cluster dependence of T^* are shown in the inset.
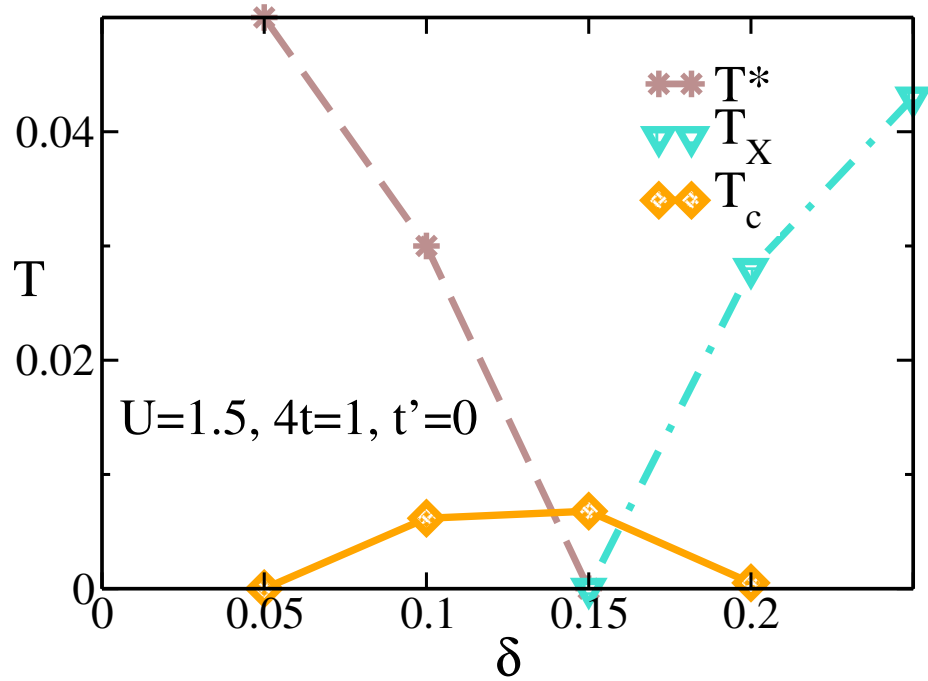
Figure G.4: (color online) Phase diagram for the 2-D Hubbard model. The x-axis is the hole doping. T_c denotes the d-wave superconducting transition temperature, T^* the pseudo-gap temperature, and T_X the Fermi-liquid cross-over temperature.

Appendix H

Vertex Decomposition

With the paring formalism, one can analyze the underlying mechanism driving the phase transition with more detailed. By looking into the behaviors of these two quantities around the transiton temperature, one can tell whether the transiton is driven by the bare susceptibility driven, or by the vertex. And to further analyze what happens for the system around the transition point, we will employ the parquet equations to decomposition the irreducible vertex.

H.1   Vertex Decomposition Scheme

One can further look into the different contributions to the irreducible vertex by using the parquet equation and decompose the irreducible vertex into different components. In this way, one can tell which scattering channel is responsible for the phase transion, and get much information about how the paring is formed.

H.2   Application on the Spin Instability

The 2-D Hubbard model at half-filling has an anti-ferromagnetic ground state. For high temperature, the system is paramagnetic. The paramagnetic to anti-ferromagnetic transition happens at the so-called Neel temperature. People believe that the transition is caused by the Anderson's super-exchange interaction

$$J \sim \frac{4t^2}{U} \tag{H.1}$$

Spin instability is caused by the fully irreducible vertex, in which the bare interaction has the largest contribution.
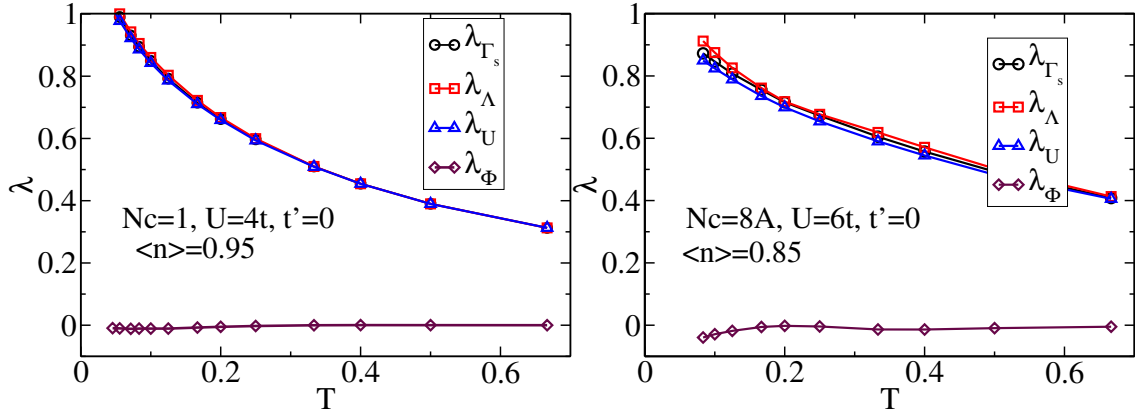
Figure H.1: Spin channel vertex decomposiontion results for the Nc=1 case (left) and Nc=8 case (right). For both cases, the divergence is dominated by the fully irreducible vertex contribution, while the crossed channel contribution is almost zero.. And note that for this two set of parameters, the contributions to the fully irreducible vertex mainly come from the first-order of U.
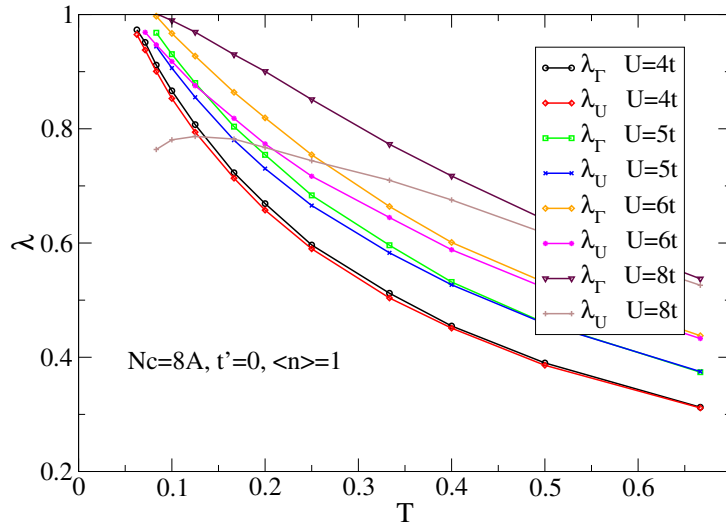

Figure H.2: (color online) Leading eigen-value result for $q = (\pi, \pi)$, $i\nu = 0$ spin channel for different U's. For small U, the divergence comes from the bare interaction contribution. As U increases, high-order contribution become important as well, which explains the increasing difference from λ_Γ and λ_U.

Appendix I

Inability to Extract the Irreducible Vertex Function

In this appendix, we will show that the conventional two-particle formalism breaks down in some parameter regions, due to its inability to extract the irreducible vertex functions. Since the DF approach is parameterized by the reducible cluster vertex, which can always be calculated, while other multiscale approaches are parameterized by the irreducible or fully irreducible vertices[45, 17], this breakdown further justifies the DF based methods.

Conventional two-particle formalisms rely upon either the reducible or the irreducible vertices (F or Γ) [36]. They are related by the well-known Bethe-Salpeter equation:

$$F = \Gamma + \Gamma \chi_0 F. \tag{I.1}$$

Given that the bare susceptibility, χ_0, is known, the knowledge of either one of them is enough to calculate the other. For example, F can be expressed as

$$F(Q)_{P,P'} = \frac{\Gamma(Q)_{P,P'}}{1 - \Gamma(Q)_{P,P'}\chi_0(Q)_{P'}}. \tag{I.2}$$

A divergence in F, and then in χ since $\chi = \chi_0 + \chi_0 * F * \chi_0$, denotes a second-order phase transition, which is used to identify the boundary lines in the phase diagram.

By inverting the above Bethe-Salpeter equation, we can write formally the irreducible vertex in terms of the full vertex and bare susceptibility as

$$\Gamma(Q)_{P,P'} = \frac{F(Q)_{P,P'}}{1 + F(Q)_{P,P'}\chi_0(Q)_{P'}}. \tag{I.3}$$

Note that the above equation involves the inversion of a matrix. We would thus expect to encounter similar situation as in solving the Bethe-Salpeter equation. Namely, Γ could be divergent in some parameter region. And the region of convergence for this equation can be defined by the boundary where the leading eigenvalue (LEV) for $-F(Q)_{P,P'}\chi_0(Q)_{P'}$ becomes equal to one. Fig. I.1 displays the LEV's for different channels. The LEV for the $i\nu = 0$ charge channel, the most singular channel and frequency, approaches one
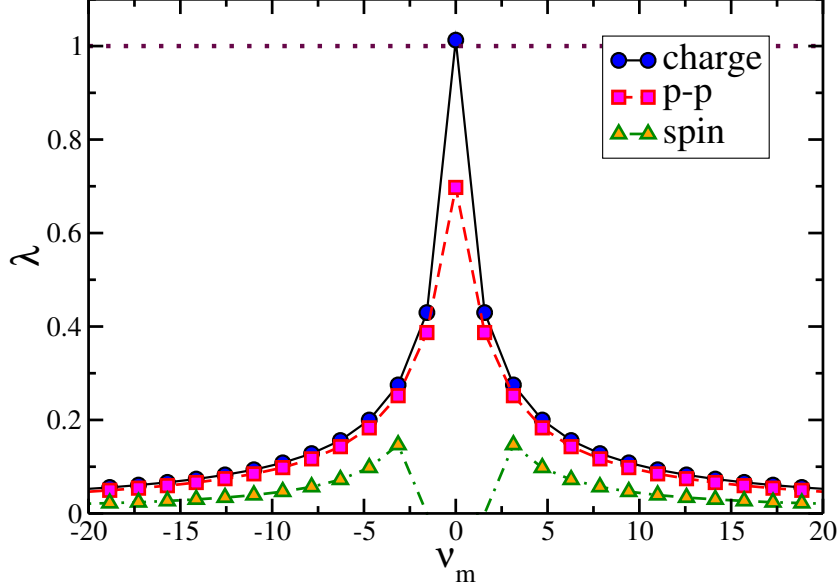
Figure I.1: (color online) The external frequency dependence of the leading eigen-values (LEV's) for different channels. Note that the LEV for $i\nu = 0$ charge channel goes across one. This is the reason for the divergence of the irreducible charge vertex in the low frequency region. The parameters used are: $N_c = 1$, $U = 6t$, $\beta = 4t/T = 4$, $\langle n \rangle = 0.95$.

for the set of parameters we show, for which the irreducible vertex diverges (not shown here). For this set of parameters, LEV's for all the other channel are less than one.

Since this divergence exists already at high temperatures and only for strong enough interaction, it is not likely to be driven by the temperature, but instead by the interaction. For a fixed temperature, as we increase the interaction, we can observe the LEV's increasing nicely (Fig. I.2). It suggests that there is a critical U, above which we cannot invert the Bethe-Salpeter equation. At half-filling, this U_c is about 1.35 for the infinite cluster size limit. Also note that in Fig. I.2, DCA and finite-size simulation (FSS) results converge to the same infinite cluster size limit from different directions. This is consistent with the fact that DCA tends to over-estimate the correlation, while FSS tends to under-estimate the correlation, so that DCA and FSS results converge complementarily.

Note that this breakdown does not invalidate the phase diagrams calculated through the DCA or the DMFA even for large U or near half filling. Here, Γ_c is only implicitly needed, and its calculation can be avoided by using another form of the Bethe-Salpeter equation to obtain the lattice reducible vertex

$$F_{lattice} = \frac{F_c}{1 - F_c(\bar{\chi}_0 - \chi_{0,c})} \tag{I.4}$$

instead of the conventional one [42, 67]

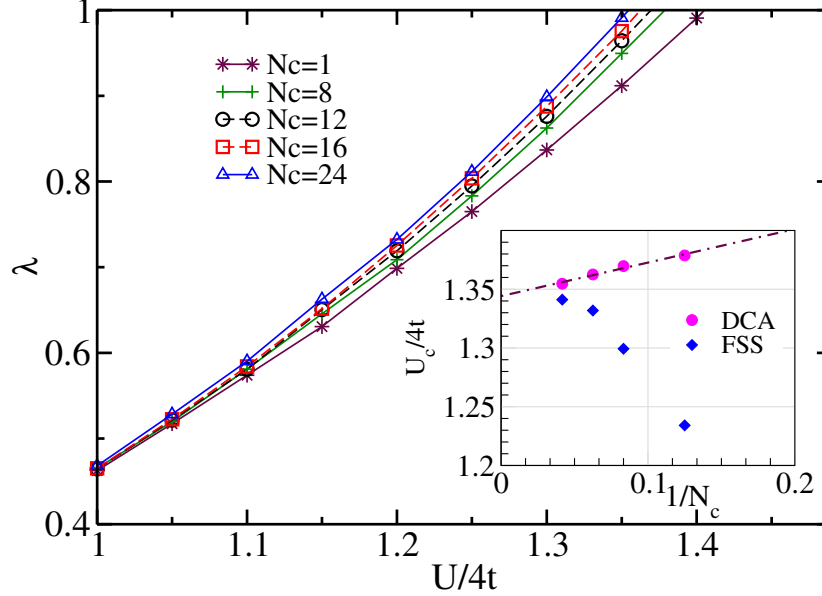$$F_{lattice} = \frac{\Gamma_c}{1 - \Gamma_c \bar{\chi}_0}. \tag{I.5}$$

Figure I.2: (color online) The U-dependence of the leading eigen-values for different DCA cluster sizes. The inset shows the DCA cluster size dependence of the critical U determined from the leading eigen-value crossing one. Finite-size simulation (FSS) data is also displayed. The parameters used are: $\beta = 4t/T = 4$, $\langle n \rangle = 1$.

One can also thus construct the pairing matrix as $M = F_c(\bar{\chi}_0 - \chi_{0,c})$, which exactly corresponds to the DFDCA calculation when corrections from the dual fermion lattice calculation are turned off.

So far, we are not able to discern a physical explanation for the existence of U_c. Nevertheless, this inability to extract the irreducible vertex renders two-particle approaches based on the irreducible or even fully irreducible vertex questionable, and partially explains the difficulty associated with the parquet approximation calculation [36]. However, the DFDCA scheme is parameterized by the reducible cluster vertex, so we do not need to invert the Bethe-Salpeter equation and thus do not have this problem.

Appendix J

Perturbation Theory for the Dual Fermion Lattice Calculation

J.1 Some Conventions

In the dual fermion calculation, we use K to label the DCA cluster momentum, $\tilde{k}$ for the momentum inside the DCA coarse-graining cell, and k for the lattice momentum. And they are related by $k = K + \tilde{k}$ (see Fig. J.1).
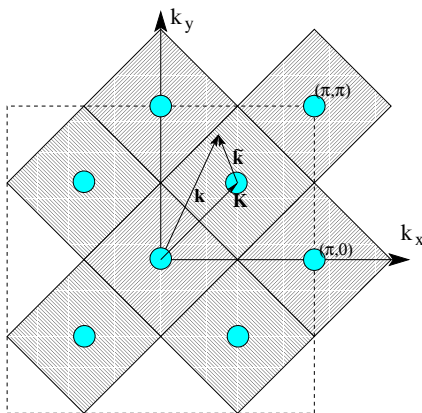

Figure J.1: Momentum index convention for the dual fermion lattice calculation. Shown is for Nc=8 DCA cluster. The DCA momentum is denoted by the captical letter K, the dual lattice momentum by small letter k, and the momentum inside the DCA coarse-graining cell by $\tilde{k}$, so that $k = K + \tilde{k}$.

It is convenient to use the combined index for the frequency and momentum $p = (i\omega_n, k)$ for the lattice, and $P = (i\omega_n, K)$ for the DCA cluster. So assuming the DCA cluster is of size Nc_1 and latticle of size Nc_2, and nf number of Matsubara frequencies is used, we have the system size nt_1 for the DCA cluster system and nt_2 for the lattice system.

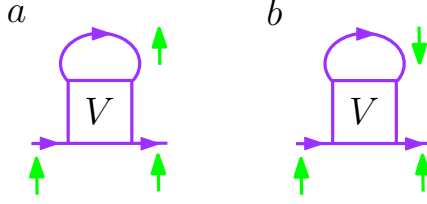## J.2 Hartree-Fock Contributions

Figure J.2: Hartree-Fock contributions to the dual fermion self-energy from the particle-hole (p-h) channel.

As the lowest-order correction to the dual fermion self-energy, the Hartree-Fock contributions can be easily calculated according to (see Fig. J.2 for the Feynman diagrams)

$$\Sigma^{(1)}(p) = -\sum_q (\frac{1}{2}V_d(q)_{p,p}G(p+q) + \frac{3}{2}V_m(q)_{p,p}G(p+q)) \tag{J.1}$$

from the p-h channel. Since we are using the DCA cluster reducible vertex to approximate the bare vertex for the dual lattice system

$$V_d(q)_{p,p'} = V_d(Q)_{P,P'} = F(Q)_{P,P'}, \tag{J.2}$$

thus we have

$$\Sigma^{(1)}(p) = -\sum_q (\frac{1}{2}V_d(Q)_{P,P}G(p+q) + \frac{3}{2}V_m(q)_{p,p}G(p+q)) \tag{J.3}$$

Or equivalently, we might calculate it from the p-p channel

$$\Sigma^{(1)}(p) = \sum_q (V^p(Q)_{-P,-P}G(p+q) + V_t(Q)_{-P,-P}G(p+q)) \tag{J.4}$$

$$= \sum_q (2V^p(Q)_{-P,-P}G(p+q) - V^{p'}(Q)_{-P,-P}G(p+q)) \tag{J.5}$$

where we have used

$$X^p(q)_{p,p'} \equiv X^p_{\uparrow\downarrow;\uparrow\downarrow}(q)_{p,p'} \tag{J.6}$$

and

$$X_t(q)_{p,p'} = X^p_{\uparrow\downarrow;\uparrow\downarrow}(q)_{p,p'} + X^p_{\uparrow\downarrow;\downarrow\uparrow}(q)_{p,p'} \tag{J.7}$$

$$= X^p_{\uparrow\downarrow;\uparrow\downarrow}(q)_{p,p'} - X^p_{\uparrow\downarrow;\uparrow\downarrow}(q)_{p,-p'-q} \tag{J.8}$$

$$= X^p(q)_{p,p'} - X^p(q)_{p,-p'-q} \tag{J.9}$$

$$\equiv X^p(q)_{p,p'} - X^{p'}(q)_{p,p'} \tag{J.10}$$

The computational complexity for the calculation of the self-energy can be easily identified as $\mathcal{O}(nt_2^2)$.

J.3   Second-Order Contributions

Similarly we can also calculate the second-order contributions to the dual fermion self-energy. The Feynman diagrams for contributions from the p-h channel are shown in Fig. J.3.
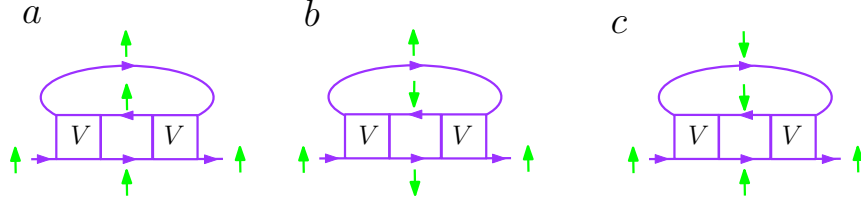

Figure J.3: Second-order contributions to the dual fermion self-energy from the particle-hole (p-h) channel.

The first and second contributions (a and b in Fig. J.3) are from the longitudinal spin-charge channel (ring-type diagrams), and can be written down as (in a matrix form)

$$-\frac{1}{2}(V_d\chi_0^{ph}V_d + V_m\chi_0^{ph}V_m)G \tag{J.11}$$

where

$$\chi_0^{ph}(q)_p \equiv G(p+q)G(p) \tag{J.12}$$

while the third contribution (c in Fig. J.3) from the transverse spin channel (ladder-type diagrams)

$$-V_m\chi_0^{ph}V_mG \tag{J.13}$$

Note that for the second-order contributions, it turns out contribution c is topologically the same as contribution b. So the second-order contribution is

$$\Sigma^{(2)} = -(\frac{1}{2}V_d\chi_0^{ph}V_d + \frac{1}{2}V_m\chi_0^{ph}V_m)G \tag{J.14}$$

This expression can be simplified by introducing the vertex ladder (see Fig. J.4)

$$\Phi_{d/m}(q)_{p,p'} \equiv \sum_{p''} F_{d/m}(q)_{p,p''}\chi_0^{ph}(q)_{p''}V_{d/m}(q)_{p'',p'} \tag{J.15}$$

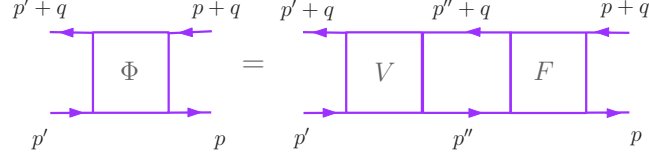For the second-order contribution, $F \approx V$, therefore

Figure J.4: Definition of the vertex ladder.

$$\Phi_{d/m}^{(2)}(q)_{p,p'} = \Phi_{d/m}^{(2)}(q)_{P,P'} \equiv \sum_{p''} V_{d/m}(Q)_{P,P''} \chi_0^{ph}(q)_{p''} V_{d/m}(Q)_{P'',P'} \qquad (\text{J.16})$$

$$= \sum_{P''} V_{d/m}(Q)_{P,P''} \bar{\chi}_0^{ph}(q)_{P''} V_{d/m}(Q)_{P'',P'} \qquad (\text{J.17})$$

where we have introduced the coarse-grained bare susceptibility

$$\bar{\chi}_0^{ph}(q)_P \equiv \frac{Nc_1}{Nc_2} \sum_{\tilde{k}} \chi_0^{ph}(q)_p. \qquad (\text{J.18})$$

Thus

$$\Sigma^{(2)}(p) = -\sum_q (\frac{1}{2} \Phi_d^{(2)}(q)_{P,P} G(p+q) + \frac{1}{2} \Phi_m^{(2)}(q)_{P,P} G(p+q)) \qquad (\text{J.19})$$

The computational complexity for forming the vertex ladder scales as $\mathcal{O}(nt_1^2 * nt_2)$ (we only need the diagonal elements), and for the calculation of self-energy and the coarsed-grained bare susceptibility, it scales as $\mathcal{O}(nt_2^2)$.
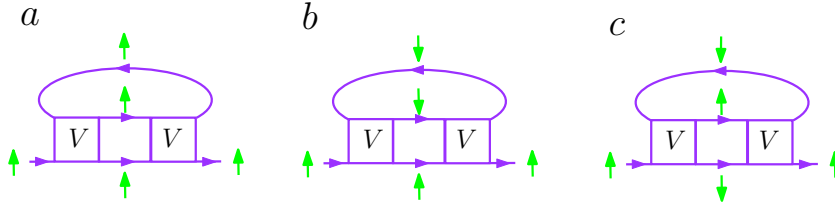

Figure J.5: Second-order contributions to the dual fermion self-energy from the particle-particle (p-p) channel.

The second-order contribution can also be written down in the p-p channel as (see Fig. J.5)

$$\Sigma^{(2)} = (V^p \chi_0^{pp} V^p + V_t \chi_0^{pp} V_t)G \qquad (\text{J.20})$$

where

$$\chi_0^{pp}(q)_p \equiv -G(p+q)G(-p) \qquad (\text{J.21})$$
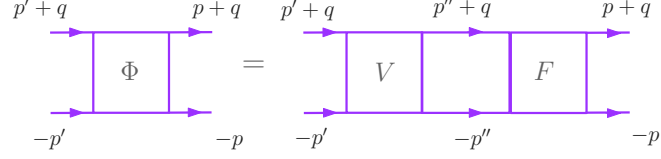
110

Figure J.6: Definition of the vertex ladder for the p-p channel.

Similar to the p-h channel, we define the vertex ladder as

$$\Phi(q)_{p,p'} \equiv \sum_{p''} F(q)_{p,p''} \chi_0^{pp}(q)_{p''} V(q)_{p'',p'} \tag{J.22}$$

and

$$\Phi^{(2)}(q)_{p,p'} = \Phi^{(2)}(q)_{P,P'} \equiv \sum_{p''} V(Q)_{P,P''} \chi_0^{pp}(q)_{p''} V(Q)_{P'',P'} \tag{J.23}$$

$$= \sum_{P''} V(Q)_{P,P''} \bar{\chi}_0^{pp}(q)_{P''} V(Q)_{P'',P'} \tag{J.24}$$

where

$$\bar{\chi}_0^{pp}(q)_P \equiv \frac{Nc_1}{Nc_2} \sum_{\tilde{k}} \chi_0^{pp}(q)_p. \tag{J.25}$$

Thus

$$\Sigma^{(2)}(p) = \sum_q (\Phi^{p(2)}(q)_{-P,-P} G(p+q) + \Phi_t^{(2)}(q)_{-P,-P} G(p+q)) \tag{J.26}$$

$$= \sum_q (2\Phi^{p(2)}(q)_{-P,-P} G(p+q) - \Phi^{p'(2)}(q)_{-P,-P} G(p+q)) \tag{J.27}$$
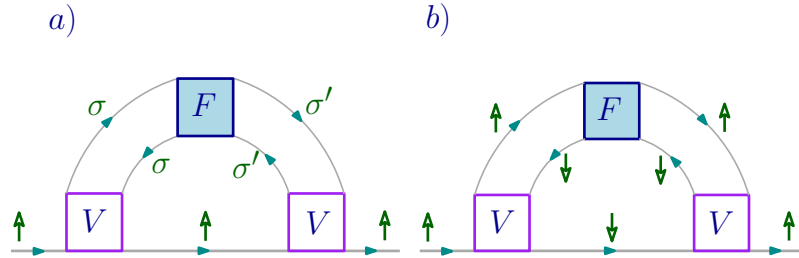
J.4 FLEX Contributions

Figure J.7: FLEX contributions to the dual fermion self-energy from the p-h channel. a), longitudinal spin-charge channel, and b), transverse spin channel.

Similar to second-order contributions, for the FLEX, some contributions to the self-energy are from p-h longitudinal spin-charge and transverse channels (see Fig. J.7). They are (second-order excluded to avoid the double counting)

$$\Sigma^{ph}(p) = -\sum_q [\frac{1}{2}(\Phi_d - \Phi_d^{(2)})(q)_{P,P}G(p+q) + \frac{3}{2}(\Phi_m - \Phi_m^{(2)})(q)_{P,P}G(p+q)] \quad \text{(J.28)}$$

And for the contributions from the p-p channel, they are (see Fig. J.8)

$$\Sigma^{pp}(p) = \sum_q [2(\Phi^p - \Phi^{p(2)})(q)_{-P,-P}G(p+q) - (\Phi^{p'} - \Phi^{p'(2)})(q)_{-P,-P}G(p+q)] \quad \text{(J.29)}$$
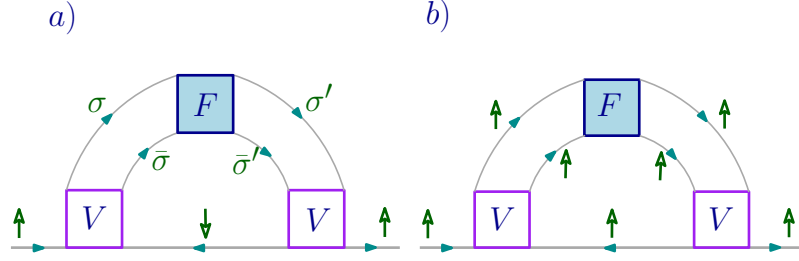

Figure J.8: FLEX contributions to the dual fermion self-energy from the p-p channel. Note that the two different spin arrangements for the internal two Green function lines in a) are actually corresponding to the same self-energy contribution due to the crossing symmetry of the vertex functions.

Note that they are topologically different contributions.
Therefore, we have

$$\Sigma_{FLEX}(p) = \Sigma^{(1)}(p) + \Sigma^{(2)}(p) + \Sigma^{ph}(p) + \Sigma^{pp}(p) \quad \text{(J.30)}$$

The vertex ladder $\Phi(q)_{P,P'}$ can be easily calculated by using the Bethe-Salperter equation

$$F(q)_{P,P'} = V(Q)_{P,P'} + \sum_{P''} V(Q)_{P,P''}\bar{\chi}_0(q)_{P''}F(q)_{P'',P'} \quad \text{(J.31)}$$

$$= V(Q)_{P,P'} + \Phi(q)_{P,P'} \quad \text{(J.32)}$$

where we have made the FLEX approximation $\Gamma(Q)_{P,P'} \approx V(Q)_{P,P'}$. Thus

$$\Phi(q)_{P,P'} = F(q)_{P,P'} - V(Q)_{P,P'} \quad \text{(J.33)}$$

and

$$F(q)_{P,P'} = [\frac{V(Q)}{1 - V(Q)\bar{\chi}_0(q)}]_{P,P'} \quad \text{(J.34)}$$

It scales as $\mathcal{O}(nt_1^3 * nt_2)$ and is thus the computational bottle-neck of the dual fermion lattice calculation.

Appendix K

Author Publication List

1. *Parquet approximation for the 4x4 Hubbard cluster*, S. X. Yang, H. Fotso, J. Liu, T. A. Maier, K. Tomko, E. F. D'Azevedo, R. T. Scalettar, T. Pruschke, M. Jarrell, Phys. Rev. E **80**, 046706 (2009), arXiv:0906.4736

2. *Comment on "Exact bosonization for an interacting Fermi gas in arbitrary dimensions"*, Dimitrios Galanakis, Shuxiang Yang, Fakher Assaad, Mark Jarrell, Philip Werner, Matthias Troyer, Phys. Rev. Lett. **105**, 159701 (2010), arXiv:0911.5155

3. *Proximity of the Superconducting Dome and the Quantum Critical Point in the Two-Dimensional Hubbard Model*, S.-X. Yang, H. Fotso, S.-Q. Su, D. Galanakis, E. Khatami, J.-H. She, J. Moreno, J. Zaanen, and M. Jarrell, Phys. Rev. Lett. **106**, 047004 (2011), arXiv:1101.6050

4. *The response to dynamical modulation of the optical lattice for fermions in the Hubbard model*, Zhaoxin Xu, Simone Chiesa, Shuxiang Yang, Shi-Quan Su, Daniel E. Sheehy, Juana Moreno, Richard T. Scalettar, Mark Jarrell, Phys. Rev. A **84**, 021607(R) (2011), arXiv:1104.1739

5. *Dual Fermion Dynamical Cluster Approach for Strongly Correlated Systems*, S.-X. Yang, H. Fotso, H. Hafermann, K.-M. Tam, J. Moreno, T. Pruschke, M. Jarrell, Phys. Rev. B **84**, 155106 (2011), arXiv:1104.3854

6. *Role of the van Hove Singularity in the Quantum Criticality of the Hubbard Model*, K.-S. Chen, S. Pathak, S.-X. Yang, S.-Q. Su, D. Galanakis, K. Mikelsons, M. Jarrell, J. Moreno, arXiv:1104.3261

7. *Solving the Parquet Equations for the Hubbard Model beyond Weak Coupling*, Ka-Ming Tam, H. Fotso, S.-X. Yang, Tae-Woo Lee, J. Moreno, J. Ramanujam, M. Jarrell, arXiv:1108.4926

Vita

Shuxiang Yang was born in December 1979, in Liancheng, China. He finished his under-graduate study in 2004 and his master degree in physics in 2006 at Zhengjiang University. He then went to University of Cincinnati in September 2006 to pursue the PhD training in physics. In Juanary 2009 he moved to Louisiana State University to continue his PhD training. He is currently a candidate for the degree of Doctor of Philosophy in physics, which will be awarded in Fall semester of 2011.